CHARACTERIZATION OF GALLIUM ANTIMONIDE CRYSTALS
GROWN UNDER MICROGRAVITY CONDITIONS BY THE
LIQUID ENCAPSULATED MELT ZONE (LEMZ) TECHNIQUE

By

JEFFREY ROBERT MILEHAM

A DISSERTATION PRESENTED TO THE GRADUATE SCHOOL
OF THE UNIVERSITY OF FLORIDA IN PARTIAL FULFILLMENT
OF THE REQUIREMENTS FOR THE DEGREE OF
DOCTOR OF PHILOSOPHY

UNIVERSITY OF FLORIDA

1999

To my wife, Beatriz

ACKNOWLEDGMENTS

CHARACTERIZATION OF GALLIUM ANTIMONIDE CRYSTALS
GROWN UNDER MICROGRAVITY CONDITIONS BY THE
LIQUID ENCAPSULATED MELT ZONE (LEMZ) TECHNIQUE

By

Jeffrey Robert Mileham

August 1999

Chairperson: Dr. Stephen Pearton
Cochairperson: Dr. Reza Abbaschian
Major Department: Materials Science and Engineering

A Liquid Encapsulated Melt Zone (LEMZ) technique was used to grow [100] GaSb

single crystals under microgravity conditions aboard the STS-77 Shuttle Endeavor mission.

One tellurium-doped and two undoped single crystals, encapsulated in a eutectic mixture of

sodium-chloride and potassium-chloride, were regrown from 16 mm diameter single crystal

rods. The quality of the crystals was compared to those grown on ground using the same

technique. It was found that the microgravity-grown crystals, particularly the Te-doped

crystal, exhibited lower dislocation densities than those grown on ground. The dislocation

density was also found to depend on the solid/liquid interface shape with a planar interface

resulting in a lower density. Reduction of rotational and nonrotational striations was obtained

with the encapsulation technique in all crystals. Moreover, the use of the encapsulant allowed for longer and more stable melt zones for those samples processed on ground.

Macrosegregation of the tellurium dopant revealed that convective-controlled growth occurred in both microgravity and terrestrial environments. The use of an encapsulant helped control but did not eliminate Marangoni convection and/or convection caused by variations in the gravity level. Irregular radial dopant distribution in the microgravity sample was attributed to localized convective flows at the growth interface caused by uneven heating when the sample was pushed off its growth axis by an argon bubble in the ampoule.

Hall and photoluminescence measurements confirmed the high quality of the crystals, but revealed that growth under different gravity environments did not influence their electrical or optical properties. However, several results from this study were highly useful in helping to understand the lesser studied gallium antimonide material system itself. Variable temperature Hall and photoluminescence measurements in the undoped crystals found two dominant acceptors at 12.5 and 33 meV below the bandgap edge. The temperature variation of the latter peak compared to the bandgap edge was explained by either a true decrease in the ionization energy of this level or by a variation in the photoabsorption capture cross section which is different than most other semiconductors. In the n-type samples, Hall measurements were used to calculate the energy level of the subsidiary conduction band and its temperature variation.

INTRODUCTION

Research Motivation

Semiconductor single crystals are key component materials in a large variety of technical products. Unfortunately, all currently available growth methods suffer from inherent limitations and, as a result, the crystals contain growth-related defects and undesirable imperfections. Presently, established growth procedures are not able to adequately meet of the degree of chemical and crystalline perfection required for advanced applications, especially in compound semiconductors. Complicating this problem, compound semiconductor growth is hindered in both the research and industrial environment by poor reproducibility under similar growth conditions, sometimes even using the same equipment.

As outlined by Müller [95MÜL], a major reason for these problems is the industrial development of growth processes based on experimentation and scientific intuition rather than fundamental understanding of growth-related phenomenon. Even today, the primary aim of industrial research, achievement of competitive yields, usually takes precedence over the development of new growth techniques or the advancement of knowledge in current methods of crystal growth. Fundamental research on crystal growth from the melt has been very limited and has not been carried out at a scale proportional to the importance of semiconductor single crystals to commercial applications.

Since established growth procedures for one material system based upon empirical knowledge are not fully transferable to other material systems, property requirements for many advanced applications cannot be adequately met by current growth methods. Modifications of growth procedures has to be determined by time consuming and expensive trial-and-error experimentation. Complicating matters further, the development of the current techniques has advanced so far that is becoming more difficult to optimize one growth parameter without adversely affecting other parameters. To step from empiricism to science in crystal growth requires that we obtain the knowledge to describe the correlation between properties of crystals and the parameters by which they were grown.

To this means, the following will describe the effects of gravity as a variable in crystal growth. Traditionally, growth processes rarely considered gravity as a component in crystal growth that could be altered. On one extreme, surprisingly little research has been done with enhanced gravity (for a review of this, see another publication by Müller in [90MÜL]). With the relatively recent emergence of space flight, the other extreme of microgravity (μg) can be reached. A discussion of the effect of gravity and other parameters upon traditional and state-of-the-art crystal growth processes such as that used in this study will be detailed in the literature review.

The Commercial Float Zone Furnace and the Floating Zone Technique

The experiments for this work were processed in the Commercial Float Zone Furnace (CFZF) payload which was launched on May 19, 1996, in the SPACEHAB-04 Module, aboard the Shuttle Endeavor, as part of the STS-77 mission operations. The objective for this

payload, managed by the Canadian Space Agency (CSA), was to grow single crystals of technologically important semiconductor materials in a microgravity environment by means of the floating-zone (FZ) technique. Four institutions comprised the scientific teams, each one processing different materials. The University of Florida, funded by the Marshall Space Flight Center (MSFC), used the Liquid Encapsulated Melt Zone (LEMZ) technique to process undoped and Tellurium-doped Gallium Antimonide (GaSb), encapsulated in an eutectic mixture of NaCl and KCl. The University of Freiburg, sponsored by the Deutsche Agentur fur Raumfahrtangelegenheiten GmbH (DARA), processed unencapsulated undoped Gallium Antimonide (GaSb). The University of Dalhousie, funded by CSA, experimented with encapsulated Cadmium Germanium Arsenide (CdGeAs2). The Canadian Center for Mineral and Energy Technology (CANMET), also funded by CSA, processed samples of Bismuth Germanium Oxide (BGO).

The floating-zone technique, which was utilized by all four groups to grow the crystals, makes use of the physical property known as surface tension to maintain a column of molten material attached to sections of unmolten material above and below it. The molten section, known as the float zone, is translated along the axis of the crystal to effect the crystal growth and thus convert the feedstock into a newly grown material. The furnace established this float zone by means of a Paraboloid-Ellipsoid Mirror Furnace (ELLI-FM) manufactured and operated by the Dornier Deutsche Aerospace Company, Friedrichshafen, Germany. The furnace focuses radiation, emitted by a halogen lamp, onto a narrow band of sample material to melt this and thus establish a float zone. The sample, enclosed in hermetically sealed quartz ampoules, then translated along its axis to effect the desired crystal growth. The

ELLI-EM furnace, a ground-dedicated copy of the flight furnace, was used at the University of Florida to process samples on ground and conduct three astronaut training activities with the objective of familiarizing Astronauts Marc Garneau and Andy Thomas with the crystal growth technique and the operation of the furnace.

Liquid Encapsulated Melt Zone Technique on GaSb

The LEMZ technique, utilized by the University of Florida, is a version of the FZ technique in which an encapsulant is introduced to completely surround the floating zone and growing crystal from the rest of the growth system. The advantages of this technique over the classical floating zone systems include [94JEN]

1. Improved stoichiometry control

2. Reduction of thermal gradients

3. Enhanced molten zone stability

4. Suppression of thermocapillary flows

Details of this technique will be given further in the Literature Review and Experimental sections as appropriate. Three single-crystal rods of the technologically important gallium antimonide semiconductor crystal were regrown in a microgravity environment using the Liquid Encapsulated Melt Zone (LEMZ) technique. In addition, ground processing was also conducted in a similar fashion. It is the goal of this research to study the material properties of the regrown crystals, compare the results with those of crystals grown under similar conditions on earth, and relate both sets of data to processing conditions according to crystal growth theory. The knowledge gained is hoped to stimulate new ideas on the processing of

gallium antimonide crystals as well as other III-V semiconductor crystals. To characterize the quality of the crystals, photoluminescence and Hall measurements examined the optical and electrical properties of the regrown material. In addition, SIMS measurements characterized the macro- and microsegregation in the samples and selective etching investigated the striations and dislocations in the crystal. Moreover, since relatively little is known about GaSb compared to other semiconductor materials, these tests also added to the database of knowledge on this material system.

LITERATURE REVIEW

<u>GaSb Material System</u>

Gallium antimonide is a lesser studied and utilized semiconductor compared to the well known silicon and GaAs material systems. GaSb is a direct bandgap semiconductor capable of either p or n type conductivity with high electron mobilities. Table 1 shows selected electronic properties for the GaSb compound compared to those of Si and GaAs. Recent advances in nonsilica fiber technology have prompted the advancement in materials for devices operating beyond 1.55 μm [97DUT]. Gallium antimonide is a very suitable substrate for epitaxial growth of a number of ternary and quaternary semiconductors since it can be closely lattice matched to InGaAsSb, AlGaAsSb and many other epilayer alloys suitable for semiconductor devices. GaSb-based devices are reviewed in papers by Milnes [93MIL] and Dutta [97DUT]. Antimonide-based ternary and quaternary compounds have been investigated for use in fiber-optic communications over a spectral range from 1.24 (AlGaAsSb) [80SAS] to 4.3 μm (InGaAsSb) [80CHI, 86CHE, 94LE]. In the shorter wavelength range (1.24 to 1.72 μm), the AlGaAsSb/GaSb material system is an alternative to InGaAsP/InP which covers the low-loss and low-dispersion region in silica fibers used in optical fiber communication [81LAW]. On the other end of the spectrum, the $In_xGa_{1-x}As_ySb_{1-y}$ alloys matched to GaSb (y/x ~ 0.9) can offer the possibility of achieving

minimum losses in heavy-metal fluoride fibers between 2 and 4 μm. At these wavelengths, losses due to Rayleigh scattering are significantly reduced up to two orders of magnitude than those currently obtained with silica fibers [84LIN].

Table 1 - Comparison of selected materials properties in GaSb, GaAs and Si (compiled from [88NGA and 91SWA]).

Material	Electron mobility $(cm^{-2} \cdot V^{-1} s^{-1})$	Hole mobility $(cm^{-2} \cdot V^{-1} s^{-1})$	Range of lattice-matched transitions (eV)	Melting Point ($^\circ K$)
GaSb	5000	1400	0.3-1.58	985
GaAs	9000	500	1.42-1.91	1511
Si	1900	500	N/A	1683

Moreover, GaSb-based devices have turned out to be a promising candidate for high speed electronic and long wavelength photoelectronic devices. AlGaSb is an advancing material for avalanche photodiodes (APDs) owing to its high hole-to electron ionization rate (β/α) which can lead to low avalanche noise at high gains and high sensitivity at high bit rates [81LAW, 81HIL, 85AND]. Also, antimony-based semiconductors can be used as infrared detectors in the 5-15 μm wavelength range [92BRO].

Table 2 gives the materials properties of GaSb that are relevant to this study. Note that this table is presented here as a reference for the rest of the investigation.

Table 2 - Materials properties of GaSb [97DUT].

Lattice Constant (Å)	6.0959
Density (g·cm^{-3})	5.6137
Melting point (°C)	712
Coefficient of thermal expansion (10^{-6} °C^{-1} at 300°K)	7.75

Direct energy gap (eV)
    at 0°K
    at 300°K)
	0.812
	0.725

Temperature dependence of minimum energy gap, ($\times 10^{-4}$ eV·K^{-1})
    α
    β
	4.2
	140

Effective mass of electrons (in units of m_o)
    Γ band, $m_e(\Gamma)$
    L band, $m_e(L)_\perp$
                  $m_e(L)_\parallel$
                  $m_{de}(L)$(density of state)
	0.0412
	0.11
	0.95
	0.226

Effective mass of holes (in units of m_o)
    heavy
    light
    density of state
	0.28
	0.05
	0.82

Wave number of TO phonons (cm^{-1})	224.0
Wave number of LO phonons (cm^{-1})	233.0

Bulk Growth of GaSb Crystals

Typically, growth of bulk crystals is performed by the Czochralski technique (CZ). There is also a limited study of crystal growth by the Bridgman (BG) technique, traveling heater method (THM), and vertical gradient freeze (VGF) technique. Each method has its own advantages and disadvantages. However, no matter which method is used substrate crystals

grown on earth commonly exhibit compositional and structural defects which limit the exploitation of their full potential in solid state electronics [82GAT]. The principle problems related to crystal growth on ground are summarized as follows [82GAT]

- Compositional inhomogeneities - a continuous change in solute concentration along the length of the grown crystal (macrosegregation) and/or local variations of the dopant material (microsegregation).

- Structural inhomogeneities - line defects and microdefects such as dislocation loops.

- Contamination from the container - chemical interactions of melts with the container are enhanced by the convective flow.

- Stoichiometric variations - variations of volatile constituents.

The details of some of these problems and their effects upon crystal and device quality will be reviewed in subsequent sections; for now it is enough to recognize that they are undesireable. First a review of traditional and state-of-the-art crystal growth processes will follow. Crystal growth systems are classified into two major categories depending on whether the surrounding ampoule or the melt meniscus near the solidification interface controls the shape of the growing crystal. The former is identified as a confined growth system while the latter is identified as a meniscus-defined system.

On of the most common meniscus-defined techniques to grow crystals is the classical Czochralski process. Here a seeded single crystal is withdrawn for the melt and is rotated to maintain thermal and cylindrical geometry. For small crystal diameters, thermal stresses are low and dislocation free crystals can be grown; however, in larger diameter crystals (>20mm), dislocation generation is primarily caused by thermal stresses because of large

radial and axial temperature gradients [91SWA]. Moreover, dislocation distribution across the crystal diameter is not homogeneous according to the thermal stresses model [83JOR]. In this model, the dislocation density is proportional to the total resolved shear stresses minus the critical resolved shear stress for the onset of plastic deformation. Higher dislocation densities are found near the edge and center of the crystal and in the <100> direction in {100} wafers. GaSb crystals grown by the CZ technique show microfacets, twins, and impurity striations [77KUM, 78KUM]. Recently, Firebird Semiconductors Ltd., Canada have grown 85 mm diameter GaSb single crystals by the CZ technique [97DUT].

The most common confined growth system is the Bridgman technique where crystals are grown in a boat. A furnace with a constant temperature gradient is translated over the melt allowing the solid-liquid interface to move. Bridgman techniques allows lower thermal gradients. High quality crystals with dislocation densities <50 cm^{-2} have been achieved with GaSb grown by this technique [94DUTa, 94DUTb]. Also, reduced thermal gradients means that convection and the associated impurity striations are also decreased [97DUT]. However, contact between the growing crystal and the wall can initiate the nucleation of grain boundaries at the periphery of the crystal and cause impurities pickup. Also, stresses due to differential contraction between the crucible and the crystal during cooling generate stresses which can lead to dislocations [91WIL].

The traveling heater method utilizes a solvent placed between the solid seed and the feed material. Crystallization takes place at the seed/solvent interface and dissolution of the feed material at the solvent/feed boundary. The main advantage of this technique is low growth temperatures which reduces stoichiometric variations caused by volatilization of high vapor

pressure constituents and stoichiometric native defect concentrations (discussed later). There are only a few reports of crystal growth by this method [79BEN, 83MÜL]. The main disadvantage of this technique is its low growth rate of around 1-5 mm/day.

Floating-zone (FZ) is another growth technique in which a molten pool, known as the float zone, is held between the grown material and the feedstock by surface tension forces. It is another example of a meniscus defined growth system. The main advantage of using this method is that the growing crystal and the melt do not come in contact with the container, thus eliminating impurities pickup and/or stress induced defects caused by the container which is common in other growth techniques such as those described above. Also, similar to the Bridgman technique, the thermal gradients are in general lower than in the CZ technique [91WIL]. This is a common technique for production of defect-free silicon crystals as reviewed by Kramer [83KRA].

Although the FZ technique seems to be superior to other growth techniques, it is only utilized in a small percentage of commercially produced GaSb crystals due to the limitations imposed in this material by hydrostatic forces on the diameter of the crystals and due to vaporization loss at the free surface. The loss of wetting at the solid/liquid interface has been the subject of extensive theoretical investigations which suggest that the maximum allowable zone length is proportional to $(\sigma/\rho g)^{1/2}$, where σ is the surface tension of the melt, ρ is the density of the melt and g is the gravitational acceleration. For example, Heywang [56HEY] carried out a detailed analysis of the stability of vertical float zones of a cylindrical geometry. For the case of equal rod diameters, the maximum stable length of the floating zone increases linearly for small rod diameters, but tends to a limiting value for large diameters given by

$$l_{max} = 2.84 \left(\frac{\sigma}{\rho g} \right)^{1/2}. \tag{1}$$

The proportionality constant has also been calculated to be up to 3.6 [77COR].

Attempts have been made to improve the zone stability in other materials under gravity. Inductions coils have been used to levitate silicon zones [81KEL, 92LAN]. Large diameters are easily obtainable in this system compared to other semiconductors due to its high $\sigma/\rho g$ ratio. Also, electron-beam heating has been used to produce short and hence stable zones [57CAL]. A technique called the immersed heater process utilizes a sheet resistance heater immersed horizontally in the molten zone to stabilize it and obtain a flat solid/liquid interface (which as will be seen later is a desired parameter) [65GAS]. However, these techniques are either not possible or have not been tried with GaSb and will not be discussed further.

Microgravity processing by the FZ technique offers the potential of growing larger crystals than possible under terrestrial conditions by overcoming the stability problems imposed by the hydrostatic forces. Rayleigh [1892RAY] calculated the maximum stable zone length for the case of zero gravity to be

$$l_{max} = \pi d \tag{2}$$

where d is the diameter of the zone. This is called the Rayleigh limit. Furthermore, as discussed in the next section, microgravity crystal growth potentially offers a high degree of compositional and structural perfection, as a result of the minimization of buoyancy-driven convective flows [88BRO] (see next section for more details). As an added benefit, this

growth method requires less power than other growth techniques such as CZ and Bridgman since the molten volume is small. This is very beneficial in space where power is a premium commodity. However, as will be discussed in more detail in the next section, the large free surface inherent in the floating zone technique allows for surface-tension driven Marangoni convection, even in space [91WIL]. Additionally, selective volatilization of the higher vapor pressure group V elements in compound semiconductors are still sources of potential problems that must be taken into account with FZ crystal growth in space [82GAT].

The Liquid Encapsulated Melt Zone (LEMZ) technique (used for all samples in this experiment) is shown schematically in Figure 1. This is a variation of the FZ technique that offers the possibility of overcoming the problems of Marangoni convection (and buoyancy convection in earth grown samples) and volitilization. The growth takes place within a molten encapsulant that completely surrounds the growing material and isolates it from the gaseous surrounding.

On earth, liquid suspension of floating zones has been shown to be stable out to the Rayleigh limit if the liquid encapsulant and liquid zone densities are a perfect match [94LOW]. When the fluid densities are not matched, the zone becomes unstable at lengths shorter than the Rayleigh limit (i.e. gravity is destabilizing) [72CAR]. To the authors knowledge, no study has ever been performed using the LEMZ technique upon GaSb. A hybrid technique was used to grow GaSb in which the crucible containing the seed, solid, and liquid GaSb was placed in a second container of liquid salt (eutectic LiCl and KCl) [89GAR]. Both containers were placed in a gradient furnace and the sample was allowed to grow with a low thermal gradient (7 K·cm^{-1}) It was found that the liquid encapsulated the

growing crystal during solidification (i.e. wetting of the crucible by the GaSb was prevented). Dislocation densities below 100 cm^{-2} were obtained.

Proof of the concept of the LEMZ technique in a space environment and its benefit to crystal growth was successfully demonstrated by the growth of InBi crystals in organic encapsulants [96ABB]. The series of experiments was conducted in 1993 aboard the Shuttle Endeavor in an earlier mission (STS-57). The model compound, InBi, was selected for the experiments because of its low melting temperature and its compatibility with organic encapsulants. The flight experiments showed that the presence of the encapsulant improved the molten zone stability, prevented loss of volatile elements, reduced thermal gradients, and suppressed thermocapillary and Marangoni flows [91WIL, 94ABB, 94JEN, 96ABB].The quality of crystals processed without encapsulant was compared to theat of crystals processed by the LEMZ technique and in all cases the encapsulated samples had a lower dislocation density.

Segregation: Convection and Gravity

Besides the advantages of a microgravity environment on zone stability and dislocation density, one of the main goals of crystal growth in a microgravity environment is reduction of convection. The deleterious effects of convection will be discussed below, but first a discussion of the causes of convection and the two main methods of its analysis will ensue. In most terrestrial crystal growing systems, the primary cause for convective flows in the fluid is temperature gradients which in turn creates density gradients. In a gravity field this generates flows known as buoyancy convection which is the most important influence of

gravity in many crystal growth configurations. The convective flow in the crystal is a function of the buoyancy conditions of the crystal growth configuration, the geometry of the system, the thermophysical properties of the fluid, and the orientation of the system with respect to the gravity vector [88MÜL]. The above mentioned temperature gradients also create surface tension gradients when the fluid has a free surface, such as that present in the float zone arrangement, which can give rise to thermocapillary convection when the gradient parallel is to the surface and/or Marangoni convection when the gradient is perpendicular to the surface. In crystals grown on earth, both gravity driven buoyancy convection and surface tension driven convection must be taken into account; however, materials processing in a microgravity environment allows the elimination of gravity driven buoyancy convective flows in the fluid from which the solid grows. This opens the possibility to differentiate between gravity dependent and gravity independent flows and to study their individual contributions to the defect structures and subsequent material properties of the crystals.

The influence of convection on the distribution of impurities and constituents in a growing crystal can be analyzed using two different concepts. First, one can solve numerical solutions of the systems of equations for the convective material and heat transport [88MÜL]. The buoyancy driven convection can be described using this formalism by hydrodynamic equations and solving the appropriate equations for the conservation of heat, species, and momentum. The influence of gravity, g, is contained in the buoyancy term in the Navier-Stokes equation represented by the dimensionless Rayleigh number (Ra) which is a measure of the relative weight of buoyancy forces compared to viscous damping influences in the melt. The action of the surface tension force is not given as a term in the Navier-Stokes

equations because it is not a body force and its nondimensionalized form is given by the Marangoni number (Ma) which is a measure of the force due to surface-tension gradient to the viscous force in the melt.

The second model uses the formalism of the effective segregation coefficient, k_{eff}, which considers the effect of gravity with the aid of a boundary layer model [53BUR]. This model is particularly well suited for a semiquantitative description of the longitudinal segregation and will be used in this study. The details of this model will follow in the SIMS results section.

The problems of crystal growth from the melt mentioned above are in part linked to gravitational and surface tension forces which induce convective flow in the melt [88MÜL]. Steady flow results in macrosegregation of dopant which is a continuous change in the distribution of the impurity along the growth axis. This is undesirable in device development where ideally the electrical and optical properties of all wafers are homogenous from all sections of the bulk crystal. (The equations describing the exact redistribution of the dopant on the macroscale will be given with the SIMS results of this study.) The transition to unsteady oscillatory or turbulent time dependent fluid flow modes result in microsegregation of the dopant and/or certain crystal defects. The unsteady convective modes in the melt interfere with the establishment of controlled mass and heat transfer conditions in the growth system and generate temperature and dopant concentration fluctuations at the interface between the melt and growing crystal. It has been proved that gravity-driven unsteady convection creates dopant striations [72KIM]. It is well established that defects [91SWA] and dopant inhomogeneities [88MÜL] limit device performance, and understanding the

relationship between crystal growth conditions and the resulting semiconductor material properties is key to the future improvement of the GaSb substrate and its lattice-matched system of devices.

Also, the elimination of buoyancy-driven flown in a microgravity environment opens up new possibilities in crystal growth research. Assuming surface tension driven convection can be reduced to negligible values, an ideal, quiescent growth regime is obtainable in which heat and mass transport are decoupled. Growth under this condition is ideally suited for studying the fundamentals of growth, of defect formation and of segregation of solutes under simpler conditions. Moreover, comparison of space and terrestrial results allows one to differentiate between gravity-dependent and -independent causes for various defects.

Other factors affecting convection include so-called g-jitters or variations in the g level in space due to such factors as aerodynamic drag, a gravity-gradient, crew activity, and spacecraft rotational effects [97MAT]. In microgravity experiments with FZ crystal growth, a g-jitters were numerically predicted to stimulate transient convection leading to similar detrimental effects to the crystal growth as in the other types of convection (i.e. unsteady temperature and concentration fields in the melt zone) [94CHE].

One of the method to decrease the convective flow in the float zone is to encapsulate the material, thus one of the driving forces behind the experimental setup in this study. Striations in silicon float zoned on earth and in space were eliminated by a silicon dioxide coating [85EYE, 86CRÖ, 89CRÖ]. The elimination of striations was attributed to the elimination of Marangoni convection. Coating germanium with liquid Pyrex glass decrease the convection in germanium grown in space [86CARa, 86CARb, 90TIL]. Another method used

to reduce the convective flow in the melt is the employment of a magnetic field. This has the effect of raising the critical value of the onset of unsteady convection. Components of the flow are damped through the action of the Lorenz force [87HUR]. This method to control convection was used on GaAs in the same furnace as was used for this study and it was found that one type of striation was completely damped out [95HER].

Previous experiments in a space environment have even proven successful in growing crystal under diffusion-controlled conditions (i.e. without the presence of convection). Both indium antimonide [75WIT] and germanium [78WIT] were grown successfully without the presence of convection. In the latter study, the distribution in an earth-grown reference sample indicated convective mixing in the melt. In both the above studies, striations in the sample due to microsegregation were absent.

<u>Gallium Antimonide: Native Point Defects</u>

GaSb grown from a stoichiometric melt or by liquid-phase epitaxy (LPE) shows a p−type conduction without internal doping with a hole concentration of about 10^{17} cm^{-3} owing to the presence of a large number of native charged defects. Thus, compared with gallium arsenide (GaAs) or indium phosphide (InP), GaSb has a serious drawback in that no high resistivity substrates are available. The microscopic nature of this defect has not yet been completely defined but it is commonly believed to be associated with the Ga antisites Ga_{Sb} [81NAK]. Some authors have described the defect as a double ionizable acceptor due to a $V_{Ga}Ga_{Sb}$ complex [67VAN, 78NOA] while a singly ionizable acceptor model has also been proposed [72BEN]. The nature of this defect will be discussed in more detail in the following sections,

but first a discussion on the effects of the native defect on device processing and research characterization will ensue.

Effect of Native Point Defects on GaSb Devices

Because of the existence of the native defect in bulk grown GaSb, the substrates are either p-type with a carrier concentration of ~10^{17} cm^{-3} at room temperature, or doped (p-type or n-type) with a carrier concentration >10^{17} cm^{-3}. At least two disadvantages with respect to utilizing these wafers for device manufacturing arise from this deficit. The first is that a semi-insulating (SI) substrate is necessary for localization of device features grown onto or incorporated into the substrate. For other substrate materials such as GaAs and InP, a common way of rendering the normally semi-conductive material semi-insulating is to both reduce the concentration of shallow background impurities and to introduce a deep center that pins the Fermi level near the middle of the band gap. Unfortunately, the concentration of shallow background impurities cannot be reduced below the above-mentioned threshold of ~10^{17} cm^{-3} and a high concentration of deep levels cannot be introduced into GaSb substrates. GaP and InP become semi-insulating after copper diffusion treatment due to the overlap of space charge regions formed between the metallic precipitates and the bulk semiconductor. However, this technology does not transfer to the GaSb material system where copper behaves as a p-type dopant and does not significantly increase the resistivity [96ŠES]. Although the existence of certain mid-gap centers in GaSb has been reported [92POLa], their concentration is much too low (10^{15} cm^{-3}) to be able to shift the Fermi level position higher in the band gap. It has been shown that hydrogen atoms can form electrically

neutral complexes with the native acceptors [58HRO, 92POLb], but the efficiency of such a process is low and the complexes are broken by even low temperature annealing at 250 °C. Lithium incorporation is also possible in reducing the acceptor concentration level [65VAN], but this impurity is not desirable in a substrate because it can diffuse easily into the growing layer with unpredictable effects on the device performance.

A second deficit arising from the fact that gallium antimonide exhibits a high concentration of native acceptors is that characterizing the electrical properties of epitaxial layers grown on GaSb by conventional van der Pauw measurements can be difficult. A routine way of avoiding this difficulty is to grow satellite layers on semi-insulating GaAs or InP substrates, but the electrical behavior of the layers is commonly altered by the heavy lattice mismatch between the layer and the substrate. One more deficit is that GaSb substrates are not transparent enough in the 10 μm wavelength range where interesting superlattice photodetectors have been proposed [93MIL]. It is often advantageous to be able to shine light onto these structures from the substrate side, but such an option cannot be realized presently for GaSb-related structures.

Native Defect Nature

To date, the structure of the dominant native defect has not been conclusively identified. Early on, Effer and Etter offered convincing evidence that the background acceptors are related to native defect rather than chemical impurities [64EFF]. Spark source mass spectrometry was performed on a sample of GaSb to determine total impurity content and the only elements detected in a high enough concentration to be considered were Si, C, O,

H and N. Carbon and silicon are the only possible sources of acceptors in GaSb; however, the best material grown by these authors was in a carbon container. Silicon was ruled out as an acceptor by preparing the sample in an oxidizing atmosphere to convert the Si(soln) to SiO_2. The most convincing evidence that the defect is native to the growth is that numerous preparations of GaSb have resulted in an almost constant acceptor concentration. This includes crystals that were either pulled or boat grown, using different purification schemes and crucible materials. Furthermore, zone refining does not have an effect upon the measured defect concentration meaning that if the defect was chemical in nature its distribution coefficient would have to be unity.

From various experimental results, it has been confirmed that the residual acceptor is either related to a deficiency of Sb or an excess of Ga in the solid (i.e. the solid is nonstoiciomentric). The case of an excess of Ga, corresponding to an antimony vacancy, can be immediately ruled out as the residual acceptor since an anion vacancy acts as a donor. In on of the earliest studies in this matter, Reid et al. [66REI] performed experiments in which GaSb crystals were grown from nonstoichiometric melts. It was found that when the Sb concentration in the melt is increased above 60%, reductions in the acceptor concentration of up to two orders of magnitude occurred. However, one must be careful in growth with non-stoichiometric melts as this technique has been recently shown to cause metallic inclusions precluding its use in devices [97DUT]. The calculated solidus existence region of GaSb lies on the p-type side of stoiciometric growth as shown in Figure 2 [90ICH]. The conduction type is converted from p to n in the case of Sb-rich solutions only when the growth temperature is lowered to below 530°C. However, since the eutectic point of Sb and

GaSb is 590°C, crystals grown from a liquid melt are always p-type. More recently, low growth temperature epitaxial techniques such as Molecular Beam Epitaxy (MBE) and Metal-Organic Vapor Phase Epitaxy (MOVPE) have been shown to decrease the acceptor level to 10^{16} cm^{-3} or less with control of the p- and n-type doping [86LEE, 88JOH, 90ANA, 90ROS, 91CHI, 93MEI, 95BOS]. However, the availability of good quality and well characterized GaSb single crystal substrates is still necessary for the incorporation of GaSb into integrated optical devices.

The defect is generally considered a double acceptor. The lower energy level measurements are concentrated in the range of 0.025-0.035 eV depending on the experimental method and the higher energy levels are in the range from 0.06 to 0.12 eV [81NAK]. The considerable range in the upper energy level is the result of the measurement techniques involved, the dependence of the acceptor ionization energy on the compensation ratio, and the misinterpretation of results. (Note that further discussion of the acceptor levels in the bands will ensue as they relate more specifically to Hall and photoluminescence measurements.) Regardless of the energy levels, strong evidence for the double nature of the acceptor exists. This model was first proposed by Baxter et al. [65BAX] who observed a reduction of the acceptor ionization energy caused by lithium diffusion and ascribed it to the interaction between Li$^+$ donors and the doubly ionized acceptor. (Lithium is a rapidly diffusing donor impurity which reacts with negatively charged acceptors to form ion pairs.) It was found that with lithium diffusion, the shallower level of the acceptor disappeared and was replaced by an even lower energy acceptor level.

It has been proposed that the residual acceptor is a Ga antisite Ga_{Sb} [64EFF]. Others authors have offered a defect complex composed of a Ga vacancy Ga antisite $V_{Ga}Ga_{Sb}$ [65VAN, 67VAN]. One argument against this model is that Ga_{Sb} and V_{Ga} act as an acceptor; therefore, they should not for a complex, but repel each other because of the Coulomb force [77KRÖ]. Theoretical thermodynamic defect concentrations in $Al_xGa_{1-x}Sb$ alloy (including GaSb when x=0) were performed by Ichimura et al. [90ICH]. It was determined through the calculations that when the liquid phase is Ga rich, the Ga antisite is dominant and the concentrations of vacancies are much smaller than the antisite concentrations. Edelin and Mathiot [80EDE] also performed calculations with similar results and pointed out that the experimental observations which have been considered to indicate the existence of the complex can be equally well interpreted assuming that the dominant defect is a simple antisite. They point out that experimental results do not positively show the existence of the complex, but rather demonstrate that the dominant defect is not a single vacancy.

Of course the native dominant acceptor defect in GaSb has a central effect on the major characterization techniques for semiconductors. Moreover, the native defect plays a major role in the discussion of the properties of lightly doped n-type materials due to its strong compensation effects. As two of the most important characterization procedures available in semiconductor research, its effect on Hall effect and photoluminescence measurements has been studied extensively. These tests will be reviewed below for both undoped and Te-doped GaSb since both types of crystals were available for this study.

Hall Effect Measurements

Undoped GaSb

One of the earliest studies on the electrical properties was performed at the General Electric Research Laboratory by Leifer and Dunlap [54LEI]. They performed Hall measurments in the temperature range 15-925°K which is just below the melting point. An inversion from p-type to n-type material was found at 357°C as the sample became intrinsic. They also found that one of the difficulties in GaSb electrical measurements is that, due to the low melting point and the high native impurity content, the gallium antimonide lattice never reaches the condition where the number of intrinsic carriers greatly exceeds the number of impurity centers. For this reason, interpretation of the intrinsic resistivity line in terms of the theoretical band gap becomes more difficult than is usual with other semiconductor materials.

A measure of the hole density (and its associated Hall coefficient) is given by the Hall measurements. A narrow-gap material like GaSb shows intrinsic conduction effects at relatively low temperatures; therefore, a clear exhaustion regime, from which a net acceptor density (N_a-N_d), typically does not exist. The electrical conductivity, σ, of GaSb is determined in the whole temperature range by light and heavy holes and by the contribution of the defect or impurity states in the form $\sigma = \Sigma \sigma_i$, where σ_i are the conductivity components of elements i. The conductivity in the extrinsic region is dominated by the previously described acceptor energy level at about 33 to 35 meV above the valence band. The temperature dependence of hole mobility on temperature has been theoretically calculated

by Dutta et al. [96DUT] and has been shown to be influenced by nonpolar and polar optical and acoustic scatterings at higher temperatures. Due to the close proximity of the heavy and light hole bands, intervalley and intravalley scatterings occur. Below about $50°K$, the mobility of the carriers drops quickly. This has been explained by ionized impurity scattering [96DUT] as well as a reduction in mobility due to impurity band conduction [73DOL]. In order to evaluate the thermal activation energy for the acceptor levels, the electroneutrality equation has to be solved using a least squares fit to the experimental data. This will result in the values for the acceptor concentrations and energies. Variable Hall temperature measurements were performed on selected samples and the electroneutrality equation was solved to determine the defect levels and concentrations of the samples. The details of the results of this study will be given in the chapter with the Hall measurement results.

<u>Tellurium-Doped GaSb</u>

The transport properties of GaSb doped with n-type tellurium have been studied in detail for some time due to relatively strong compensation effects compared to other semiconductor materials and some special features of its band structure. Since the native acceptor concentration in GaSb is on the order of 1×10^{17}, one must dope with higher concentrations than this to obtain n-type material. Below this value, the material retains its p-type behavior; however, the acceptor levels show compensation effects which can be discussed in terms of the electrical properties. In n-type GaSb of lower doping levels, there are other peculiarities in the electrical properties which can also be attributed to compensation effects. Even in n-type material which is doped to a level high enough to disregard the effects of compensation,

the transport properties exhibit unusual behaviour due to a relatively low-lying secondary minima. The following will discuss these three cases in more detail.

GaSb lightly doped with tellurium ($<10^{17}$) retains its p-type behavior and results in various degrees of compensation. Ideally, one would like to compensate the crystals with Te to shift the Fermi level toward the conduction band and observe the deeper level of the acceptor state. However, in these samples, in addition to the native double acceptor, an acceptor level has been found at ~70 meV above the valance band edge. It has been suggested that this acceptor level is the result of the complexation of $V_{Ga}Ga_{Sb}$ with Te_{Sb} [96DUT]. This energy level is then confused with the energy levels of the native acceptor [65HAB, 70LAZ, 72KYU, 81NAK]. The mobility of tellurium-compensated p-type GaSb decreases with increasing Te concentration. In contrast to the undoped GaSb, the impurity scattering dominates at all temperatures up to room temperature (for higher concentration levels).

Early on it was noticed in lightly doped n-type GaSb that the mobility at low temperatures *increases* monotonically with increasing electron concentration [61STR]. Later, Baxter et al. explained the reduction in mobility in terms of the effects of compensation on Coulomb scattering [67BAX]. Normally mobility decreases with increasing electron concentration due to the dominant effect of Coulomb scattering from the ionized impurities. The ionized impurity mobility is in general an increasing function of carrier concentration due to the screening effect of the electrons. Conversely, the mobility is inversely proportional to the ionized impurity concentration. In the absence of compensation, N_I is equal to n;

however, with the high concentration of compensating acceptors, N_I varies much more slowly with n. That is, the concentration of N_I can be given by

$$N_I = N_D + N_A \tag{3}$$

or, in the case of n-type samples where $n = N_D - N_A$,

$$N_I = 2N_A + n. \tag{4}$$

For the case of lightly doped material, $n \ll 2N_A$ and N_I is essentially independent of n, thus the variation of mobility is controlled through n. Similarly, it was noticed that in Te-doped material, for low doping levels, the mobility was significantly increased with only a modest addition of lithium [65YEP]. Recall from an earlier discussion that this donor will form ion pairs with the acceptor states, thus decreasing number of Coulombic scattering centers and the ionized impurity scattering. Moreover, Baxter also found that the required hole concentration to fit the variation in mobility with temperature is two to three times that observed in the undoped GaSb. This can be attributed to the doubly ionizable nature of the native acceptor. The deep level is not appreciably ionized even at room temperture in the undoped samples, but of course is completely ionized in the n-type material. The higher hole concentration required to explain the electrical measurements can also be partially attributed to the acceptor states incorporated by the tellurium as mentioned earlier.

Aside from the effects of compensation from the acceptors, highly doped GaSb exhibits a complicated electron transport due to the contributions from the higher subsidiary conduction bands. The Γ band is the lowest lying band at (000) (which of course gives a direct transition to the valance band allowing luminesence). Above this is the L band at the (111) positions with an activation energy , ΔE_C of ~58 to 90 meV [71SZL, 91CHE]. There is a higher band, X, in the (100) positions; however, it only contributes to transport above 180°C and will not be of consideration in the present study. Sagar was the first to discuss the results of Hall coefficient measurements on n-type material on the basis of a two-band model which takes into consideration the Γ and L bands [60SAG]. (This model will be used to discuss the Hall measurement results for the present study and the details will be left for later discussion.) Contrary to n-type GaAs, the Hall coefficient increases with increasing temperature rather than remaining constant due to the difference in the effective masses and mobilities in the two bands. The effective mass of the L band is heavier increasing the density of states in this band to fourty times that of the Γ band. For a constant total number of electrons there is an increasing Hall coefficient with increasing occupation ratio (n_L/n_Γ) since the mobility in the L band is smaller than that of the Γ band. In heavier doped materials, a maximum occurs when the total number of electrons starts to increase at the onset of the intrinsic region, since at that point, R_H drops rapidly. Apart from the two band structure, tellurium introduces donor states in both bands. The donor states below the (000) minimum fuse into the conduction band; however, the states below the (111) minimum keep a finite ionization energy due to the larger effective mass.

Photoluminescence

By impinging laser radiation onto a semiconductor material, energy is transferred to the crystal which is subsequently partially re-emitted as radiation. The radiative emission of photons involves a quantized transition of an electron occupying a higher energy state to an empty state at a lower energy. By measuring the intensity of this quantized transmission as a function of wavelength, one can study the band structure of the crystal and more importantly, determine its defect structure by examining the peaks associated with these defects.

<u>Undoped Samples</u>

The energies of the common low temperature defects present in nominally undoped GaSb are outlined in Table 3. The low temperature PL spectra of high quality unintentionally doped GaSb exhibits about 20 transition in the energy range of 680-810 meV, and Table 3 is a list of the most common. In addition to the defects, several unidentified peaks are present which are typically explained as features of the specific growth method used in a particular study. Other peaks observed include several exitonic transitions and even LO transitions related to bound exitons.

The presence of the native defect strongly influences the photoluminescence (PL) of GaSb; typically it gives rise to an intense recombination band (A) centered at about 777 meV [72JAK, 76RÜH]. For this reason, PL has been frequently used to evaluate material quality through the intensity ratio of defect-related emissions and nominal exciton recombinations

Table 3 - Defect levels in undoped GaSb (compiled from [72JAK, 87NIC, 91CHI, 95JIA, 96BIG, 96DAN]).

Defect Name	Defect Energy (meV)	Type of Defect
D	800-803	Band-acceptor transition of unknown origin
A	777	Donor-to-acceptor pair recombination involving the neutral native double acceptor (D^0-A^0 transition)
A-LO	746	LO-phonon replica of the A band
B	758	Acceptor B
B-LO	728	LO-phonon replica of the B band
A^-	710	Conduction band-to-acceptor pair recombinaiton involving the singly ionized native double acceptor (C-A^0 transition)
A^--LO	682	LO-phonon replica of the C band
FE	810	Free-exiton
BE_1-BE_4	805.4, 803, 800, 796	Exitons bound to the neutral state of the native acceptor, BE_1-BE_4 in order shown
BE	792	Exiton bound to a neutral acceptor level of unknown origin

[94VAR, 95BOS]. As an example, in Liquid Phase Epitaxy (LPE) growth, the low-temperature PL spectrum of GaSb crystal grown from stoichiometric melts [73RÜH] and Ga-rich solutions [92WUa, 72JAK] is dominated by the BE_1-BE_3 transitions and recombination at the native acceptor level A, while it is dominated by a BE_4 transition in material grown from and Sb-rich melt [72JAK, 90ANA, 85BAR, 92WUb]. The accompanying doping level in these samples was also reduced to about 3×10^{16} cm^{-3} with a corresponding increase in hole mobility from 540 to 700 cm^2/V·s [72JAK]. Recall from the discussion above that the native

acceptor is caused by a Sb deficiency in the crystal growth and non-stoichiometric growth with excess Sb helps in the reduction of the acceptor state and it corresponding PL signal.

<u>Tellurium Doped Samples</u>

The low temperature defects related to the tellurium dopant are outlined below in Table 4. As explained by Bignazzi et al., the A, T, and C' bands, the only bands present at higher doping levels, broaden and shift toward higher energy levels with increased doping [96BIG]. Broadening occurs in the low energy tail by band-gap narrowing due to carrier-carrier and carrier-impurity interactions and to formation of band tails due to doping inhomogeneities and it occurs in the high energy tail due to conduction-band filling. The peak position of the PL bands in heavily doped samples is primarily determined by the conduction-band filling due to the low density of states of the conduction band which is dominate over any bandgap narrowing effects. The PL bands are shifted on the order of the Fermi level shift. The above study was determined in crystal grown with a low native acceptor concentration. Otherwise, investigation of Te doped samples with a high native acceptor concentration ($\geq 10^{17}\,\mathrm{cm^{-3}}$) will be of limited study since the energies of the Te-related transitions depend on the Fermi level position, which, in turn, depends on the free electron concentration that can be hardly obtained in the low ranges because of the high native acceptor concentration. A PL study by Basu on vertical Bridgman grown samples with high native acceptor concentration and moderate to high Te doping levels illustrates this point with observed broad spectra [92BAS].

Table 4 - Defect levels in doped GaSb (compiled from [72KYU, 76RÜH, 79LEB, 85BAR, 87NIC, 89CHE, 92WUb, 95JIA, 96BIG]).

Defect Name	Defect Energy (mev)	Type of Defect
D	808	Related to the presence of EMA unintentional and/or Te shallow donors (present in undoped samples also).
T	~720-740	Conduction band to acceptor transition related to the Te donors. Evidence suggests that it is likely a defect complex (C-$V_{Ga}Ga_{Sb}Te_{Sb}^{0}$). The peak energy increases with increasing Te concentration.
T-LO	694	LO phonon replica of the T band.
C'	701	Merging of C and T–LO bands at higher doping levels.

Extended Defects

Dislocations in semiconductors can be efficient gettering sites for impurities which act as recombination centers [89WON]. They can also affect the dark currents, breakdown voltage and consequently the sensitivity of photodetector devices because they are considered to produce midgap states in the bandgap; therefore, a reduction in the dislocation density is highly desirable [80TAK]. Dislocations in the growing crystal are typically generated by stresses caused by contact with a growth container and also by temperature gradient induced stresses. Due to the LEMZ experimental setup, the latter is of primary concern in this case. Herrmann and Müller have calculated the temperature and resulting stress distribution for float-zone microgravity GaAs crystals with various zone height to zone diameter ratios (h/d) [95HER]. They showed that the interface curvature strongly influences the stress distribution

in the growing crystal which had a direct correlation with the observed EPD. A h/d ratio of 1.0 resulted in the most favorable experimentally observed EPD count in the grown crystal.
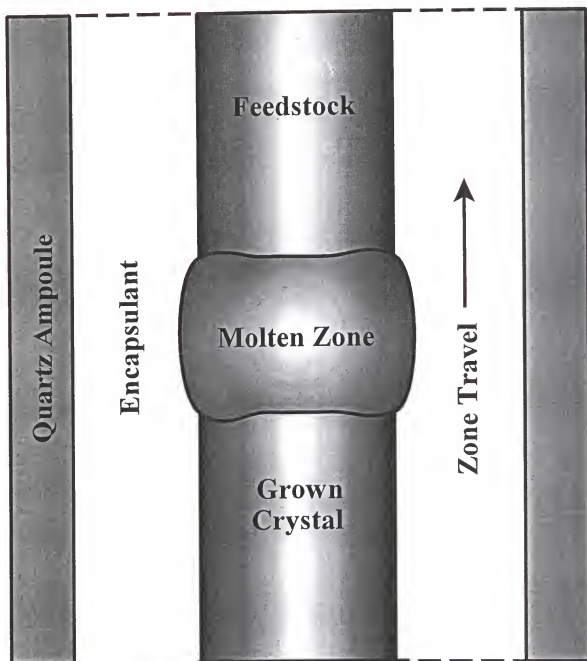
Figure 1 - Schematic of the Liquid Encapsulated Melt Zone crystal growth technique.
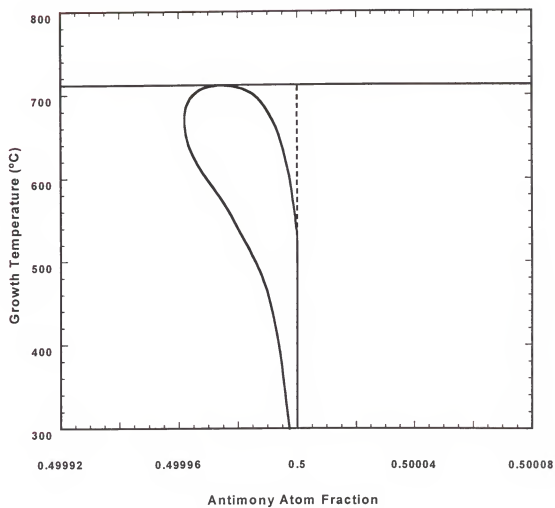
Figure 2 - Calculated solidus of GaSb (after [90ICH]).

EXPERIMENTAL

Sample Processing

Overview

GaSb crystal were grown by the LEMZ technique as part of the Commercial Float Zone Furnace (CFZF) payload that was part of the STS-77 mission operations launched on May 19, 1996 aboard the Shuttle Endeavor. On-orbit operations were carried out by astronaut mission specialists Marc Garneau, Ph.D., and Andrew Thomas, Ph.D. Also, experimental commands were sent via telescience by the experimenters from mission control in Houston, Texas.

Four GaSb ampoules were flown, two of which were undoped and the other two doped with tellurium. Three of the ampoules were processed with the fourth one serving as spare. All microgravity-processed samples were 62 ± 2 mm long and 16 ± 0.4 mm in diameter. The samples were encapsulated with an eutectic salt mixture of sodium chloride (NaCl) and potassium chloride (KCl). This system was contained within a double wall quartz ampoule configuration in a partially evacuated argon environment. In addition, two undoped and two doped GaSb samples, with diameters ranging from 7.85 to 9.17 mm, were processed on ground in ampoule configurations similar to those used in microgravity.

The melting and processing of the samples were conducted in a Double Paraboloid-Ellipsoid Mirror Furnace (ELLI-FM), property of the Dornier Deutsche Aerospace Company out of Friedrichshafen, Germany. The melting of the crystals was achieved with the ELLI by focusing radiation, emitted by a halogen lamp, onto a narrow band around the hermetically sealed salt-sample system, thus establishing a float zone. Once a stable zone was achieved, translation of the ampoule along its axis was executed at different rates to effect the desired crystal growth. The ELLI-EM furnace, shown in Figure 3, was stationed at the University of Florida for the purpose of training the astronaut crew and performing ground testing. The EM model is a ground-dedicated copy of the flight furnace. After processing, the samples were sectioned and analyzed with: chemical etching to determine EPD and to resolve dopant striations in the doped crystal; photoluminescence and Hall measurements to examine the near bandgap defects and electrical properties of the wafers, and SIMS measurements on the doped samples to determine the redistribution of tellurium on both the micro- and macro-scale in the crystal.

Ampoule Design and Sample Preparation

Single crystals of GaSb were acquired from ATRAMET Inc. out of Farmingdale, New York. A partnership was established with the manufacturer to supply eight single crystal rods of GaSb at cost and show the difference between commercial price and manufacturing cost as an in-kind contribution to the CFZF project. In return, ATRAMET Inc. was named as an official partner to the University of Florida for the duration of the project.

Eight GaSb single crystals, grown by the (LEC) technique, were purchased from ATRAMET Inc. Figure 4 shows a typical as-received GaSb crystal from the manufacturer. Table 5 shows the properties of the crystals as received from the manufacturer. All crystals were grown by ATRAMET along the <100> axis with deviations of less than $0.6°$. The top four samples in the table were utilized for microgravity processing with the remaining four dedicated to ground activities. The diameter of all samples dedicated to ground-based processing was reduced to ~8-9 mm to assure that stable molten zones could be obtained on ground. Recall that only small diameter samples can be processed on ground due to the limitations imposed on the stability of molten zones by the Earth's gravitational acceleration. The length of the ground-based crystals remained unchanged from the as-received crystal. The length and diameter of the flight samples was maintained.

The details of the ampoule design criteria and of the ampoule integration are given by López [97LÓP]; a summary is given as follows. The selection of an encapsulant material compatible with the growth of GaSb single crystals requires the consideration of certain requirements. The following aspects were considered in the selection process:

5) Melting temperature below that of GaSb ($712°C$)

6) Negligible reactivity with the GaSb line compound

7) Optically transparent above its melting temperature

8) Negligible volatility above its melting temperature

9) Good wetting behavior with the line compound

A eutectic salt mixture was chosen as the encapsulant for the GaSb system since it met all of the above criteria. The eutectic mixture of 50 mol% NaCl and 50 mol% KCl is

Table 5 - Processing environment and properties of crystals as given by the supplier.

Sample	Dimensions Diameter × Length (mm)	Dopant	Processing	300 °K Carrier Concentration ($cm^{-3} \times 10^{17}$)	Mobility (cm^2/Vs)
UFL1-GaSb	16.3 × 63.9	Undoped	Space	1.2	323
UFL-GaSb (Spare)	15.6 × 62.3	Undoped	Space	1.2	348
UFL2-GaSb	16.1 × 62.1	Te	Space	11	1609
UFL3-GaSb	16.1 × 62.0	Te	Space (aborted run)	12	892
53/1	15.8 × 61.4	Undoped	Earth	1.3	348
53/2	15.8 × 67.2	Undoped	Earth	1.3	244
59/3	16.1 × 60.0	Te	Earth	14	1150
59/4	16.1 × 62.2	Te	Earth	18	1641

typically used in the LEC growth of GaSb. The mixture melts at 645°C or about 65°C below the melting temperature of the GaSb compound. Previous research by mass spectroscopic analysis has shown that typical GaSb single crystals grown by the LEC technique with this encapsulant have impurity concentrations of the encapsulant elements of less than 0.5 ppm by weight [80MIY]. These concentrations are equivalent to those of other impurities found in the crystals such as silicon, zinc, sulfur and other elements. The mixture is optically opaque (white color) in the solid state but optically clear in the liquid phase. The rate of evaporation of the eutectic salt has been measured on LEC growth systems at values less than 35 mg/hr [80MIY].

Figure 5 shows a schematic of the approved final ampoule design. This configuration was utilized in both, microgravity and ground-based studies. The salient features of the ampoule assembly include the following:

- Salt-encapsulated, rod-shaped GaSb single crystal: 62 ± 2 mm long x 16 ± 0.4 mm in diameter for all microgravity-based processing. For the ground-based studies, the GaSb rod diameters ranged from ~8-9 mm with lengths ranging from 60 to 67 mm.

- Samples were held in place by a dimple-graphite-pin configuration. Graphite rings, on either end of the crystals, were fastened to the rods by inserting a molybdenum pin through the components. Movement of the rings along the axis of the ampoule was restrained by dimples fused into the inner ampoule quartz tube. This prevents the feedstock and growing crystals from being pulled together during processing by the surface tension of the float zone.

- Double wall (inner and outer ampoules) quartz crucible for the containment of any toxic vapors. Outer ampoule dimensions were 190 ± 2 mm long and 34 ± 0.05 mm in diameter. The outer ampoule outside diameter was held to a very close tolerance so as to minimize the misalignment of the ampoule relative to the heating focal point of the mirror furnace. Each ampoule was independently sealed to provide redundant isolation of internal environments.

- Separation of the inner and outer ampoules by means of graphite felt and rings. This feature was incorporated so as to assure the structural integrity of the ampoules was maintained through the critical shuttle launch stage.

- Free volume cavity to allow for the expansion of the salt encapsulant upon melting.

- Partial vacuum argon environment in both inner and outer crucibles. The inner ampoule was sealed under an argon environment lower than 10^{-4} mTorr in pressure and the outer crucible was fused shut under an argon pressure of 150 mTorr.

All moisture-absorbing components such as graphite felts, rings, eutectic salt, and ampoule identification molybdenum tags were degassed under vacuum at high temperatures prior to assembly. The graphite and molybdenum tags were degassed at 1100 °C for a period of one hour while the encapsulant salt was degassed at 550 °C for a period of no less than eight hours.

Processing Equipment

Processing of the ampoules was conducted in a double paraboloid-ellipsoid mirror furnace (ELLI-FM) property of the Germany-based Dornier GmbH company. The mirror

furnace was launched, along with the ampoules, in the McDonnell Douglas' SPACEHAB-04 Module aboard the Shuttle Endeavor (STS-77) on May 19, 1996. STS-77 was a nine day science mission. The SPACEHAB-04 Module, shown in Figure 6, is a commercial laboratory platform designed for use aboard the space shuttle in the forward part of the cargo bay. Its purpose is to augment the shuttle's middeck working space providing additional laboratory and support systems for microgravity experimentation.

The ELLI-FM mirror furnace was designed and developed to meet the scientific requirements for the processing of semiconductor crystals in a microgravity environment aboard the space shuttle. The facility can melt materials with a melting point of up to 1600°C. All processing is conducted in quartz glass ampoules of up to 40 mm in outside diameter. The ampoule assembly is mounted into a metallic holder which provides the mechanical and electrical interface to the facility. Radiation, emitted by a halogen lamp, is brought into focus around the sample to melt it and thus establish a molten zone. The sample can be translated along its axis at rates ranging from 0.06 to 600 mm/hr with rotation rates ranging from 0 to 20 rpm. Lamp pulsing is available for interface demarcation (i.e. a deliberate reduction in lamp power by ~15% for 5 seconds). The experiments can be observed directly and by two video cameras. This allows experiment control by the flight crew or by the investigators on ground by means of telescience commanding. In addition, still camera pictures of the molten area can be taken. Automatic processing files are required for all microgravity-based experiments. Up to 76 parameters can be specified in these files including critical processing variables such as lamp voltage, sample translation and rotation speed, heat-up rate, and cool-down rate. All critical variables can be adjusted during the

experiments. The definition of the processing parameters was conducted through a series of extensive ground testing performed on ampoules identical to the flight configuration. Figure 7 shows a picture of Mission Specialist Marc Garneau, in the SpaceHab-04 Module next to the ELLI-FM furnace during flight.

<u>Processing Procedures</u>

Once in orbit, loading of the ampoules into the furnace was conducted by the mission specialist. The automatic processing feature was utilized in all the experiments. The processing sequence can be summarized as follows:

1. Ampoule loading into furnace by the mission specialist.

2. Ampoule translation from loading to processing stage.

3. Heat-up.

4. Heat soak.

5. Power adjustment to establish the molten zone.

6. Crystal growth at various translation rates.

7. Cool-down.

8. Ampoule unloading.

Figure 8 shows a typical timeline of processing events as conducted during the microgravity-run experiments.

Steps 2, 3, 4, 6 and 7 were executed by means of the automatic processing feature. The power adjustment phase was controlled from ground by the experimenters at the Payload Operations Control Center (POCC) of the Johnson Space Center in Houston, Texas. Heat-up

was conducted at rates ranging between 0.5 and 1.0 V/min up to a predetermined value of 18.5 V obtained from ground testing. All samples were allowed to heat soak at a predetermined lamp power for a period of 30 minutes, at which time the power was gradually incremented by the experimenters, by means of telescience, until a stable float zone was established. Real-time video downlink was made available to experimenters about 90% of the processing time. Once a stable float zone was established the automatic processing feature was allowed to take over and translate the ampoule to effect the desired crystal growth. Microgravity growth rates ranged from 1 to 6 mm/hr. Lamp pulsing was utilized occasionally to demarcate changes in translation speed. Lamp power was adjusted occasionally during the growth phase according to the experiment conditions.

The processing of the ground ampoules was conducted in a similar fashion as explained above. The processing chamber of the ELLI-EM ground furnace was evacuated to a pressure of around 20 mbar so as to minimize the effects of convection on the external environment of the ampoules. Ground-based growth rates ranged from 3 to 18 mm/hr. Lamp power pulsing was not utilized on ground testing. Real-time video was available and recorded 100% of the processing time.

Sample Characterization

Hall Measurements

The application of external fields, such as electric and magnetic fields, causes electric currents to flow in semiconductors. Measurements of this flow and its associated effects

provides important information about the semiconductor such as the impurity content, carrier concentration, and mobility. Moreover, the temperature response of these parameters gives further information about the band structure of the sample. The Hall effect was first discovered by E. H. Hall in 1879 [1879HAL]. Classically, measurement of the Hall effect was done by placing contacts on a bar or a sample in the bridge shape. A modification of the measurement technique to include arbitrary shapes was first outlined by van der Pauw [58VAN]. Due to its ease of use and nondestructive nature, the van der Pauw technique was used chosen for the Hall measurements in this study. This test method requires a singly connected test specimen which is homogeneous in thickness and electrical properties. The methodology for this technique as well as that for bar and bridge specimens is outlined in ASTM F 76-86 [86AME] and a summary description of the technique as it relates to the present experiment is as follows.

First, samples surfaces were degreased in acetone and four indium pressure contacts were placed at equal distances along the periphery of the sample. The contacts were sufficiently small and located at the periphery of the sample to prevent erroneous measurements. All combinations of contact pairs were checked for a linear current-voltage characteristic in both polarities with an oscilloscope. Samples were then placed in a holder between two poles of a variable flux electromagnet. For measurement purposes, the poles of the magnet could be interchanged electrically. A current source passed current up to 0.1 A through two contacts of the sample while voltage was measured with a voltmeter across the other two contacts. The magnetic field dial setting on the electromagnet was ±5000 Gauss for all samples while the actual fluxes at the sample for this setting was measured to be approximately 4350 and

-4480 Gauss. A total of 20 current/voltage measurements were taken for each sample according to the standard switching sequence which is outlined in ASTM F 76-86. For the variable temperature measurements, a similar procedure was followed except the sample was cooled by a Helium cryopump down to approximately 30°K. The sample and cooling apparatus was surrounded by an aluminum sleeve which was pumped down by a mechanical pump to prevent convective heat loss. Again, the current/voltage curve was checked for linearity prior to each measurement.

From this technique, the Hall coefficient, Hall mobility, carrier concentration, and resistivity of each wafer was determined. Experiments were performed at room temperature on all sectioned samples to determine the change in these electrical parameters as a function of growth distance, to measure the results against the as-received material, and to compare the materials grown in different gravity environments. Based on the room temperature results, variable temperature Hall measurements were also performed on selected samples to further determine the electrical characteristics of the material in relation to its band structure.

<u>Photoluminescence Measurements</u>

Photoluminescence is one of the most powerful and versatile forms of optical spectroscopy used in semiconductor characterization. Moreover, this purely optical technique is inherently nondestructive. With this method, a wealth of information about band structure and impurity and defect levels is available. Photoluminescence was performed on the samples that were used in variable temperature Hall measurements to complement the data.

The tests were performed at the National Renewable Energy Laboratory (NREL) out of Golden, Colorado. Energy resolved photoluminescence was performed at 4.5 °K at variable input powers ranging from 0.05 to 13 W. The spot size was 250 μm in diameter which translates to power densities of 1 to 26.5 W·cm^{-2}. Also variable temperature measurements were made on the undoped samples to better identify and determine the temperature evolution of the acceptor and excitonic transitions. The laser was a Spectra Physics Model 127 HeNe continuous wave laser at 632.8nm and the chopper was a Stanford Research Systems Model SR540. The combination of a Spex Model 1680 Spectramate Double-Grating Monochromator/Spectrometer, a North Coast Optical Systems and Sensors Model EO-817 Germanium Detector and a EG&G Instruments Mode 5210 Lock-In Amplifier obtained the signal strength at each wavelength.

<u>Secondary Ion Mass Spectrometry Measurements</u>

Secondary Ion Mass Spectrometry is a surface analytical technique where trace elements in a matrix can be detected with a dynamic range of up to 5 orders of magnitude. The scale of these measurements can be localized to determine the variation of impurities in a semiconductor substrate. SIMS was performed on the Te-doped ground and microgravity grown crystals to determine the dopant distribution in the grown crystals. The results of these experiments were then compared to determine the effect of gravity on the distribution.

The sample was placed in a high vacuum chamber and Cs$^+$ ions were projected onto the target with 1.2 kV of energy. The raster size of the beam was 250µm and the primary beam diameter was 50µm. The ion beam created momentary motion of the atoms known as a

collision cascade and some of these atoms overcame the surface binding energy and were sputtered off the sample as secondary ions. The ions emitted in this manner were guided to a mass spectrometer by an extraction voltage and from this the total concentration of Te was compared to that of a know standard.

Measurements were performed in both the so-called linescan mode and individual point measurements were also taken. The seed and tail of the Te-doped microgravity sample had linescans performed in the center of the crystal along the growth axis. Only the seed section of one of the ground based samples was available for SIMS testing on the Te-doped ground based samples due to the post LEMZ processing crystal structure (see [97LÓP] for a detailed explanation of the final structure). The SIMS linescan data was then examined on the macroscale by comparing the Te concentration in the crystal to the equations for convective and diffusive controlled growth.

Chemical Etching

Chemical etching can be classified as either selective (also called preferential) or polishing. The former is used for revealing defects on the surface. The basic requirement for a defect etchant is that it should remove material from the crystal surface at a constant, substantial rate and at the points at which defects emerge, the etch rate should be larger (or less commonly, smaller) than the perfect crystal. Etch pits are produced in areas with local strain such as dislocations. Moreover, striations caused by dopant microsegregation can also be produced in a selective etch in the oxidation-reduction reactions that operate during etching. Electron transfer during the reactions varies with the dopant distribution and the

associated change in local conductivity of the surface. In general, selective etches are reaction limited and local variation in the solid produce different reaction rates. Conversely, the polishing etches are commonly diffusion limited processes since variations in dissolution rate, which depends on the properties of the solid, become irrelevant.

The defect etchant used for this study was a variation of the method used by Brown et al. [82BRO], The procedure including initial polishing and grinding is outlined below:

- Grinding: with 800 grit and 1200 grit SiC paper (U.S. grain sizes)

- Polishing: Polishing was done on fine rayon cloths using water-based diamond suspensions. Samples were polished to a mirror finish with diamond suspensions containing particle sizes of 15 and 6 mm.

- Polish etch #1: Polished samples were subjected to a chemical polish consisting of 2 HF/18 HNO_3/40 CH_3COOH (Acetic Acid) to smooth out the surface and eliminate the mechanical damage from the grinding and polishing steps. The polish etch was conducted at room temperature for two minutes.

- Polish Etch #2: A second polish etch consisting of 1 vol.% Br-methanol was incorporated to the procedure in order to enhance the reproducibility of the process. Samples were transferred directly, without rinsing, from polish etch #1. Typically, a solution containing 50 ml of methanol and 0.5 ml of bromine was prepared. This step was conducted at room temperature for a duration of 30 seconds.

- Selective Etch: A solution of 2 HCl:1 H_2O_2 (50%) was used to reveal growth features on all cut sections. Mixing of hydrochloric acid and hydrogen peroxide results in a strong bubbling exothermic reaction. The solution was allowed to react completely

before placing the sample in it. The sample was then transferred directly, without rinsing, from polish etch #2. The etching was allowed for up to five minutes under constant stirring as the etchant produced bubbling at the surface of the crystal. Bubbles on the surface of the crystal were found to produce undesired surface pitting if sample stirring was not performed properly. A new freshly prepared chemical etch solution was used for each sample.

Polish etch #2 and the selective etch were those used by Brown; additionally, it was found that the reproducibility of this process was enhanced if it was preceded with polish etch #1. For each chemical polishing step there was an oxidizer (HNO_3, H_2O_2, and Br_2) which served to oxidize the surface. In polish etch #1 and the selective etch, there was a complexer (HF and HCl) to facilitate removal of the oxidized species and make it soluble in the etching solution. Finally, in polish etch #1 and #2, acetic acid and methanol were added as a diluent.
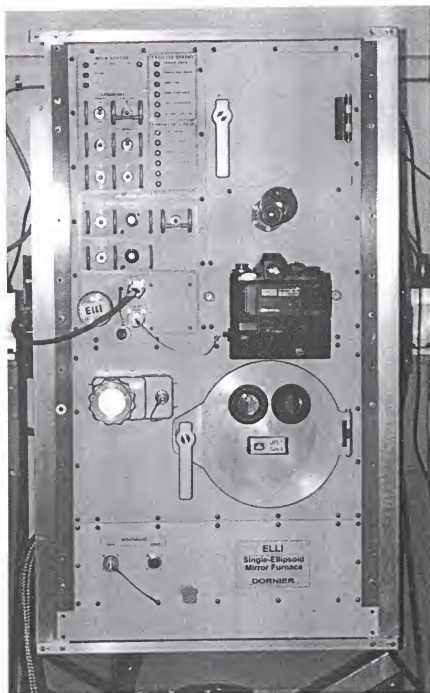
Figure 3 - ELLI-EM ground based furnace used to train the mission specialists and regrow the ground-based samples.
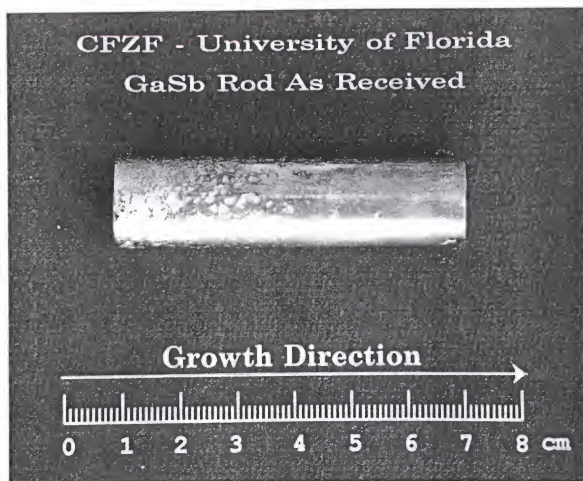
Figure 4 - Typical as-received GaSb crystal.
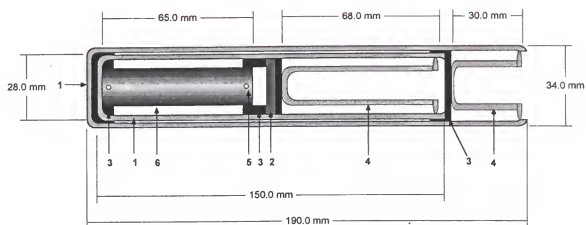
Figure 5 - Schematic diagram of the ampoules: 1) double quartz walls for safety considerations, 2) graphite felt and 3) graphite holders to isolate the sample and ampoules, 4) quartz sealing cap, 5) molybdenum pin through the end of the crystal fastened to the graphite holder, and 6) encapsulant. The internal environment of the ampoules was argon under partial vacuum.
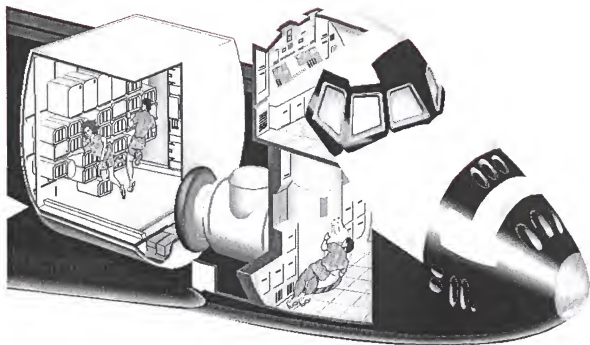
Figure 6 - Schematic of the SPACEHAB-04 Module as configured for the Shuttle system.
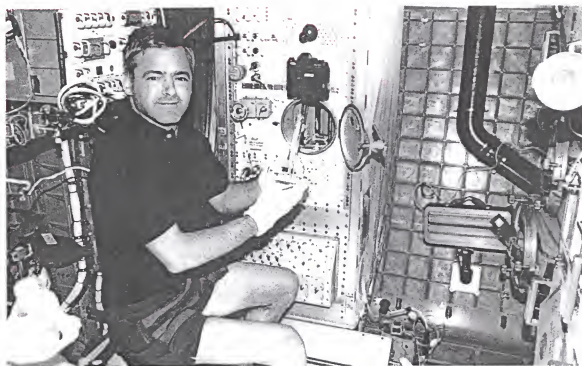
Figure 7 - Astronaut Marc Garneau holding a sample next to the ELLI-FM furnace in the SPACEHAB-4 Module during the mission.
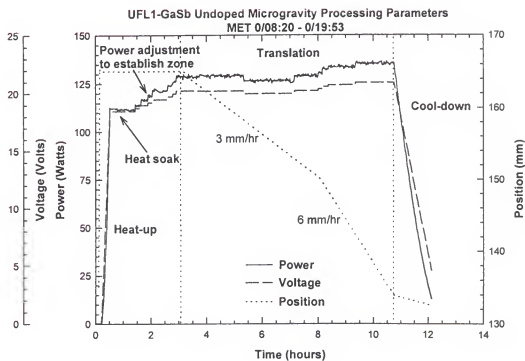
Figure 8 - Typical timeline of processing events as conducted in microgravity.

PROCESSING RESULTS AND DISCUSSION

Crystal Growth

The master's thesis by Carlos López [97LÓP] concentrated in great detail on the processing parameters and their resulting effects on the crystal growth by the LEMZ technique. The highlights of his study along with some new findings and clarifications are presented below as they are relevant to the understanding of the present investigation. Figures 9 and 10 show the resulting GaSb crystals grown in space and on ground. For the microgravity experiments, single crystals were obtained from all three samples over the entire length of the rods. Of the four samples processed on ground, two were single crystals, with the remaining two exhibiting polycrystalline structures in some sections of the rods. Back-reflection Laue X-ray analysis confirmed single crystallinity was obtained and the all microgravity-grown GaSb crystals were grown with the [100] direction of the seed.

There was a remarkable difference in diameter control between the microgravity- and ground-grown crystals. Example diameter measurements for each case are shown in Figures 11 and 12. In all space-processed samples, the initial crystal exhibited a reduction in diameter, contained within the first 6 mm of growth, followed by a gradual increase in cross section that approached but did not reach the feedstock diameter. Ground-processed samples, on the other hand, maintained a stable cross section throughout the entire newly grown crystals.

The difference in the diameter control of the space and terrestrial crystals is due to the influence of the shape of the molten zone on the diameter of the crystal, particularly at the tri-junction between the growing crystal, melt, and the surrounding fluid. In the space grown samples, when the diameter of the regrown crystals reached a minimum, the angle between the growth axis and the tangent to the liquid meniscus was equal to about $44°$. Near the beginning of crystal growth this angle was observed to be around $20°$ and after the minimum diameter it was observed to increase to values as high as $52°$. As discussed by Eyer et al. [84EYE], the stability of crystal shape can be predicted using the criterion defined by Surek [76SUR]. The criterion indicates that a critical growth angle, ϕ_o, between the melt meniscus and the growth axis is necessary for a stable growth diameter, and, if this angle is not realized, the crystal diameter will adjust itself to reach that angle.

To illustrate this concept for the microgravity crystals in the present experiment, the evolution of the shapes of both the molten-zone and regrown crystal is shown schematically in Figure 13. The rapid initial reduction in the cross section of the microgravity grown crystals is consistent with a critical angle of greater than zero. In the beginning of crystal growth, the observed angle was smaller than the critical angle (i.e. $\phi<\phi_o$ in the figure) due to the 8% volume reduction upon melting. Consequently, the diameter decreased in order to build up more molten material and increase the angle. After this rapid decrease in diameter, the critical growth angle was approached and the diameter approached a minimum value. As explained by Surek [76SUR], when the crystal diameter reached a minimum, the growth angle is temporarily equal to the critical angle. The critical angle for the present experimental setup with an encapsulated zone was estimated to be around $44°$. The angle measured is

shown schematically by the middle diagram in Figure 13 and is shown in an actual processing photograph in Figure 14. The angle subsequently increased to about 52° as the diameter increased back toward the feedstock diameter. The growth angle surpassed the critical angle as the diameter was increased once again. The system would reach steady state in an exponentially decaying oscillatory manner. As shown in Figure 11, the diameter approached the feedstock diameter almost completing one period of oscillation.

On the other hand, the ground-processed samples maintained a stable cross section throughout the entire regrown crystal due to the effects of gravity on the shape of the molten zones. Since the gravity vector was parallel to the growth direction, the molten zones attained a pear-shaped profile, thus leading to the immediate attainment of the stable growth angle [84EYE].

The critical growth angle measured in this experiment compares with an angle 28° measured by Tegetmeier in *unencapsulated* GaSb [96TEG]. The difference between the measured critical angle for the present investigation and that for unencapsulated samples is believed to be due to the influence of the encapsulant on the contact angle at the tri-junction. The encapsulant is expected to reduce the line forces along the external boundaries of the crystal and the melt at the triple phase boundary [78WEN].

It should be emphasized that the initial diameter reduction is mainly due to the volume shrinkage upon the formation of the molten zone. The volume shrinkage can be reduced by allowing a controlled movement of the seed and feedstock material toward each other as the molten zone develops. This concept works adequately on the ground, but for space experiments it would seriously complicate the design and fabrication of flight worthy

ampoules. Another method to eliminate the initial diameter reduction is to add excess material in the section where the float zone will first be established in order to initially create the critical growth angle necessary. This approach was successfully implemented by Cröll and Benz [97CRÖ] for floating-zone growth of unencapsulated GaSb in microgravity.

For both growth microgravity and terrestrial growth conditions, the shape of the last section to solidify exhibited a protrusion as shown in Figure 9. This is due to the fact that the final molten zone experienced solidification from two fronts, top and bottom, that, given the 8% volume expansion upon solidification, forced the final freezing zone to bulge out. Also, with the initial diameter reduction in the growth of the crystals, a mass of GaSb built up in the molten zone and migrated toward the end of the crystal.

The furnace lamp power input required to establish a stable molten zone in space was considerably lower than that required on ground. Ground testing trial runs on samples with 16 mm diameters required lamp power inputs of 155 Watts or higher as compared to about 128 Watts in space, a reduction of close to 17%. Moreover, the terrestrial processing conducted on 9 mm diameter samples with stable molten zones required about as much lamp power input as that in space with 16 mm diameter crystals. The lower power requirement in space is believed to be due to the reduced convection in the halogen lamp, the furnace, and in the molten salt encapsulant. Consequently, more of the filament output was delivered to the crystal and more of that which was delivered was able to remain in the processing zone. In addition, it was observed that the molten zone length of the encapsulant, particularly above the center of the molten GaSb zone, was considerably larger for the terrestrial samples which again indicated convection in the encapsulant.

For ground processing, stable molten zones could not be maintained for an extended period when the sample diameter was larger than 9 mm. For these samples, the maximum stable float zone length was determined to be around 9 mm. For space processing, on the other hand, stable zones as long as 20 mm were maintained for several hours during the experiments. Typical values ranged from 10 to 20 mm. The maximum stability length of the encapsulated float zone was not tested in microgravity because the length of the crystals was small compared to the predicted Rayleigh stability limit (~50 mm) given by [1892RAY]

$$l_{max} = \pi d \tag{5}$$

where d is the diameter of the crystal. For ground-based tests, however, the stable zone length was found to exceed the length predicted by Hewang's model for an unencapsulated float zone [56HEY]. The model predicts that the maximum length of an unencapsulated vertical zone is determined by the gravity level and equilibrium between the surface tension and hydrostatic internal pressure as

$$l_{max} = 2.84 \left(\frac{\sigma}{\rho g} \right)^{\frac{1}{2}} \tag{6}$$

where σ is the surface tension, ρ the effective density and g the gravitational acceleration. According to this model, the limit of stability for unencapsulated GaSb molten zones on ground is 8 mm with $\sigma = 473 \times 10^{-3}$ N·m^{-1} [96TEG] and $\rho = 5.6$ g·cm^{-3}. The main factor contributing to the increased encapsulated molten zone stability is believed to be the reduced density difference between liquid GaSb and the encapsulant which reduces the hydrostatic

forces acting across the GaSb/encapsulant interface. The observed increase in the stability limit can also be predicted by the effect of the encapsulation on the static Bond number [94LOW]. The dimensionless parameter represents the ratio of gravitational to surface tension forces.

For a given power input, the zone length during the processing was found to vary inversely with the translation rate. An increase in the translation speed resulted in a decrease in the zone length as more material was brought into the zone at the melting interface than that removed at the freezing interface. Also, the zone length decreased as the molten zones approached the ends of the samples because of increased thermal conduction through the rod ends which were in direct contact with graphite holders (see Figure 5 in the Experimental section).

The etched cross-sections of microgravity samples revealed monocrystalline structure along the entire length of float zoned material confirming the results of the X-ray analysis. It is worth noting that the unprocessed LEC-grown crystal etched at a faster rate the regrown float-zoned regions which can be an indicator of the enhanced quality of the reprocessed crystals as compared to the starting material. The areas of the crystals which grew under the final power-down conditions contained a polycrystalline structure on one side of the crystal within the last 5 mm of growth. A clearly demarcated, slightly convex, boundary at the mid-section of the pronounced material protrusions was seen where the top and bottom interfaces converged.

The etching also revealed growth striations across the tellurium-doped samples. Changes in Te concentration in the GaSb are caused by microsegregation of the dopant during growth

of the crystal. The cause of microsegregation will be discussed in greater detail in the SIMS results and discussion chapter, but for now it will be mentioned that changes in Te concentration allow different etch rates to be realized which reveals the shape of the solid/liquid interface at that location. Note that, for the undoped crystals, the striations were either very faint in portions of the crystal to nonexistent.

Figures 15 and 16 shows a photograph of the Te-doped space-grown sample depicting striations. Some striations observed on parts of the outer surface of the regrown crystals were found to correlate with the distance the sample moved in one period of rotation. They are classified as rotational type striations. In general, the rotational striations penetrated the internal structure of the crystal and quickly faded and disappeared as one progressed toward the center of the crystal. The density of rotational striations observed on the microgravity float zoned crystal was a mere fraction of that observed on the ground-grown starting materials, as shown in Figure 17. There were also a low density of faint nonrotational striations which were most likely causes by disturbances to the melt zone such as g-jitters (see the Literature Review for the background on g-jitters).

Note that the strong striations visible in Figure 15 are the result of seven intentional lamp pulses which were used to mark the growth interface. The pulses involved a 16% decrease in power which caused the growth rate to increase, thus increasing the effective distribution coefficient and the local Te concentration (see the SIMS section for further details on the effective distribution coefficient).

The structure of the ground-processed crystals was single crystal during the initial growth with polycrystalline material surfacing toward the tail end in two of the samples. Well-

defined growth striations were also observed on the tellurium-doped ground-processed samples (Figures 18 and 19). These were classified as strictly rotational type and, unlike the microgravity processed crystals, they exhibited long range periodicity throughout the cross-section. No striations of any type were revealed by chemical etching on the earth-grown, undoped GaSb samples.

The initial growth interface shape was clearly demarcated in all samples. It was found to have a slightly convex curvature relative to the solid in both the microgravity- and ground-processed crystals. The curvature of the solid/liquid interface in the interior of the Te-doped regrown crystals was revealed by the striations in the sectioned rod. For the Te-doped microgravity sample, the interface curvature was easily observed by the lamp pulse striations in the crystal as shown in Figure 15.

In this sample, determination of the aspect ratios (zone height over diameter) for the molten zones yielded values ranging from 0.72 to 1.22. The initial convex interface was observed to be contained within the early stages of growth along the section where the melt exhibited a small zone height. The convex interface region in the initial molten zone had an aspect ratio of 0.72. The interface subsequently switched to concave in the sections that exhibited reductions in diameter with the concomitant increase in zone height. The aspect ratio of 1.22 coincided with the concave interface. In, between, a flat interface was obtained at a ratio of 1.0. The tilting of the interfaces in this sample relative to the growth axis was apparently caused by the asymmetrical position of the molten zone relative to the thermal axis of the mirror furnace. (The asymmetrical position will be discussed in more detail as it relates to the radial dopant variation).

A similar result was also reported by Hermann and Müller [95HER] on float-zoned GaAs crystals processed in a microgravity environment. Apparently, with small molten zone lengths (small h/d), the radiant heat input to the molten material controls the shape of the interface thereby producing convex curvatures toward the solid material. This is so because it is easier to melt the outside of the rod than to melt the core. On the other hand, heat loss from the molten zone becomes the controlling factor for longer molten zones (large h/d) and the interface attains a concave shape. In other words, the interface shape is controlled by the relative magnitude of heat absorption and dissipation in the molten zone.

<u>Etch Pit Density</u>

The density and distribution of line defects intersecting the surface of wafers sliced along the (100) plane were characterized by the Etch Pit Density (EPD) method [52HOR]. First a discussion of the qualities of the etch pits observed with the etch chemistry used for this study will follow. Typical etch pits produced on the GaSb (100) single crystals are shown in Figure 20 by Nomarski interference contrast (NIC) microscopy and in Figure 21 by scanning electron microscopy (SEM). The samples for these photographs were left in the selective etching solution for an extended period of time to exaggerate the pit size in order to more clearly see their structure. Note that there are two types of etch pits visible in each of the figures, a deep oval pit with a pointed central core or shallow oval pits with a smooth center. All etch pits are aligned along the <100> direction. Brown et al. [82BRO] has correlated both types of defects with contrast features in transmission X-ray topographs (XRT), although the type of defects which cause each type of defect was not studied. In Brown's study, there were

a few contrast features in the XRT topographs which did not correlate with the pits observed on the surface, which was attributed to dislocations contained within the bulk of the material.

Etching chemistries along with correlation of defect types of the associated etch pits has not been studied in great detail for the {100} surface of GaSb. However, etch pits with a pointed morphology are typically attributed to line defects such as threading or slip dislocations while those with a smooth morphology can be caused by inclusions and small dislocation loops [80MIL]. Dislocation loops are more probable in GaSb since the point defect levels during growth are high for this material as evidenced by the p-type carrier concentration of the material even when undoped. It is also possible for the morphologies of edge and screw dislocations to exhibit different etching characteristics [87SAN]. Regardless of the nature of the etch pits, the 1:1 correlation of the etch pits with XRT is further supports the proposition that all types of dislocations are revealed with the chemistry used.

Figures 22 and 23 give the average EPD along the length of the growth axis for all regrown crystals and Figure 24 shows a summary of the reduction trends observed in all LEMZ-processed crystals. As one can see, the EPD of the as-received crystals (first data point for each graph) is typically high with counts ranging from 83,000-138,000 cm^{-2}. Figure 25 shows a typical micrograph of the etch pits in an as-received section of the crystal. As growth progressed, all crystals exhibited, to varying degrees, a reduction in the dislocation density as a function of distance from the initial solid/liquid interface. This general reduction trend can be attributed to the low thermal gradients and the containerless growth of the LEMZ technique. The degree of reduction observed was not equivalent in all crystals and was seen to be a function of gravitational environment, crystal doping, and interface

curvature, but not a function of the growth rate. This will be discussed individually below. Note that sample the tail end of 59/3 is a special case and will be discussed later.

The microgravity-processed crystals exhibited larger reductions in dislocation density than those processed on ground. For example, the doped microgravity sample attained the lowest average dislocation density value of 4,300 cm^{-2}, a reduction of ~20 times the seed value. An example of the etch pits visible in the tail end of this sample is given in Figure 26. On the other hand, the earth grown crystals, although still following the same trend, only exhibit a fraction of the reduction observed in the regrown space samples. The lowest reduction compared to the seed obtained for an earth regrown sample was 1.3 for sample GaSb 53/1. This large difference can be possibly attributed to the reduced convective flows under microgravity leading to a more quiescent interface. The difference can also be attributed to different axial and/or radial temperature gradients due to reduced convection in the melt, encapsulant, and furnace atmosphere. Others have found a similar result for samples grown in space. Cröll et al. found a reduction factor of 8 in GaAs wafers regrown in microgravity using the floating-zone technique in the same furnace [96CRÖ].

In terms of the crystal doping, the Te-doped crystal processed in microgravity exhibited the largest improvement in dislocation density with the aforementioned reduction of ~20 times the original seed compared to 4 and 10 for the undoped crystals. Conversely, the doped ground-processed crystals only exhibited a 1.1 times reduction which is comparable to the undoped ground-processed samples. However, it is important to note that both the doped terrestrial samples became polycrystalline after some growth distance and the reported EPD values are shortly after the initial growth interface. Since the trend in all samples is a

reduction in EPD with distance grown, it can be argued that had equivalent lengths of single crystal material been obtained on all samples, the doped terrestrial crystals would have exhibited a larger reduction.

It has been recognized that doping semiconductor crystals with certain impurities reduces the density of dislocations during crystal growth from the melt [78SEK, 83FOR]. This has been rationalized in terms of a solution hardening concept wherein the Critical Resolved Shear Stress (CRSS) of the matrix is effectively raised, either through considerations of bond strength or via a volume strain effect [87SEK]. It is suggested that the increased CRSS reduces the dislocations generated by temperature gradients behind the growing interface [56BIL]. It was suggested that Te acted as an impurity hardening agent in Czochralski-grown crystal, but this was for higher doping levels [86SUN].

For the Te-doped microgravity sample shown in Figure 15, the dislocation density on the concave side of the interface was about twice that of the opposite side which was more planar. Moreover, the dislocations across the crystal were observed to be more homogeneously distributed for a planar interface. The effect of zone height and the resulting interface curvature on the dislocation density is seen to be consistent with the thermoelastic stress theory that predicts higher stresses for solid/liquid interfaces that deviate from a planar configuration [95HER].

If there is a variation from that of a planar interface shape, a slightly convex interface has been proposed to be a desirable growth parameter since it is expected to allow dislocations to grow out of the surface of the material [92ŠES]. In this study, it appears that the doping and gravity environment contributions to EPD reduction are dominant over the possible

benefits of growing crystals with a convex interface. For example, in both ground-based Te-doped samples, the interface was revealed to be convex over the length of the crystal by examining the striations in the rod (Figures 18 and 19). However, the dislocation density was reduced very little in both samples along this distance indicating other higher order factors.

It appears that interface shape might play a partial role in the dislocation density trend for the doped space-grown sample. In Figure 15, the initial interface is slightly convex, but this interface quickly switches to concave over a distance of ~8 mm. In this distance, the EPD count is seen to increase. After this the interface switched back to convex and the EPD count drops. As discussed above, it must be kept in mind that the gravity environment rather than the interface curvature is the dominant factor in the EPD reduction for this sample. In the study mentioned above by Cröll et al. [96CRÖ], this point is discussed. They observed that the EPD value decreased by the factor of 8 despite a concave interface throughout growth. It should be noted that this type of analysis was not able to be applied to the undoped crystals since striations were not revealed in these samples.

Finally, increasing the translation rate did not appear to have an appreciable effect on the dislocation density of the crystals, and no increase in etch pit density was observed when the ampoule translation rate was increased. In all cases, the calculated density of etch-pits simply followed the observed reduction trend with growth distance. Stable thermal gradients can be invoked to explain this behavior. Similar results were reported by Cröll et al. [96CRÖ] on microgravity float zoned crystals of GaAs processed at up to 120 mm/hr. However, Abbaschian et al. [96ABB] reported reductions in the etch pit density of InBi crystals as the translation speed was increased.

A surprising anomalous result occurred in sample GaSb 59/3 as seen by the EPD count with distance in Figure 23. Single crystalline material was obtained throughout the length of this sample including where the zone collapsed. Figure 27 shows a photograph of the etched crystal illuminated in a way such that the etch pits are highly visible. It is seen that toward the end of the growth and in the collapsed zone, the dislocation density drops to nearly zero. This is the result for a sessile drop experiment with a gradual cool-down as the power was reduced.

The dislocation density of gallium antimonide grown in space has been studied by others as well. Nishinaga et al. [97NIS] examined the EPD in GaSb grown by the gradient freeze technique and it was found by examining the surface of the material that nearly half of the space grown part was processed without contact with the ampoule wall [97NIS]. The etch-pit density tended toward zero in the space-grown part where the melt did not touch the ampoule wall, but it increased dramatically in the part where strong contact with the wall occurred. They attributed this to strain-free growth in the microgravity environment. It must be mentioned that the seed material for this regrowth had a low dislocation value of <500 cm^{-2}. Of course, the dislocation density reduction in this study could theoretically produce values approaching zero had the seed dislocation density been lower.
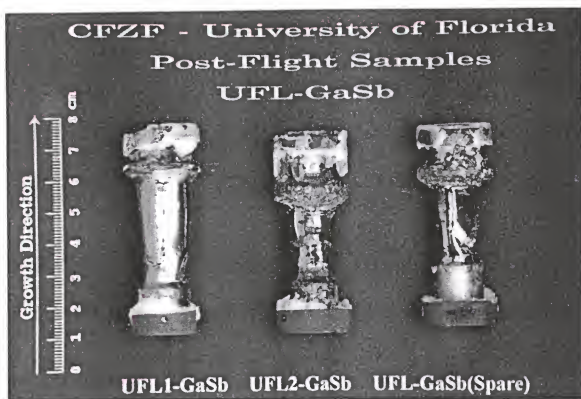
Figure 9 - Microgravity-processed GaSb crystal
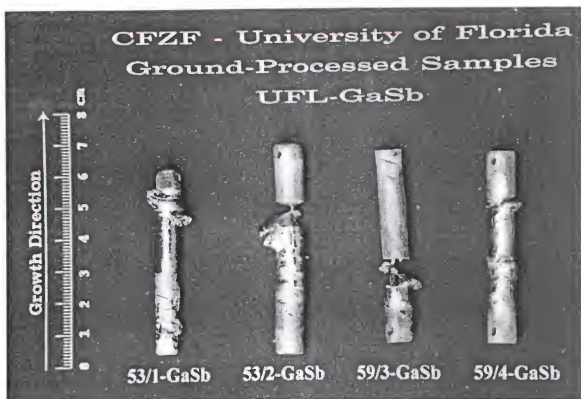
Figure 10 - Ground-processed GaSb crystals.
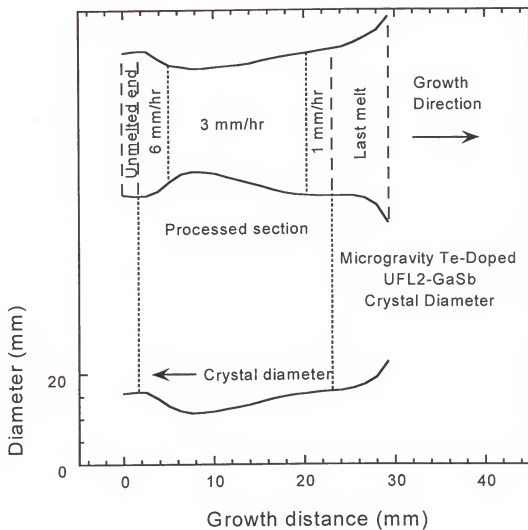
Figure 11 - Example diameter measurements for microgravity sample UFL2-GaSb.
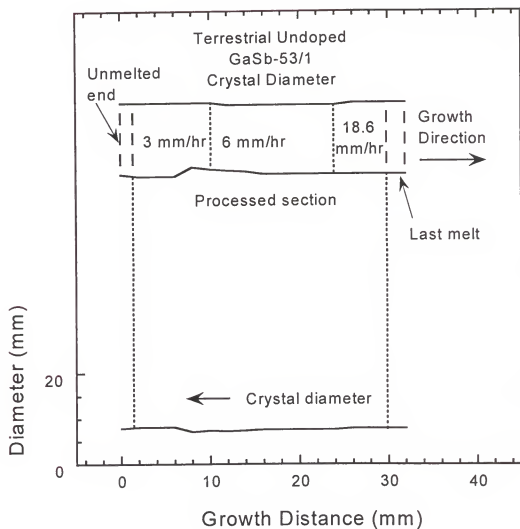
Figure 12 - Example diameter measurements for terrestrially-grown sample GaSb 53/1.

| Sample partially translated | Sample partially translated at minimum diameter | Post-growth |
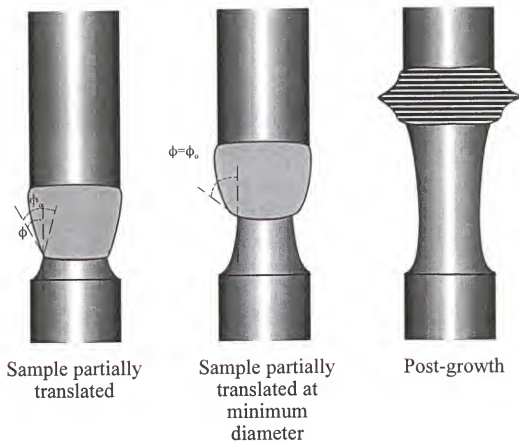
Figure 13 - Schematic showing the evolution of the molten zone shape (light grey area) and the regrown crystal diameter for the microgravity crystals. The excess material in the final zone creates a bulge in the final frozen section (horizontal lines).
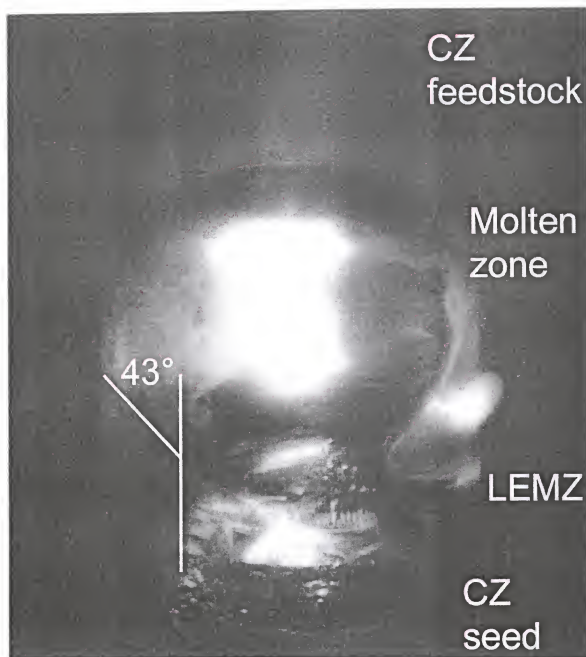
Figure 14 - Middle stages of microgravity processing showing a critical angle of 44°. (The angle measured on the right side was 45°.) Notice the reduction in crystal diameter as one moves up from the initial solid/liquid interface.
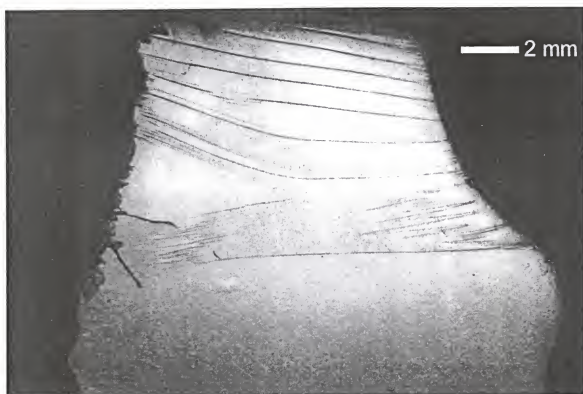
Figure 15 - Striation pattern observed on the internal structure of the seed portion of the Te-doped μg-grown crystal as revealed by chemical etching. The bottom of the figure is the original seed and the boundary indicates the initiation of the float-zoned material on the top.
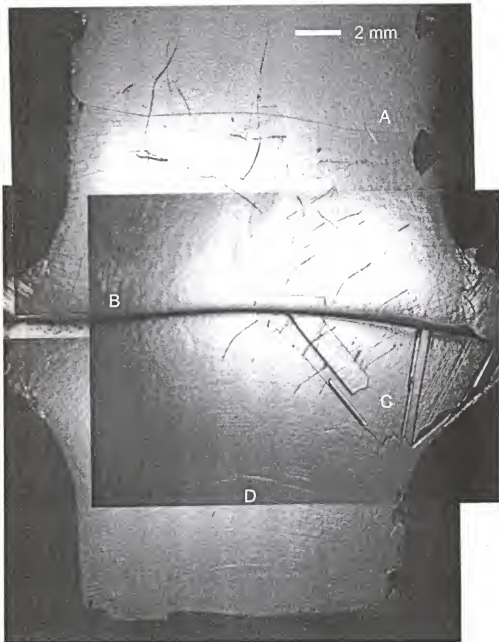
Figure 16 - Striation pattern observed on the internal structure of the tail section of the Te-doped µg-grown crystal as revealed by chemical etching. The translation direction of the molten zone was from bottom to top. The features of this photo include: A) the border between the as-received CZ-grown feedstock and the last molten zone, B) the section of the last molten zone where the top and bottom interface made contact and caused a portrusion, C) polycrystalline region in the last zone, and D) the approximate position in the crystal where growth was terminated by translation and switched to a gradient freeze as power was reduced.
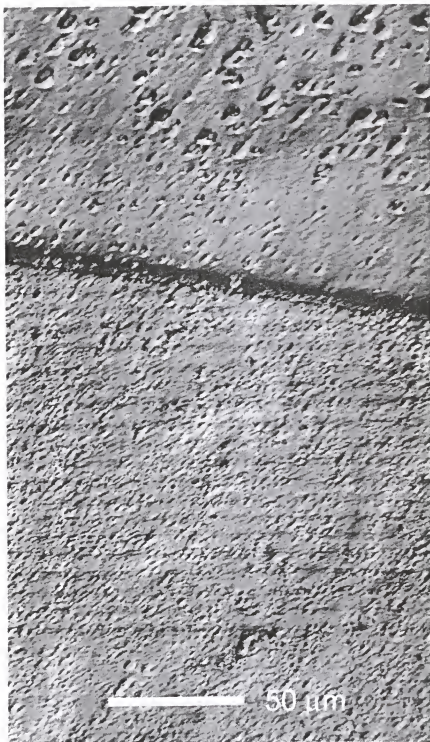
Figure 17 - Abrupt change in striation pattern at the LEMZ- and CZ-processed boundary (top and bottom of figure respectively) of the chemically etched Te-doped microgravity sample. Etch pits due to dislocations are also visible.
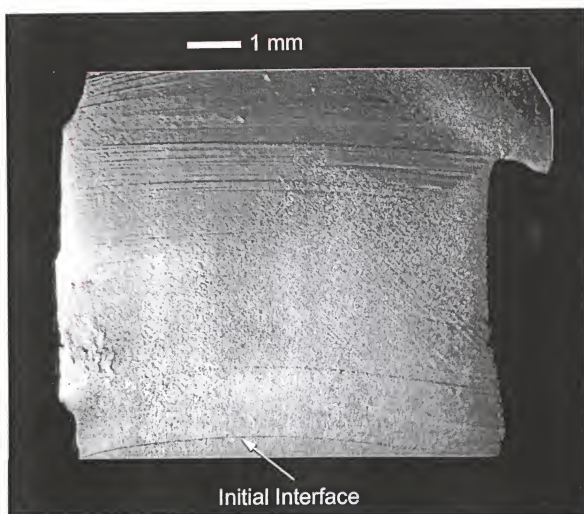
Figure 18 - Etched single crystal section from ground sample GaSb 59/3 cut along the growth axis showing growth striations and etch pits.

2 mm

Initial Interface
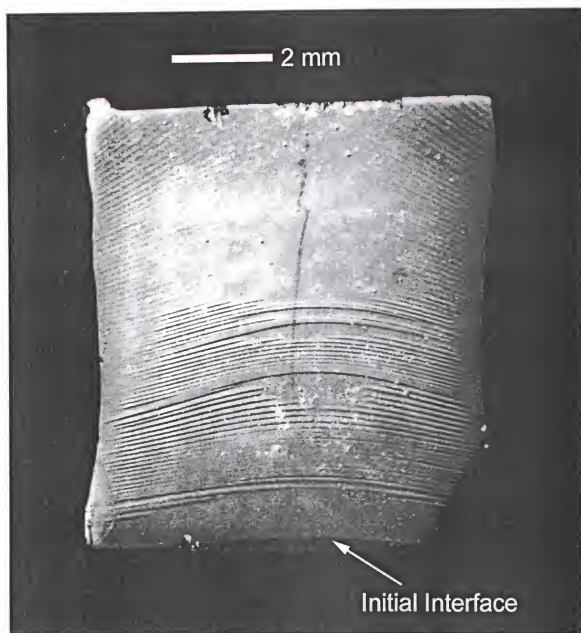
Figure 19 - Etched single crystal section from ground sample GaSb 59/3 cut along the growth axis showing growth striations.
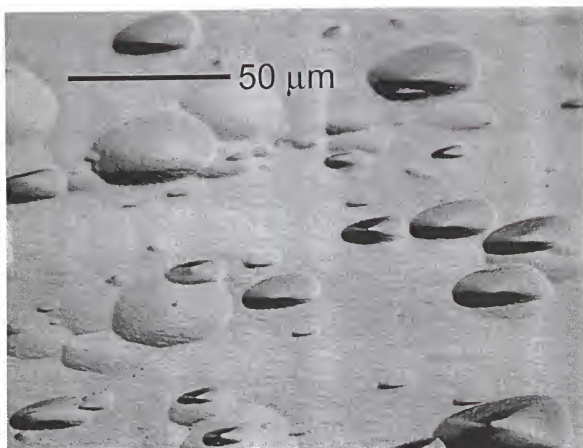
Figure 20 - Typical etch pits produced by selective etching on (100) GaSb as observed by NIC microscopy.
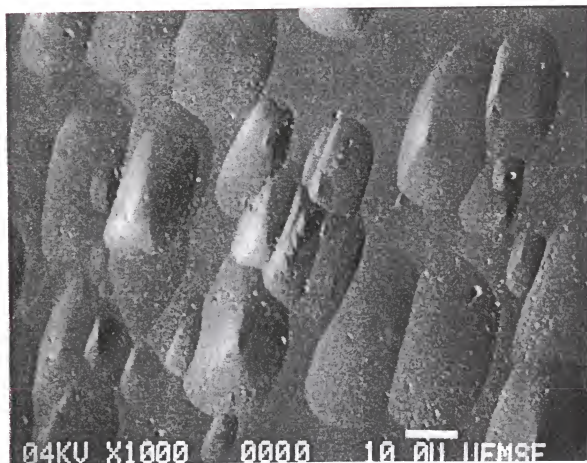
Figure 21 - Typical etch pits produced by selective etching on (100) GaSb as observed by scanning electron microscopy.
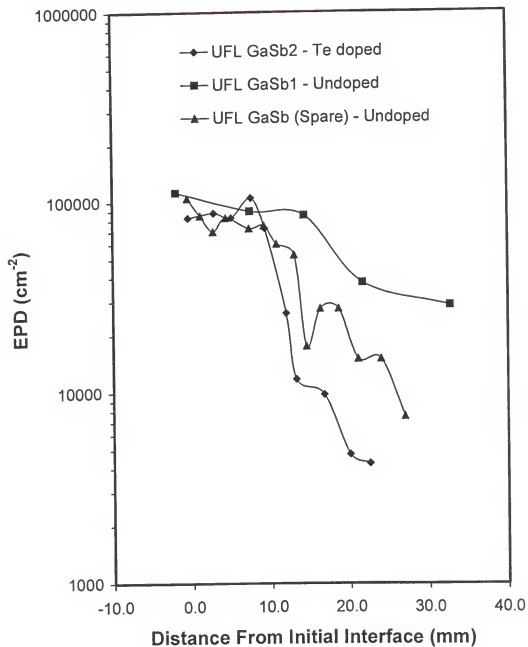
Figure 22 - Resulting average dislocation density along the growth axis for the microgravity samples.
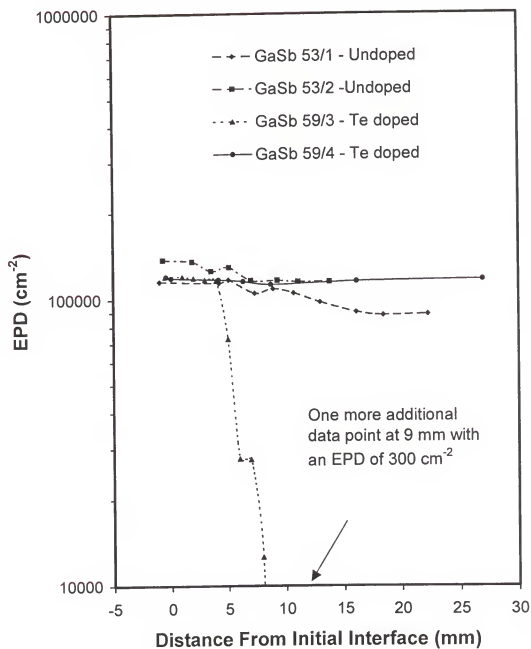
Figure 23 - Resulting average dislocation density along the growth axis for the terrestrial samples.
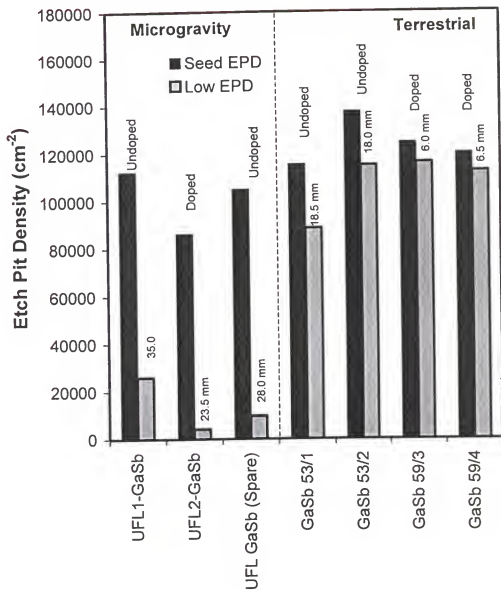
Figure 24 - Summary of the etch-pit densities observed on all LEMZ-processed crystals. The distance shown in the graph refers to the point at which the measurement was taken at the tail end of the single crystal.
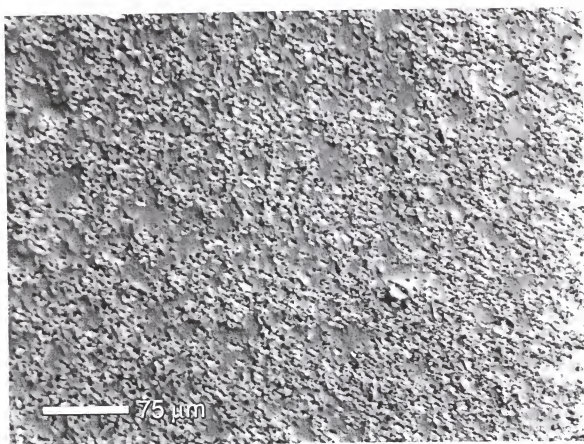
Figure 25 - Typical concentration of dislocations observed on the seeds of all crystals.
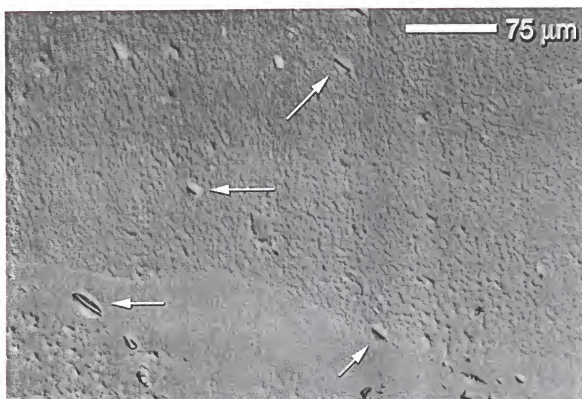
Figure 26 - Etch pits in the tail end of UFL2-GaSb. The more visible etch pits are marked with arrows. Note that the surface roughness visible in this sample is an artifact of the etching.
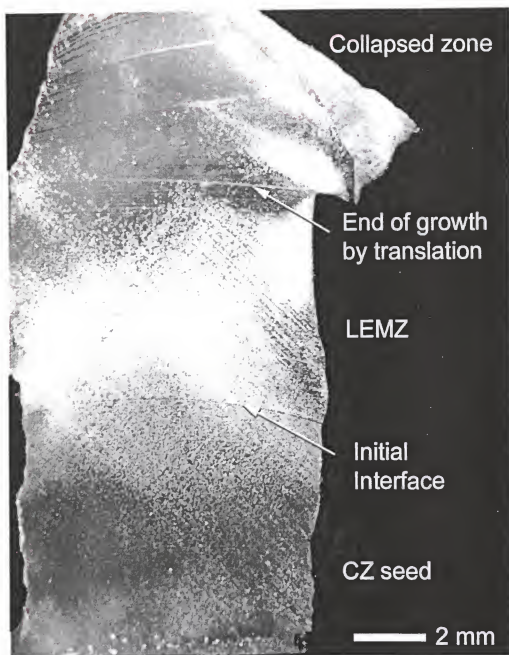
Figure 27 - Etched section of the ground sample GaSb 59/3 showing etch pits in the highlighted areas. The growth was interrupted by a collapsed zone. The etch pit density in this sample is for case of a sessile drop after with a reduction in power input.

SIMS RESULTS AND DISCUSSION

Macroscopic Segregation

Secondary Ion Mass Spectrometry (SIMS) was performed on the space-processed and one of the earth-processed tellurium-doped GaSb samples to determine the dopant distribution in the regrown crystal. Subsequent chemical etching was performed to reveal growth features and compare these with the SIMS results.

Segregation Phenomenon Background

Before discussing the specific results of this experiment, some background behind the driving force of macro- and microscopic segregation will follow. Assuming no impurity diffusion in the solid and full homogenization of the impurity in the liquid, the amount of the impurity incorporated in the crystal depends on its relative solubility in the solid, C_S, and the melt, C_L, by the equilibrium coefficient, $k_o = C_S/C_L$. For the majority of common solutes in semiconductors, including Te in GaSb, $k_o < 1$. Under finite growth rates, the concentration of the solute in the solid initially formed is $k_o C_L$, but with non-equilibrium growth, due to the combination of the inherent limited diffusion of the solute in the liquid and limited mixing of the melt due to weak convection, the concentration in the solid increases soon thereafter as the concentration in the liquid at the interface increases. Thus, an effective distribution

coefficient, k_{eff}, becomes $k_{eff} > k_o$, and continues to increase at a rate controlled by the rate of solute transport away from the interface into the bulk fluid by solution mixing due to convection and diffusion effects. This value is given by the following expression [53BUR]

$$k_{eff} = \frac{k_o}{k_o + (1 - k_o)\exp\left(-\frac{R\delta}{D_L}\right)} \qquad (7)$$

where R is the growth rate, δ is a parameter with units of length (sometimes taken as a boundary layer), and D is the diffusion coefficient. As determined by the variables in the exponential of equation, the actual value for k_{eff} varies between k_o and 1 depending on the growth conditions. The minimum value, which would set $k_{eff} = k_o$, occurs when $f\delta/D_L \ll 1$, that is, at slow growth rates, high liquid diffusivity, and maximum stirring to decrease the boundary layer (and visa-versa for $k_{eff} \rightarrow 1$). Under normal growth conditions where convection is present, but is not enough to homogenize the melt, δ will increase in value and k_{eff} will tend toward a moderate value that is between k_o and 1. The interaction between these variables is given in Figure 30. The diffusion coefficient of tellurium in liquid GaSb is 3×10^{-5} cm^2/sec as given by Müller [88MÜL]. The value of k_o=0.13 was used for the top four curves which, as will be seen below, is the effective distribution coefficient in the present samples. It is possible that the equilibrium distribution coefficient is lower than this value and the curve for k_o=0.01 is shown for the case of 1 mm/hr to illustrate the effect of a lower value. From the curves it is seen that increasing the boundary layer thickness has the effect of increasing k_{eff} toward one. An increasing growth rate has the effect of building up the dopant

concentration at the interface quicker than it can be diffused through the boundary layer. Thus, the boundary layer thickness decreases for equivalent values of k_{eff}.

Striations in the sample are caused by temperature fluctuations at the solid/liquid interface. If the driving force behind the float zone convection is increased, a point is reached at which the motion of the fluid becomes time periodic. Further increases in the convective driving force results in progressively more complex time dependence until the flow is turbulent. The time-dependent flow modulates both the crystal growth rate and boundary layer thickness. Both of these are terms in the expression for k_{eff} and locally changes the distribution of the impurity in the crystal, thus producing the solute striations.

Te-doped Microgravity Sample

Figure 28 is a photo of the successfully chemically etched UFL2-GaSb microgravity grown crystal near the seed end which, prior to SIMS analysis, was sliced perpendicular to the growth direction along the (110) plane. Similarly, Figure 29 is a photo of the tail portion of the same crystal, except it is the mirror face of the section from which the seed slice was taken. The etch features are highlighted with lines and points for clarity as they are difficult to discern in the macrographs. As illustrated for the seed sample, SIMS line scans were recorded twice along the growth direction in the center of the crystal and several SIMS depth profiles were performed in various locations across the crystal. For the tail section a single line scan was performed along the center of the crystal along with several SIMS depth profiles. (The depth profiles will be discussed in a following section.) As seen, there is a large drop in the Te concentration at the beginning of the regrown crystal followed by a slow

continuous macroscopic increase of the dopant concentration as the float zone was translated. This increase can be followed to the tail end of the crystal until the region where the translation stopped.

The major growth feature noted in Figure 28 is the boundary between the as received Czochralski (CZ) grown crystal and the regrown microgravity grown crystal at ~2.5 mm. Before this boundary, in the as-received CZ-grown seed section of the crystal, the SIMS line scan analysis shows an increase in the Te concentration that compares well with the measured room temperature carrier concentration values given later in the Hall measurement results. Typically the increase in dopant concentration for CZ-grown crystals follows the normal freeze equation given by [52PHA]

$$C(g) = k_{eff} C_o (1-g)^{k_{eff}-1} \tag{8}$$

where $C(g)$ is the concentration of solute (Te) in the solvent (GaSb) as a function of the fraction of original liquid volume (g), C_o is the initial solute concentration and k_{eff} is defined above. The variation of Te concentration in the seed section of the crystal increases, but not according to equation 8. The reason for this is not clear, but the processing of the as-received crystal is not pertinent and will not be discussed further.

The subsequent nearly order of magnitude drop in Te concentration at the initial growth interface indicates zone refining of the Te dopant. After this point, the influence of gravity upon the macroscopic redistribution of the impurity is introduced in the k_{eff} term by the parameter δ which can be thought of as a characteristic length of concentration profile. The

influence in the present experiment was determined by studying the details Te concentration profile with growth distance. Depending on the growth conditions imposed, two different equations can describe the macrosegregation of the Te dopant in the system. One assumes the melt is either partly or completely homogenized, usually due to convection in the melt leading to convective-controlled growth. The other assumes that convection is not present leading to diffusion-controlled growth. Recall from the Literature Review that the latter cases is desirable and has been achieved in a microgravity environment.

For the first case, one can assume mixing of the solute into the liquid (i.e. zero or limited solute build-up at the solid-liquid interface) due to either 1) full diffusion of the dopant with no convection or 2) convective mixing of the dopant caused by Marangoni convection in the case of space-growth. The first condition is rarely met as growth speed would be prohibitively slow. Under the second condition, the equation for redistribution of dopant describing a floating zone is given by [52PHA]:

$$\frac{C_S}{C_o} = 1 - \left(1 - k_{eff}\right)\exp\left(-\frac{k_{eff}x}{l}\right) \tag{9}$$

where l is the length of the molten zone and x is distance from the starting end.

In the other extreme, the solute distribution in the system is completely diffusion-controlled. Mass transport of the solute is controlled by diffusion only under controlled conditions where there is no convection in the melt, such as those conditions that can exist under microgravity where buoyancy driven convection is eliminated and Marangoni

convection is effectively controlled, thus allowing a high dopant concentration boundary layer to build up at the solid-liquid interface. The solute distribution can be described for low values of k_o by [53TIL]

$$\frac{C_S}{C_o} = 1 - (1 - k_o) \exp(-\beta x) \tag{10}$$

with

$$\beta = \frac{k_o \dfrac{R}{D}}{1 - \exp\left(-\dfrac{Rl}{D}\right)} \tag{11}$$

where all other terms are described above. If the boundary layer thickness is small compared to the zone length, the denominator for β tends toward unity. Note that equation 9 is of the same form as equation 10 with the only difference being the variables in the exponential. Schematics representations for each of the above extremes is given in Figure 31.

Directly determining whether equation 9 or 10 governs the macrosegregation of the Te dopant requires a knowledge of the convective fluid flow present in the melt. Unfortunately, this is not measurable directly for this system and must be determined either by modeling or performing experiments under controlled conditions to conform to either extreme. The following discussion will explore both possibilities and draw a conclusion based on the most likely interpretation.

In either of the above extremes, at $x=0$, $k_{eff}=C_s/C_o$ since a boundary layer has not built up at the beginning of growth. The drop in Te concentration measured at the initial solid/liquid interface calculates a k_{eff} of 0.13. According to both equations 9 and 10, the dopant concentration will subsequently increase toward the initial concentration, C_o. This is because either the zone (for equation 9) or the solid liquid freeze interface (for equation 10) is enriched and subsequently freezes out higher concentrations. As the zone progresses, enrichment continues, at a decreasing rate, until the concentration of Te in the liquid at the interface reaches C_o/k. From this point onwards, the solute concentration entering and leaving the zone are equal, and the concentration in the freezing solid remains C_o.

For the extreme of convection control with the above calculated value of 0.13 for k_{eff}, equation 9 will result in a relatively slow increase in Te concentration with the number of zone lengths translated. In fact the concentration of Te in the freezing solid would not even reach the value of C_o. During processing of UFL2-GaSb, the average zone length of 14.9 mm and zone translation of 20.8 mm results in only 1.39 zone lengths translated; therefore, at a k_{eff} of 0.13, the final concentration at the end of translation would only be expected to be $0.28 \cdot C_o$. The theoretical curve along with the SIMS data for both the seed and tail are shown in Figure 32. As seen, the measured Te concentration as revealed by SIMS analysis compares well with the theoretical curve.

For the other extreme, where the macrosegregation is diffusion controlled (equation 10), one needs to compare the theory to the SIMS data for various values of the growth rate, R. The variation in the growth rate of the solid/liquid interface was complicated in this sample and will be discussed first. Sample UFL2-GaSb initially grew at 6 mm/hr for the first 5.85

mm of translation. In reality, the zone height increased rapidly during the 6 mm/hr growth portion causing the initial interface to melt back slightly, thus creating a new initial interface (see [97ÓP] for details of the processing). After this point, the expansion of the zone height slowed compared to the translation and the solid/liquid interface did travel in a positive direction. However, due to the initial zone height increase, the 5.85 mm of translation of the ampoule in the furnace was not the same as the distance that interface traveled during this growth stage. This was determined by examining the striations caused by the planned lamp power reductions in the experiment. As highlighted in the SIMS results, the strong striations visible in Figure 28 have a direct correlation with the pulses which locally increased k_{eff} and thus, increased the Te concentration until the melt system corrected back to steady state conditions. The first strong striation visible in Figure 28 corresponds to the transition from 6 mm/hr to 3 mm/hr. As seen, this transition actually occurs at 2.5 mm from the melted back interface instead of the 5.85 mm that was translated. After this point, even though the ampoule translation velocity was reduced to 3 mm/hr, the calculated growth velocity of the interface, based in the lamp pulse striations, varied between 7.4 and 3 mm/hr from start to finish. This is consistent with the observed reduction in zone height in this region back to the initial height at the beginning of growth. This increased the solid/liquid interface velocity to values higher than that of the ampoule translation velocity.

Regardless of the real translation velocity of the solid/liquid interface, the extremes of 3 and 7.4 mm/hr were used in equation 10 and the resulting theoretical variation in impurity concentration, along with the measured SIMS data are plotted in Figure 32. Compare the diffusion-controlled theoretical curves to that of the convective-controlled theoretical curve

and it is evident that convective controlled growth most likely dominated, even in space, owing to Marangoni convection. However, the convection appears much more controlled and less turbulent than in the as-received Czochralski-grown section where there are numerous striations due to microsegregation as was reported earlier in Figure 17.

A comment should be made concerning the effect of the growth rate on the dopant distribution. As seen above for the diffusive controlled case, the growth rate has a profound effect upon the distribution of the solute with growth distance. Even for the case of convective controlled growth, the growth rate can change the solute distribution through a variation in the value of k_{eff}. However, recall from Figure 30 that k_{eff} can remain at values near k_o over a large range of values for the boundary layer thickness. From the excellent fit between the SIMS data and the equation for convective controlled growth (over a range of growth rates), the value of 0.13 calculated above is considered to be the equilibrium distribution coefficient. Only the boundary layer thickness is expected to change with the changes in growth rate in this experiment.

After the end of translation in the doped space sample, the Te concentration in the last melt steadily increases, as expected, due to the increasing solute concentration as the zone freezes from both interfaces and becomes smaller. The peak in the graph reflects the last melt interface of the crystal as the two freezing faces made contact.

Earth-Grown Sample

The analysis of the marcrosegregation in the earth-grown samples was treated in a similar fashion to the undoped crystals. The SIMS measurements for this sample are given in Figure

33. Unlike the other seed and tail sections of sample UFL2-GaSb above, the line scan was performed in a radial direction. Depth profiles were also performed on the samples in various locations across the crystal. The macrosegregation for this sample was determined by looking at the Te concentration in the data points along the center of the sample along with the Te concentration in the line scan at this location. These concentrations are plotted in Figure 34. To fit the data, convective-controlled growth was assumed for this sample as is the case for terrestrially-grown crystals. First, the Te concentration in the as-received crystal was estimated to be around 3.27×10^{18} cm^{-3} based on the carrier concentration of 1.4×10^{18} cm^{-3} given by the supplier. (As will be discussed in detail in the variable temperature Hall measurements section, the measured carrier concentration at room temperature is always lower than the impurity concentration due to the special band structure of the GaSb crystal, the compensation caused by the native acceptors and the partial self-compensation from the Te donors.) A least squares fit to the first four data points in the curve resulted in a effective distribution coefficient of 0.125, a value that matches extremely well with the calculated value of 0.13 for the microgravity samples.

Depth Profiles and Radial Segregation

As mentioned, SIMS depth profiles were performed at several points on all samples. Figure 35 and 36 show schematics of the seed and tail crystals in the microgravity sample showing the Te concentration per cubic centimeter in the depth profiles. Note that, for SIMS measurement purposes the tail sample was reduced from its original size and the shaded area is the crystal observed in Figure 29. As was the result for the sections in Figures 28 and 29,

the depth profiles follow the same general trend of the line scan, that is, a high dopant concentration in the as-received section followed by a sharp drop due to zone-refining. Moreover, the Te concentration is seen to increase slowly with increasing distance from the initial growth interface as predicted.

A slight variation in concentration is seen in the radial direction and an attempt to observe a trend in this data and relate it to processing conditions is as follows. The first task that was performed was to replot the data along the lines of a constant interface. That is, as seen in the previous chapter, the interface shifted in direction and/or amount of curvature depending on such factors as the zone height and the distance between the zone and the graphite rings at the end of the sample. Thus, a certain distance on one side of the sample does not correlate with the same solid liquid interface on the other side or the center of the sample. This concept is illustrated in Figure 37 for the seed section of the microgravity crystal. For consistency, the depth profile data points were traced back to the position were they best matched "Line Scan 1" in the figure. The position of this point in the line scan from the initial interface was used in the graph for the independent variable.

The next step is to compare the concentration of the dopant in the radial direction at any given distance (i.e. to evaluate the relative locations of the curves in the figures). In general there appears to be no pattern in the radial distribution of the dopant. An argon free cavity bubble was intentionally placed in the ampoule to account for the volume expansion of the salt upon melting. Unfortunately, this was located near one side of the melt zone at all times in the microgravity sample since it was not buoyant in the space environment. The large triangular shape in the schematic is the direct result of this bubble shifting from the bottom

side of the crystal to the top side (in the schematic). This caused a rapid growth in the crystal in this region causing a higher measured Te concentration according to the equation for k_{eff}. Also, data points which were located in the striations caused by the lamp pules were in general found to have a higher Te concentration in comparison to the data points which were outside of the striation region, similar to the results of the line scan given above.

The tail section of the sample was analyzed in a similar fashion. As in the seed sample, the data was also replotted to conform to a constant location along the line scan. The result is given in Figure 38 without a schematic of the crystal. Again, no general pattern can be found in this sample which can be related to the processing conditions. In fact, it is interesting to see that for Line 1, Line 2 and the Line Scan, the Te concentration increases; however, Line 3 sharply decreases and then increases again in Line 4.

The reason for this variation over such a short distance is not known at this point, but must be a factor of the convection present locally at that point in the rod as the crystal was grown. It is supposed that the convection in the crystal is far from an idealized case since the argon bubble physically pushed the rod and the molten zone until it actually hit the quartz ampoule. During ampoule fabrication, great care was taken to place the crystal in the center of the ampoule. Moreover, the ampoule was initially centered in the ampoule holder to an eccentricity tolerance of ± 0.25 mm. The bubble moving the sample off axis by several millimeters had the effect of causing highly irregular thermal gradients in the crystal since the focus of the halogen lamp varies greatly with radial distance. This would cause local variations in the flow pattern at the solid/liquid interface. An inflow to the solid liquid interfaces would compress the thermal boundary layer thickness (δ_T). The diffusion boundary

layer thickness, given by δ layer in equation 7 is proportional to δ_T; thus, as seen in this equation, a large inflow would reduce δ resulting in a decrease in k_{eff} and the amount of solute incorporated into the crystal [88MÜL].

The earth grown section had a line scan performed in the radial direction as shown earlier in Figure 33. Also, depth profiles in this sample were also analyzed for radial differences in dopant distribution in a similar fashion to the seed and tail sections of the Te-doped microgravity sample. The results for this analysis are given in Figures 39 and 40. As seen, the radial distribution is even around the center of the sample and drops off toward the edges of the crystal. A similar trend is visible in the depth profiles as visible in Figure 33. This would indicate that the flow pattern in this crystal is more homogenous across the crystal interface with increased convection toward the interface near the edges of the crystal. Thus, the boundary layer thickness was decreased locally decreasing k_{eff}.
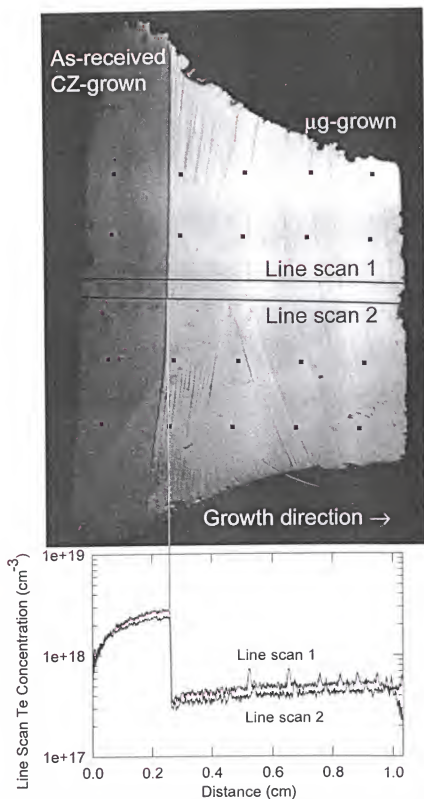
Figure 28 - Chemically etched seed section of UFL2-GaSb showing SIMS line scans and several depth profiles (small squares). The Te concentration in the line scans is shown to compare with the etch features.
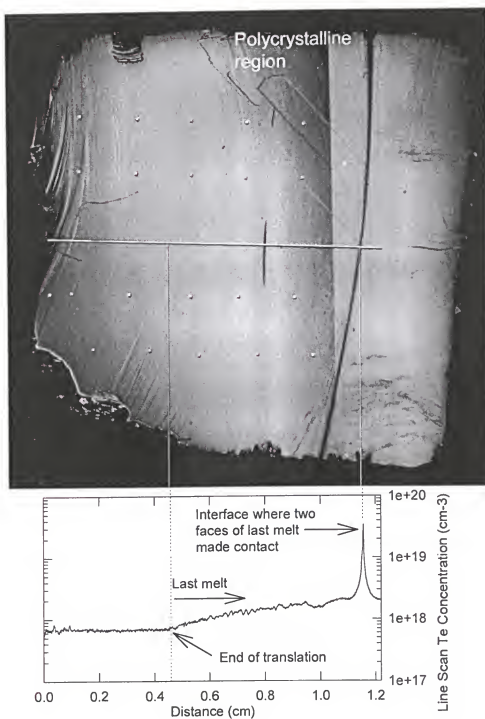
Figure 29 - Chemically etched tail section of UFL2-GaSb showing as SIMS line scan down the center of the crystal and several depth profiles (small squares). The Te concentration of the line scan is also shown to compare with the etch features. The growth direction is from left to right.
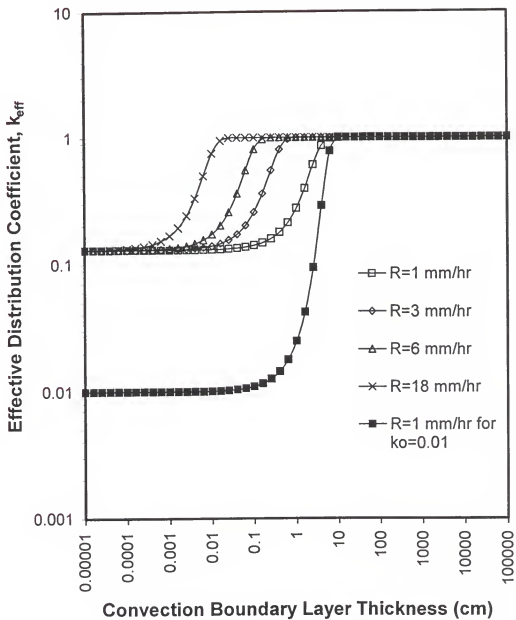
Figure 30 - Plot showing the relations between the variables for the effective distribution coefficient equation.
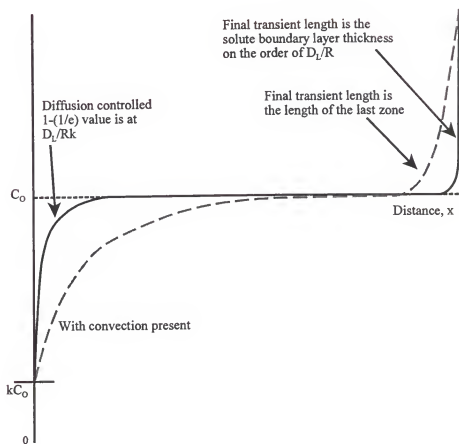
Figure 31 - Schematic diagram showing the impurity concentration profiles with the floating-zone growth method under the extremes of diffusion-controlled growth and convective-controlled growth.
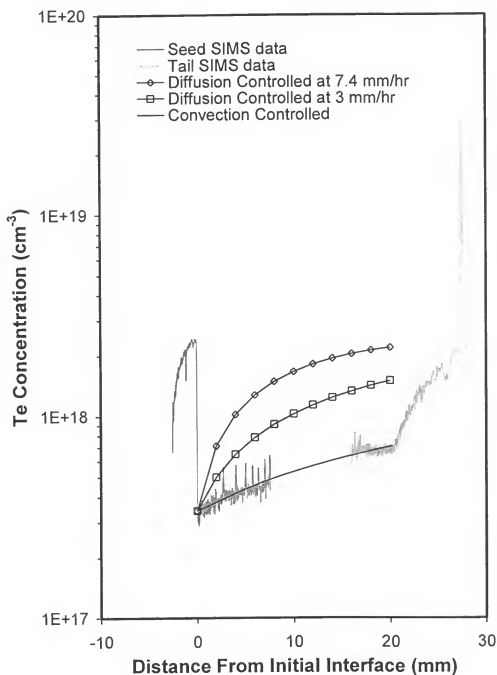
Figure 32 - SIMS data from the seed and tail sections of UFL2-GaSb put together with the theoretical curves for diffusive- and convective-controlled growth.
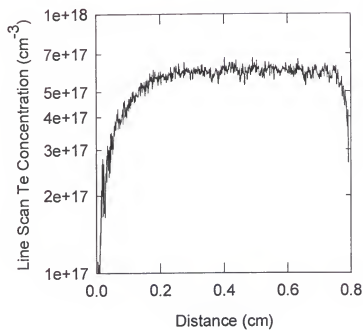
Figure 33 - Chemically etched seed section of GaSb 59/3 showing a radial line scan and several depth profiles. The Te concentration in the line scan is shown to compare with the etch features.
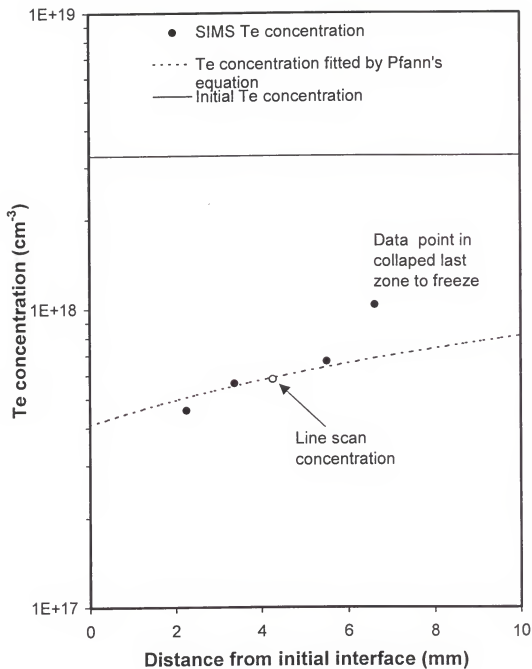
Figure 34 - Plot of SIMS data points along the growth direction fitted by Pfann's equation assuming convective-controlled growth.
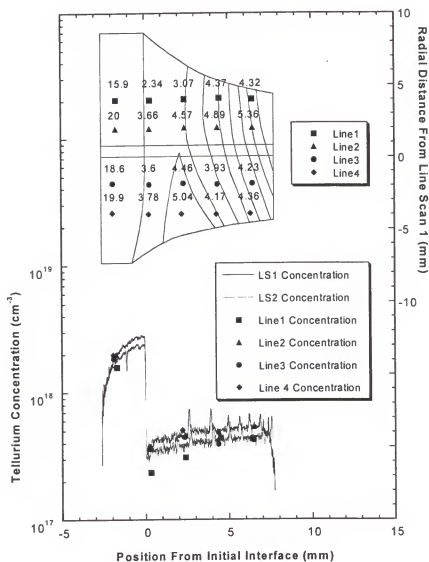
Figure 35 - Schematic of the seed section of UFL2-GaSb simultaneously showing the SIMS line scan data and the depth profiles. The concentration in the schematic is ×10^{17}.
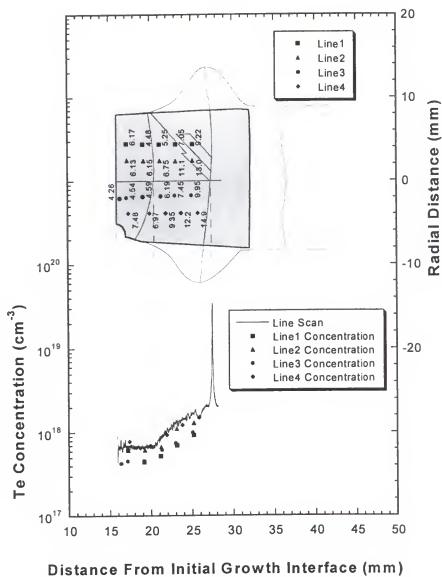
Figure 36 - Schematic of the tail section of UFL2-GaSb simultaneously showing the SIMS line scan data and the depth profiles. The shaded area was cut from the rest of the crystal for mounting purposes and is the same section visible in Figure 29.
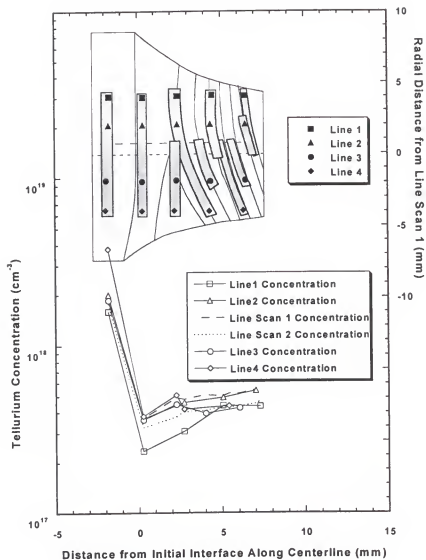
Figure 37 - Depth profiles in the seed section of UFL2-GaSb replotted to conform to a constant solid/liquid growth interface.
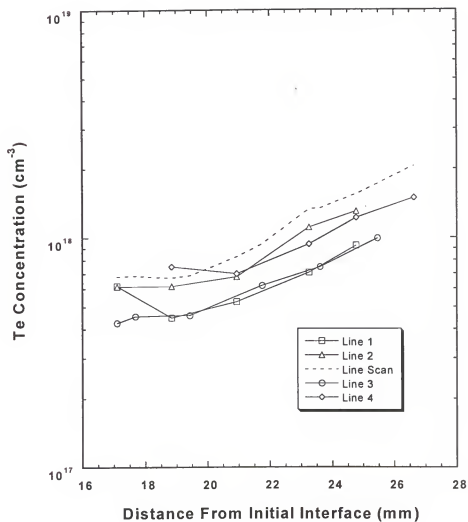
Figure 38 - Depth profiles in the tail section of UFL2-GaSb replotted to conform to a constant solid/liquid growth interface.
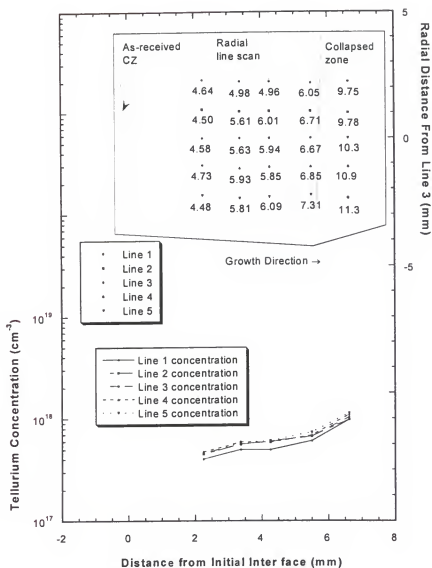
Figure 39 - Schematic of ground sample GaSb 59/3 showing the SIMS depth profiles and the Te concentration in the radial line scan at the same radial distance as the points.
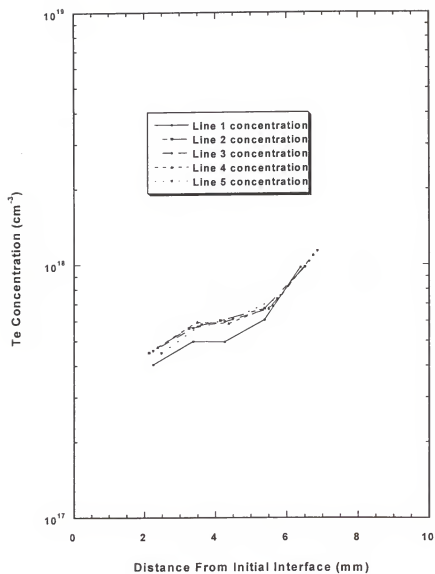
Figure 40 - Depth profiles in the seed section of UFL2-GaSb replotted to conform to a constant solid/liquid growth interface.

HALL MEASUREMENT RESULTS AND DISCUSSION

Variable Temperature

p-type GaSb

Three undoped nominally p-type samples were tested with Hall measurements at variable temperatures ranging from 30 °K to room temperature. Namely, the three samples were a sample regrown under microgravity conditions (UFL GaSb Spare Wafer A), a sample regrown on earth at 1 g and the unprocessed, as-received tail end of the space sample grown by the Czochralski technique also under 1 g (UFL GaSb Spare Tail Slice). Figure 41 shows the plot of the temperature dependence of the Hall coefficient.

In order to evaluate the thermal activation energy of the acceptor level, the electroneutrality equation has to be solved. For an undoped sample with two acceptors and an unintentional compensating donor, this is [64EFF]

$$p = \frac{N_{A1}}{1 + g \cdot \exp\left(\dfrac{E_{A1} - E_F}{kT}\right)} + \frac{N_{A2}}{1 + g \cdot \exp\left(\dfrac{E_{A2} - E_F}{kT}\right)} - N_D \tag{12}$$

where k is the Boltzmann constant, T is the temperature, p is the concentration of free holes in the valance band, N_{A1} and N_{A2} are the concentrations of the two acceptor levels with energy levels E_{A1} and E_{A2}, and N_D is the concentration of the compensating donors.

Attempts have been made to analyze the variable Hall temperature data of GaSb samples with a one-acceptor approach also. In general, this has been found to be deficient in describing the results; however, this analysis will be performed in the present case for completeness. For one acceptor level, the electroneutrality equation is given by

$$p = \frac{N_{A1}}{1 + g \cdot \exp\left(\dfrac{E_{A1} - E_F}{kT}\right)} - N_{D}.$$

(13)

The total concentration of holes is also calculated by integrating the Fermi-Dirac distribution function $F_{\frac{1}{2}}$

$$p = N_V F_{\frac{1}{2}}\left(\frac{E_F}{kT}\right).$$

(14)

The effective valence-band density of states, N_V is given by

$$N_V = 2\left(\frac{m_{hh,lh} k_B T}{2\pi \hbar^2}\right)^{3/2},$$

(15)

where $m_{hh,lh}$ is the effective mass of the heavy and light holes and $\hbar$ is the Planck constant. In the case of non-degenerate statistics (i.e. $E_{A1} < 3kT$), the Boltzmann approximation is valid and equation 14 is given by

$$p = N_V \exp\left(-\frac{E_F}{kT}\right).$$

(16)

Substitution of equation 16 into equations 12 gives

$$N_V \exp\left(-\frac{E_F}{kT}\right) = \frac{N_{A1}}{1+g\cdot\exp\left(\frac{E_{A1}-E_F}{kT}\right)} + \frac{N_{A2}}{1+g\cdot\exp\left(\frac{E_{A2}-E_F}{kT}\right)} - N_D \qquad (17)$$

which one can solve for E_F via iterative techniques. Subsequently, p can be solved for in equation 16. Alternatively, for the one acceptor case it is easier to solve equation 16 for E_F and substitute this into equation 13, thus obtaining

$$p = \frac{N_{A1}}{1+g\cdot\exp\left(\frac{E_{A1}}{kT}\right)\frac{p}{N_V}} - N_D \qquad (18)$$

These formulas were used to study the ionization energy(ies) and concentration(s) of the acceptor level(s) via a least-square fit of the experimental data.

For the case of a one acceptor approach, equation 18 can be solved for p. The equation is in the form of a quadratic equation whose solutions is the positive root to

$$g\exp\left(\frac{E_{A1}}{kT}\right)p^2 + \left[N_V + gN_D\exp\left(\frac{E_{A1}}{kT}\right)\right]p - \left(N_{A1}N_V + N_D N_V\right) = 0 \qquad (19)$$

and the solution to this is given by

$$p = 2(N_A - N_D)\left[1 + g\frac{N_D}{N_V}\exp\left(\frac{E_A}{kT}\right) + \left(\left(1 + g\frac{N_D}{N_V}\exp\left(\frac{E_A}{kT}\right)\right)^2 + \frac{4(N_A - N_D)}{N_V}g\exp\left(\frac{E_A}{kT}\right)\right)^{1/2}\right]^{-1} \qquad (20)$$

From this, it is customary to plot $\log(p)$ vs. $1/T$, which in general is not linear. Two limiting cases where the curve becomes linear can be used to determine the acceptor energy. At low temperatures, a straight-line fit to the $\ln(p/T^{3/2})$ vs. $1/T$ plot may be realized by the following equation if $p \ll N_D$ and $p \ll N_A$-N_D

$$p \propto T^{3/2} \exp\left(-\frac{E_A}{kT}\right). \tag{21}$$

Under this case, the slope is equal to $-E_A/k$. At more intermediate temperatures, a straight line fit to the $\ln(p/T^{3/4})$ vs. $1/T$ plot may also be followed under the following equation if $p \gg N_D$ while the condition $p \ll N_A$-N_D remains

$$p \propto T^{3/4} \exp\left(-\frac{E_A}{2kT}\right). \tag{22}$$

Here, the slope is equal to $-E_A/2k$. If the material is compensated with donors, then $N_D \gg p$ is always true and the intermediate temperature range will not be realized. In this case equation 21 will be true at both intermediate and low temperatures. The plots of these two curves are shown in Figures 42 and 43 and the resulting E_A calculations are given in Table 6; the calculated values are given for the last two data points in the low temperature region. The significance of the results will be discussed in the following discussion together with the results of the more general solution.

Table 6 - Calculated ionization energies assuming a straight line fit.

Sample	E_A for $\ln(p/T^{3/2})$ vs. $(1/T)$	E_A for $\ln(p/T^{3/4})$ vs. $(1/T)$
UFL GaSb Spare Tail (as recieved)	8.76	22.94
UFL GaSb Spare Wafer A (μg processed)	8.99	23.31
UFL GaSb 53/1 Wafer 5 (earth processed)	3.50	12.65

The more general solution of equation 20, which does not follow the assumptions of the straight line fits, was also analyzed for comparison. There is uncertainty in the values for the heavy and light hole masses in the literature. Values range from $0.28m_e$ and $0.05m_e$ to $0.5m_e$ and $0.07m_e$ for the heavy and light hole masses respectively. From equation 15, this results in a range of values for N_v from $7.93 \times 10^{14} - 1.80 \times 10^{15} T^{3/2}$. For both extremes, the values of E_{Al}, N_{Al}, and N_D were varied to obtain the best least-square fit to the experimental data. The program that performed the fit for the one acceptor level case was the commercial plotting program KaleidaGraph. Figures 44 and 45 show the results of this fit for the case of one acceptor level. The numerical results to the fits are given in Table 7. Note that in general, two unique solutions to the best fit are presented. This is the result of two local minima that are possible using this approach. The results illustrate the need to analyze the least square fit data carefully even with a simple model such as this with one acceptor level.

From the above tables, it is obvious that there are two solutions to the variable temperature data; one for a highly compensated sample with a lower acceptor energy level and one for an uncompensated sample with a higher acceptor energy level. Some fits were

Table 7 - One level curve fit results for p-type samples.

	Curve fit 1 - high compensation			Curve fit 2 - low compensation		
$N_v = 7.93 \times 10^{14} T^{3/2}$	N_{A1} ($\times 10^{17}$)	E_{A1} (meV)	N_D ($\times 10^{17}$)	N_{A1} ($\times 10^{17}$)	E_{A1} (meV)	N_D
UFL GaSb Spare Tail (as recieved)	-	-	-	4.66	12.4	0.4
UFL GaSb Spare Wafer A (μg processed)	6.57	9.60	4.62	1.59	27.8	-4.1×10^{14}
UFL GaSb 53/1 Wafer 5 (earth processed)	4.13	4.52	2.30	1.50	16.57	-2.9×10^{15}
$N_v = 1.81 \times 10^{15} T^{3/2}$						
UFL GaSb Spare Tail (as recieved)	5.63	9.84	2.12	3.38	18.31	5.4×10^{15}
UFL GaSb Spare Wafer A (μg processed)	4.22	9.85	2.05	1.96	23.93	2.1×10^{13}
UFL GaSb 53/1 Wafer 5 (earth processed)	7.38	4.17	5.65	1.28	21.01	-4.5×10^{15}

only possible if a negative value for the donor concentration was used (which is, of course, impossible). The solutions for the highly compensated case are difficult to accept since donor concentrations should not be present in the $> 10^{17}$ range. For the lower compensated solution, a negative value for the donor concentration for the earth processed sample in *both* solutions can be considered as a non-solution.

From the above sets of data, it is obvious that a one level acceptor approach is inadequate in solving for the best curve fit. A better fit to the Hall data was performed by a two-level fit following equation 17. As will be seen in the section describing the photoluminescence

results, acceptor levels are found in the above samples at 12.5 and 33.0 meV. These energy levels were used to fit the variable temperature Hall measurements. The variables in this case will be the acceptor concentrations at the two levels and the number of compensating donors. An solution for p in this case (similar to the quadratic in equation 20) is the solution to a cubic and too cumbersome to solve for analytically. Therefore an iterative solution was used to solve for the Fermi level (in Mathcad) and thus the carrier concentration was found with equation 16. The effective masses of the light and heavy holes was chosen to be $0.045m_e$ and $0.36m_e$ as used by Meinardi et al. [93MEI]. This value is intermediate between the two extreme values given above and gives the best fit to all three sets of data. The results of the analysis are shown in Figure 46 and listed in Table 8.

Table 8 - Two acceptor level and donor level concentrations for 12.5 and 31 meV acceptor levels.

Samples	$N_{a,12.5}$	$N_{a,33.0}$	N_d
UFL GaSb Spare Tail (as recieved)	3.5×10^{17}	1×10^{17}	3.9×10^{16}
UFL GaSb Spare Wafer A (μg processed)	9×10^{16}	1.4×10^{17}	2.8×10^{16}
UFL GaSb 53/1 Wafer 5 (earth processed)	9×10^{16}	8×10^{16}	3.2×10^{15}

The results given are much more numerically reasonable than for the one acceptor case; therefore it can be concluded that the acceptor level observed at 12.5 meV is real and needs to be taken into account in the present samples. Other authors have also found an acceptor

level around this energy level in variable temperature Hall measurements using a two acceptor level approach; 11 meV [64EFF], 12.3 meV [88JOH], 15.3 meV [93MEI], and 12 meV [94BAR,95BOS]. Note that authors who have used a single acceptor approach have found values higher energy values for the acceptor level; 19 and 24 meV [73DOL], 17.6 meV [93MEI], and 25.1 and 26.4 meV [81NAK]. These results are similar in number to this studies lower compensated column in Table 7 (Curve fit 2). It is believed that had the latter samples been analyzed by a two acceptor approach, a more accurate representation of the sample acceptor levels would have been realized.

The variation of Hall mobility with temperature for the three samples is shown in Figure 47. The highest values are observed in the two regrown samples, but this should be taken as normal sample variation. (In fact, as will be seen in the room temperature results, the highest observed mobility in the undoped samples is an as-received CZ-grown seed section.) Typical of most semiconductors in the higher temperature ranges, the mobility decreases with increasing temperature as the free carriers increasingly interact with the lattice phonons. Dutta [96DUT] has calculated that nonpolar and polar optical phonons and acoustic scatterings all make significant contributions for the undoped sample. The mobility approaches the $T^{-3/2}$ theoretical lattice scattering law as the temperature is raised. In the low temperature range, the mobility begins to level in the two regrown samples (UFL GaSb, Spare, Wafer A and UFL GaSb 53/1 #5) indicating the onset of ionized impurity scattering.

n-type GaSb

The variable temperature Hall data for the n-type samples was analyzed using Sagars's two-band model combined with a single Te donor level resonant with the subsidiary band. The details of the fit are as follows. First, a value was assumed for the tellurium concentration, N_D, the energy of the L-band above the Γ-band, ΔE, and the change in level of this energy with temperature, $d(\Delta E)/dT$. From this, the Fermi level at each temperature was determined using the charge balance equation, thus giving the variation with temperature of the concentration of carriers in each of the bands. The charge balance equation applied to n-type gallium antimonide is given by

$$n_\Gamma + n_L + n_i = N_D - 2N_A - N_{Te} \tag{23}$$

where N_A is the concentration of native compensating acceptors, N_{Te} is the concentration of acceptors created simultaneously by the tellurium donors which acts to self-compensate the material, n_i is the concentration of the carriers frozen into the impurity level associated with the L minimum given by

$$n_i = \frac{N_D}{1 + \dfrac{1}{g_L} \exp\left(-\dfrac{E_f - \Delta E + E_D}{k_B T} \right)} \tag{24}$$

and the concentration of carriers in the Γ and L bands is given by

$$n_\Gamma = N_{c\Gamma} \mathscr{F}_{1/2}\left(\frac{E_F}{kT} \right) \tag{25}$$

and

$$n_L = N_{cL} \mathscr{F}_{\frac{1}{2}} \left(\frac{E_F - \Delta E}{kT} \right).$$
(26)

Here, g_L is the degeneracy factor of the impurity band at ionization energy E_D below the L-band edge, $N_{c\Gamma}$ and N_{cL} are the effective density of conduction band states, and $\mathscr{F}_{\frac{1}{2}}$ is the Fermi-Dirac function of order ½.

The value for the degeneracy factor was taken as two [76HOO]. The concentration of native compensating acceptors was taken to be 1×10^{17} and the factor of two in front of the term in the charge neutrality equation is to take into account the double acceptor nature of the native defect. Based on previous research [96DUT], the concentration of tellurium acceptors was also given the value of 1×10^{17}. The concentration of ionized donors was taken to be the full value in the charge neutrality equation because the donor band below the central valley merges with the conduction band [97DUT]. The value of E_D in the literature varies between 4 and 33 meV based on the measuring method used and the concentration of tellurium. A reduction in the ionization energy is common in heavily doped materials due to broadening of the impurity levels into a band and band tailing in the L-band minimum. For the present experiment, a value of 13.8 meV was taken as the ionization energy at low doping levels and this was reduced to 4 meV for the higher doping levels [74SUN]. The value for $N_{c\Gamma}$ was calculated in a similar manner as N_V in equation 15 with a value of $0.047 \cdot m_0$ used for the effective mass of the electrons in this band. The energy bands were assumed to be

parabolic and the value of N_{cL} was taken to be $40 \cdot N_{c\Gamma}$. The Fermi-Dirac integral was solved

for with an analytical approximation given by [87PIE]

$$\mathscr{F}_{\frac{1}{2}}(\eta) = \left[e^{-\eta} + \xi(\eta)\right]^{-1} \qquad (27)$$

where

$$\xi(\eta) = 3\sqrt{\frac{\pi}{2}}\left[(\eta + 2.13) + \left(|\eta - 2.13|^{2.4} + 9.6\right)^{\frac{5}{12}}\right]^{-\frac{3}{2}} \qquad (28)$$

The final step in the analysis of the Hall data consisted of solving for the apparent Hall

carrier concentration using the calculated values of n_Γ and n_L calculated from equations 25

and 26. The Hall coefficient is actually the weighted average of the carrier concentrations in

two bands given by

$$R_H = \frac{n_\Gamma \mu_\Gamma^2 r_\Gamma + n_L \mu_L^2 r_L}{e(n_\Gamma \mu_\Gamma + n_L \mu_L)^2} \qquad (29)$$

where e is the elementary charge, μ_Γ and μ_L are the mobilities in each of the bands and r_Γ and

r_L are the scattering coefficients related to the minima. It should be noted that the carriers

trapped in the impurity band associated with the L-band does not contribute significantly to

the conductivity and all coefficient because of their very low mobility value ($\mu_i = 2 \, \text{cm}^2 \cdot \text{V}^{-1} \cdot \text{s}^{-1}$)

[74SUN]. However, the thermal equilibrium carrier concentrations in the two bands are

affected by the impurity band as indicated in the charge neutrality equation. The scattering

coefficients for each band were each taken to be one which is a valid assumption since they

were calculated to be less than 1.1 for all carrier concentrations at 300 °K [95CHI]. With this assumption, Equation 29 can be reformulated to calculate the apparent carrier concentration by

$$n_H = \frac{\left(n_\Gamma + n_L \left(\frac{\mu_L}{\mu_\Gamma}\right)\right)^2}{n_\Gamma + n_L \left(\frac{\mu_L}{\mu_\Gamma}\right)^2} \tag{30}$$

The mobility ratio in the above equation was estimated to be 1/6 by Sagar and this result was used as a starting point in the calculation. Variations from this value allowed a better fit to the data and this point will be discussed later. As a final step, the result of the calculated apparent carrier concentration was compared to the experimental data and N_D, ΔE, and $d(\Delta E)/dT$ were varied until the best fit to the data was found.

The samples chosen for variable temperature Hall measurements were, in order of lower to higher carrier concentration levels, one sample regrown on earth, one sample regrown in space, and one sample in the as-received condition. The results of the fit to the measurements for the n-type samples are given in Figures 48-50. These graphs simultaneously shows the carrier concentrations in the two bands which, when added together, give the total carrier concentration. This value differs from the total number of carriers (which is a temperature independent constant) because of the carrier frozen into the impurity state associated with the higher energy band. Again, from equation 30, the apparent carrier concentration as measured by the Hall effect can be compared to the actual data. The final fit for all three curves is made more visible in Figure 51. The ionization energy used in the calculation for

the lowest doped sample was 13.8 meV and this was decreased to 10 meV for the intermediately doped sample and finally to 4 meV for the highest doped sample. The discussion of the variables in the fit for a variable doping levels follows below.

For the two lower doped samples (the two regrown samples), at low temperatures, the concentration of carriers is small in the subsidiary L-band and the apparent carrier concentration is essentially equivalent to that of the total concentration of carriers. This is because the carriers do not have enough thermal energy to be promoted to either the higher energy band or the donor states below this band, even if the Fermi level is relatively close to the subsidiary valley. As the temperature is raised, the Fermi level drops (Figure 52) as the density of states in the central band increases; however, the concentration of carriers in the subsidiary valley increases causing the apparent carrier concentration to drop according to Equation 30. The concentration of carriers in the L-band (n_L) in the lower-doped samples is primarily controlled by the energy gap between the center and subsidiary bands, ΔE and its variation with temperature over the measured temperature range, $d(\Delta E)/dT$. For the low-doped samples, the concentration of carriers trapped in the donor level associated with the L-band increases with temperature as more carriers are thermally promoted to this level, but afterwards, the concentration decreases again as the Fermi level drops. The total concentration of trapped carriers in the low-doped samples is in general about one order of magnitude smaller than the total carrier concentration, a small, but significant value.

The variation of the higher-doped as-received sample is primarily controlled throughout the whole temperature range by the concentration of carriers in the subsidiary valley and the concentration of carriers in the donor state associated with this valley. In contrast to the other

two samples, this occurs even at lower temperatures because with the higher doping levels, the Fermi level is close to the subsidiary band.

The value of 1/6 for the mobility ratio was calculated by Sagar from the change in Hall coefficient of one sample. Other authors have used this mobility value to determine ΔE and $d(\Delta E)/dT$ for n-type GaSb. However, it was found through careful examination those papers, and through the manipulation of the variables in the present experiment, that this value is inadequate to accurately describe the change in apparent Hall carrier concentration in all the samples. For example, using this value, the best fit to the sample grown on earth was ΔE=105.5 meV, $d(\Delta E)/dT$=16.8×10^{-5} eV·K^{-1}, and N_D=3.79×10^{17} while the best fit to the sample grown in space was ΔE=83.5 meV, $d(\Delta E)/dT$=3.5×10^{-5} eV·K^{-1}, and N_D=5.97×10^{17}. Note that the reference value for ΔE for all reported values is at 300°K. Also note that because the highly-doped as-received sample was controlled throughout the entire temperature range by the concentration of carriers in the L-band, a suitable fit could be found for the Hall data by varying the three variables over a large range; therefore the results of this sample with a mobility ratio of 1/6 are irrelevant to the discussion.

It was decided to take the average of the above calculated fit values for ΔE and $d(\Delta E)/dT$ for the two regrown samples at the mobility value of 1/6 and vary the mobility ratio for each sample until a good fit was found. An excellent fit to the data was found using this approach for ΔE=95 and $d(\Delta E)/dT$=10×10^{-5} eV·K^{-1} by changing the mobility ratio of the lower-doped earth grown sample to 1/4 and that of the higher-doped space grown sample to 1/8. This increase in mobility ratios with increasing carrier concentration is consistent with the general trend of the calculated mobility ratios by Harland and Woolley [66HAR]. Unfortunately,

with these results, a good fit to the highly-doped as-received sample is not possible with the above values for the gap in the conduction band minima. The value of ΔE in the low temperature range is very close to the donor level at the subsidiary band causing a large number of carriers to be frozen at this level. A better fit to this sample is realized by decreasing $d(\Delta E)/dT$ to 5×10^{-5} eV·K^{-1} and thus increasing difference in Fermi and donor state levels. This is done with only a slight consequence to the fits of the two regrown samples.

As outlined by Kourkoutas et al. and illustrated in Table 9, there is a large scatter in the results of previous authors for ΔE [84KOU]. A graph of these previous results, along with the results of this study are given in Figure 53. Values for the this energy separation in general fall in the range of 75-120 meV at room temperature and the corresponding values for the temperature coefficient fluctuate from -2×10^{-4} to 2×10^{-4} eV·K^{-1}. Nevertheless, as shown in the figure, the results of the experimental data in the present experiment compare favorably with some past results. Most notably, Chen [90CHE] had a energy separation value of 95 meV at 300°K and a temperature coefficient of 13.5×10^{-5} while Szlenk [71SZL] had a energy separation value of 100 meV at 300°K and a temperature coefficient of 14×10^{-5}.

A better fit to all the data could be realized with simultaneous analysis of the Hall data with other transport measurements to determine the variation in the mobility ratio as a function of temperature. For example, Mathur and Jain [79MAT] analyzed both Hall and transverse-magnetoresistance measurements to determine not only the carrier distribution, but also the relaxation times in both the bands (which translates to a variable mobility ratio). Similarly, Lee and Woolley performed a rigorous analysis of heavily-doped samples using Hall coefficient and electrical conductivity as a function of temperature and as a function of

Table 9 - Previously calculated conduction band energy separation values and its temperature coefficient given by other authors.

Author	$\Delta E_{\Gamma L}$ (meV)	Reference Temperature (K)	α (eV·K^{-1})	Method Used
Sagar [60SAG]	74	300	-3×10^{-4}	Piezoresistance and conductivity
Piller [63PIL]	80	296	1.1×10^{-4}	Faraday rotation
Harland and Wooley [66HAR]	84	0	8×10^{-5}	Hall, magnetoresistance
Averous [70AVE]	120	300	2.1×10^{-4}	Piezoresistance and Hall
Szlenk and Walukiewicz [71SZL]	58	0	1.4×10^{-4}	Hall and conductivity
Basinski et al. [72BAS]	97	0	-3.4×10^{-5}	Hall and magnetoresistance
Robert and Barjon [70ROB]	77	4.2	-2×10^{-4}	Hall and magnetoresistance
Chen and Cho [91CHE]	95	300	1.35×10^{-4}	Hall
Present Work	95	300	5×10^{-5}	Hall
	95	300	10×10^{-5}	Hall

pressure at room temperature, magnetoresistance as a function of magnetic field at different temperatures, and Nernst-Ettingshausen coefficients as a function of magnetic field. Moreover, the assumption parabolic energy bands does not strictly hold for most III-V materials. Such a study is beyond the scope of the present experiment; however the fit to the carrier concentration data would undoubtably improve with a variable mobility ratio as a function of temperature and with non-spherical energy surfaces.

The Hall mobility for the three doped samples is given in Figure 54. With increasing temperature, the mobility decreases for the as-received sample (59/4 seed slice #0) while it increases for the regrown earth sample (59/4 seed slice #2). The regrown space sample (UFL2 GaSb Tail 6) is a combination of these two curve with increasing values until about 120 °K before decreasing. Mathur and Jain [79MAT] have calculated that ionized impurity scattering dominates the mobility values in the Γ band where most of the activity takes place. In the higher doped sample, screening of the ionized impurities by the high electron concentration decreases the ionized-impurity scattering as temperature is lowered. In the lower doped sample, the influence of the screening is not as much due to the low carrier concentration. Therefore, the ionized impurity scattering limited mobility increases with increasing temperature as the carrier momenta are less randomized by ionized scatters at increased velocities. The intermediately doped space sample illustrates a competition of these two effects across the temperature range.

<u>Room Temperature</u>

The variation of room temperature Hall coefficient (carrier concentration), mobility, and resistivity along the length of each rod was performed by conducting measurements on the wafers cut from the regrown rods. The results for the p-type samples are given in Figures 55-57. There appears to be no effect on growing the samples in space on the carrier concentration within experimental error and normal sample variation. The results range from 9.7×10^{16} to 2.8×10^{17} for all samples and in general fall within $1-2 \times 10^{17}$ range. This is consistent with all previous studies on GaSb grown from a stoichiometric melt since the

1950's (see for example Leifer [54LEI]). The mobility data range from 405 to 844 $cm^2V^{-1}sec^{-1}$ and in general are centered around 650-700 $cm^2V^{-1}sec^{-1}$ which is also comparable to past results [54LEI], even in samples grown by molecular beam epitaxy [95BOS]. The resistivity of the samples ranges from 0.040 to 0.077 ohm·cm centered around 0.06 ohm·cm, again representative of bulk grown samples [54LEI]. Thus, there appears to be negligible difference among the samples with gravity as a variable.

The doped samples are complicated by the fact that the Te concentration varies along the length of the sample due to the micro- and macrosegregation phenomenon. Figure 58 shows that in the case of the regrown space sample, the carrier concentration in the seed drops at the initial interface to values so low that the material becomes p-type due to the higher concentration of native acceptors present in the sample. The wafers in this region did not exhibit coherent experimental results in the beginning sections of the rod which is most likely attributed to inhomogeneous dopant distribution across the samples. Note that this effect is prominant as the dopant level approaches the compensated range of values in the nominally undoped samples. The transition to n-type samples is seen at about 17.5 mm into the growth of the sample. The sample centered around 19mm is just after the transition and the measured carrier concentration is less than the native acceptor concentration in the undoped samples. Afterwards, the concentration increases with increasing Te-concentration according to the macrosegregation rules for zone-processed samples previously described above. When the last-freeze zone is reached, the carrier concentration continues to follow the rapid increase in Te-concentration as viewed by the SIMS results.

In this same sample, before the regrown section (the seed section), the mobility is seen to initially drop with increasing doping levels as shown in Figure 59. In the measurable samples near the last freeze zone, the doping level is decreased due to macrosegregation and the mobility returns to higher levels. Theoretical calculations by Chin [95CHI] have shown that at 300°K, ionized impurity scattering in both the Γ and L band becomes increasingly significant as the carrier concentration increases to the range of concentrations observed in this study. The highest measured room temperature mobility is ~3500 cm^{2}V^{-1}sec^{-1} which is near the level of previous studies whose carrier concentration is in the low to middle 10^{17} range (see for example Chin [95CHI]).

As shown in Figure 60, the carrier is n-type in all wafers of the regrown earth rod GaSb 59/4. This reflects the slightly higher initial doping concentration in the as-received rod. In fact, the first sample after the initial interface is barely n-type instead of p-type as in the space-grown sample. Afterwards, the carrier concentration is seen to vary considerably and does not appear to follow the rules for macrosegregation. This is most likely due to the strong variation in the zone height and/or convection during processing causing variations in the growth velocity of the solid/liquid interface. As shown earlier in the SIMS data for the space-grown Te-doped sample, even a minor disturbance such as a five second duration lamp pulse can cause the Te dopant to increase by ~15%. The change in growth velocity will in turn change the effective distribution coefficient and thus the Te concentration in the solid. Figure 61 shows the processing parameters for this sample. One can see a large decrease in the zone height between 5 and 14 mm after the initial solid/liquid interface which in turn would cause an increase in the growth velocity of the solid/liquid interface. This appears to be correlated

with the large increase in carrier concentration in this range. As seen by the equation for k_{eff} (equation 7), as the growth rate is increased, k_{eff} would increase thus distributing more dopant at the interface. After 15 mm, the carrier concentration drops to lower values and varies in the low 10^{17} range for the remainder of the growth. The initial drop can be correlated with the increase in zone height at this point.
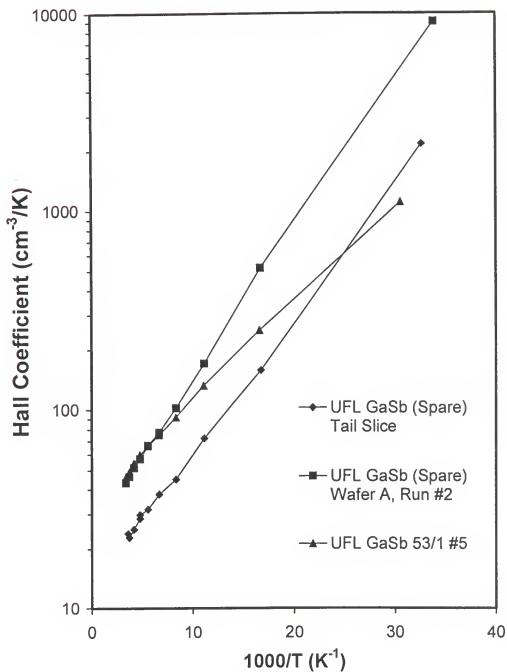
Figure 41 - Temperature dependence of the Hall coefficient for the three undoped samples.
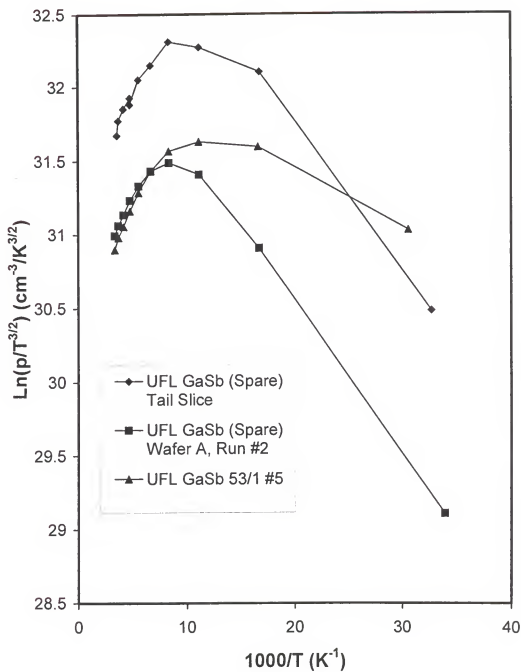
Figure 42 - Plot to determine acceptor level activation energy for the case of compensated samples. The slope determined was for the low temperature section of the curve.
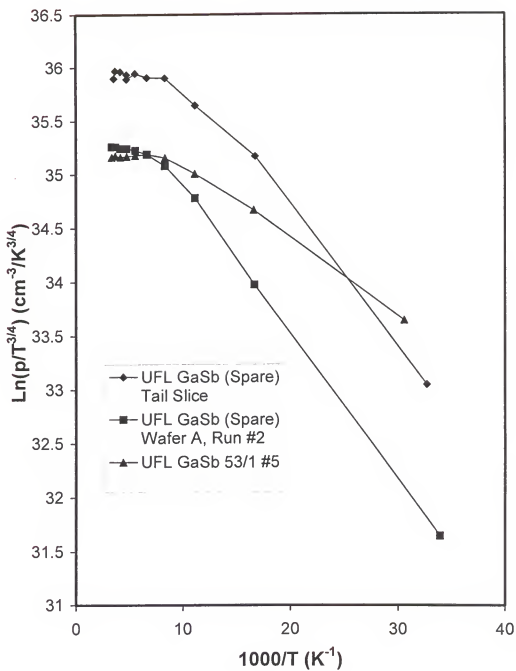
Figure 43 - Plot to determine acceptor level activation energy for the case of uncompensated samples. The slope determined was for the low temperature section of the curve.
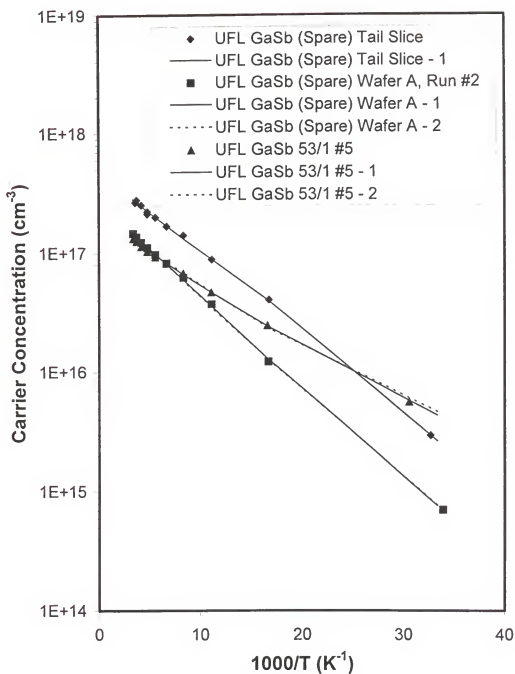
Figure 44 - Curve fit to undoped samples with one acceptor level for $N_v=7.93\times10^{14}T^{3/2}$. Note that in general, there are two possible solutions to each set of data points.
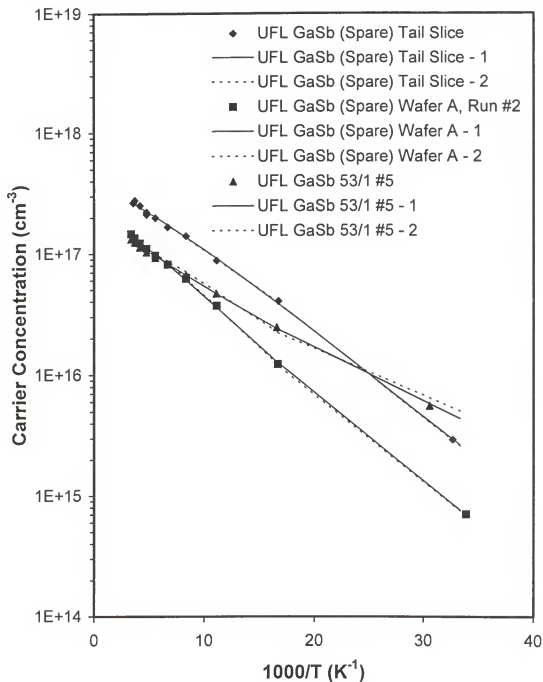
Figure 45 - Curve fit to undoped samples with one acceptor level for $N_v=1.81\times10^{15}T^{3/2}$. Note that, there are two possible solutions to each set of data points.
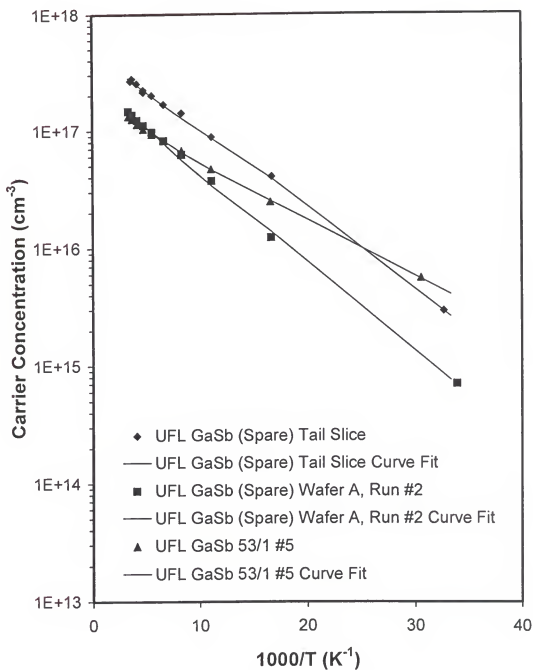
Figure 46 - Curve fit to undoped samples with two acceptor levels.
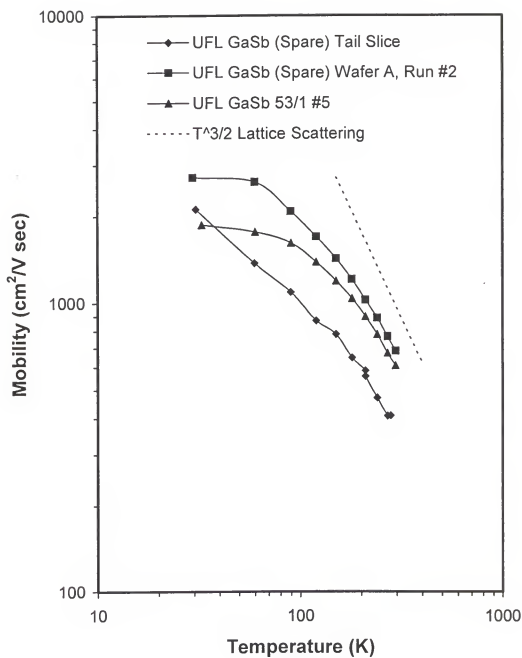
Figure 47 - Variation of Hall mobility with temperature for the three undoped samples.
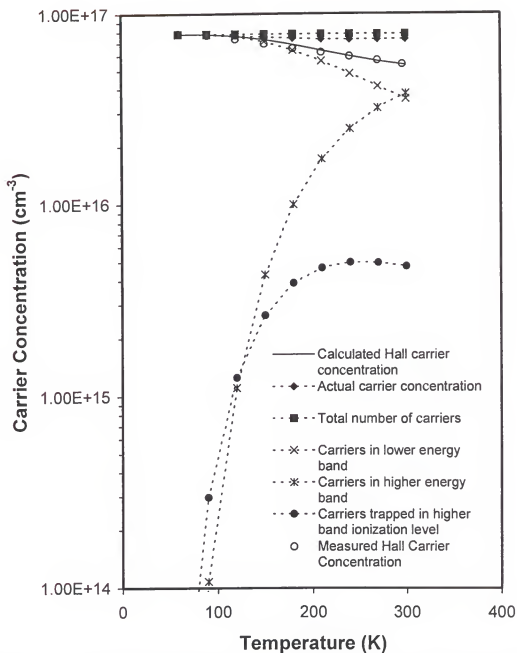
Figure 48 - Curve fit to the apparent Hall carrier concentration for the earth processed sample 59/4 #2. Also shown are the total number of carriers, total free carrier concentration, the carrier concentration in the two energy bands and the ionization level associated with the upper energy band.
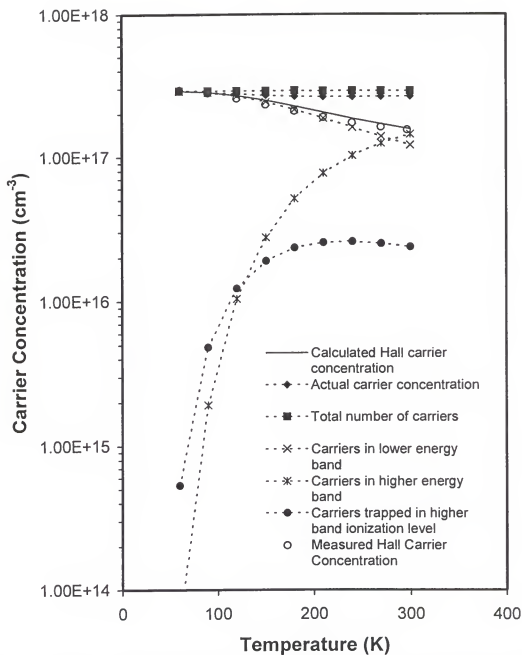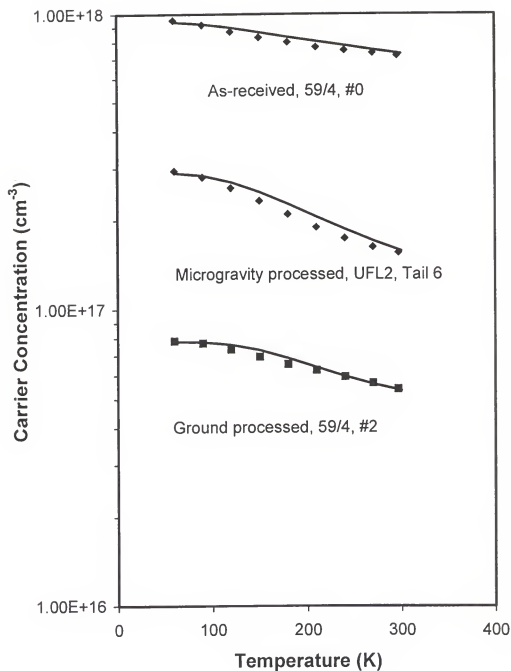
Figure 49 - Curve fit to the apparent Hall carrier concentration for the space processed sample UFL2 Tail 6. Also shown are the total number of carriers, total free carrier concentration, the carrier concentration in the two energy bands and the ionization level associated with the upper energy band.
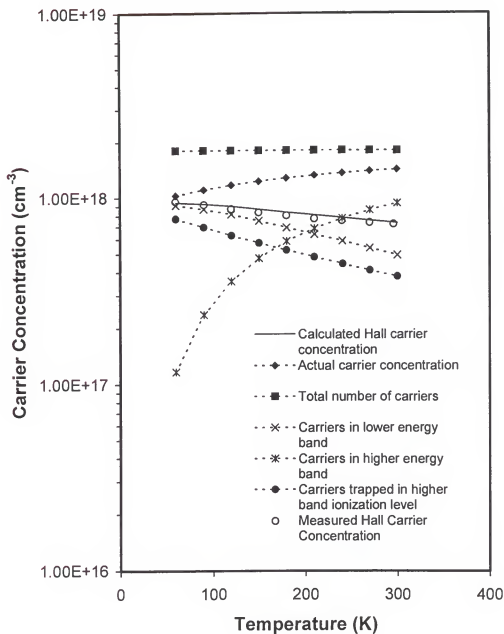
Figure 50 - Curve fit to the apparent Hall carrier concentration for the as-received sample 59/4 #0. Also shown are the total number of carriers, total free carrier concentration, the carrier concentration in the two energy bands and the ionization level associated with the upper energy band.

Figure 51 - Summary of the curve fits to the apparent Hall carrier concentration for the three n-type samples studied.
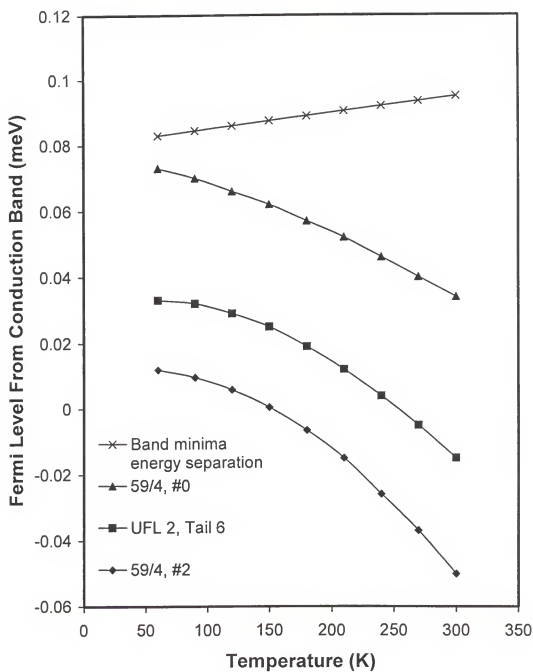
Figure 52 - Fermi level positions for the three n-type samples studied as determined by the curve fit.
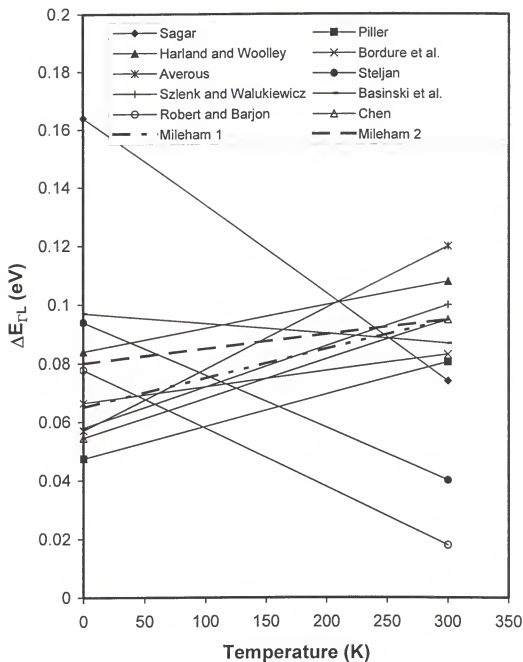
Figure 53 - Comparison of results for the variation with temperature of the difference in energy between the conduction band minima. The two dotted lines are the results of this study.
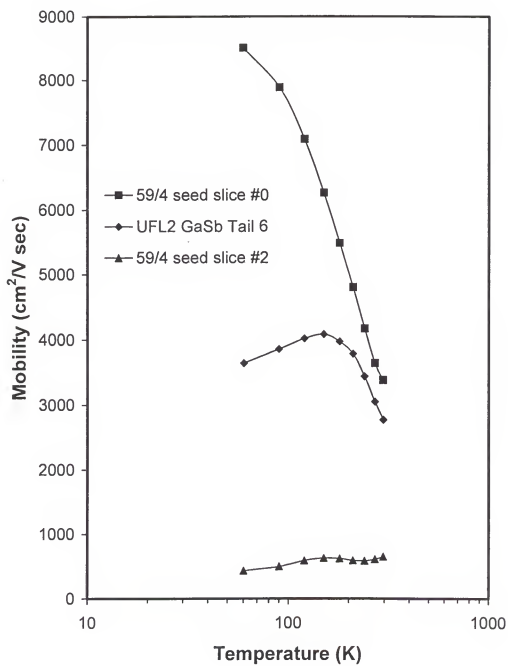
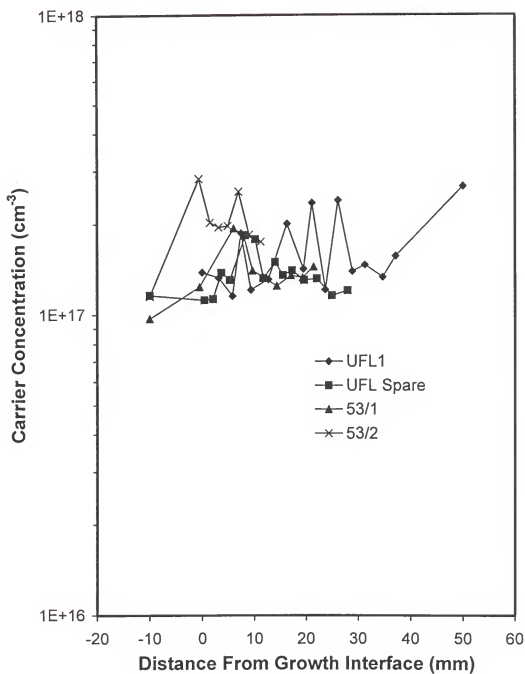Figure 54 - Variation of Hall mobility with temperature for the three doped samples.

Figure 55 - Variation of the Hall carrier concentration along the length of the grown rod for the four undoped samples.
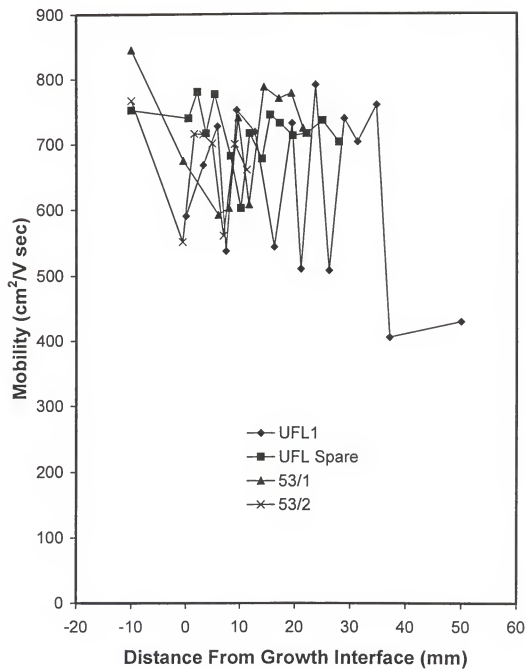
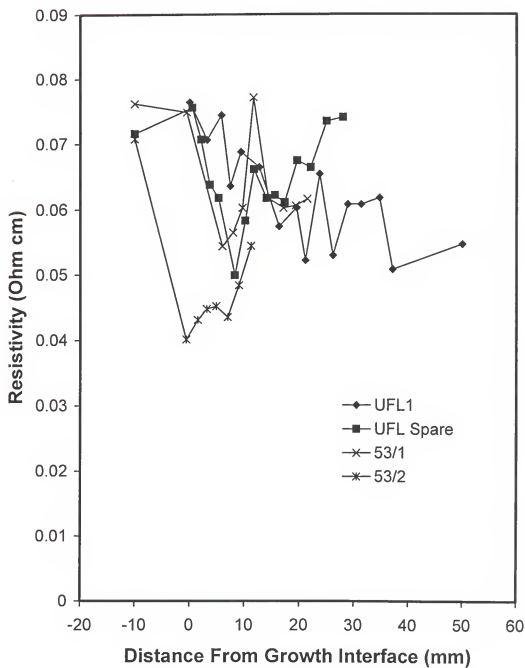Figure 56 - Variation of the Hall mobility along the length of the grown rod for the four undoped samples.

Figure 57 - Variation of the resistivity along the length of the grown rod for the four undoped samples.
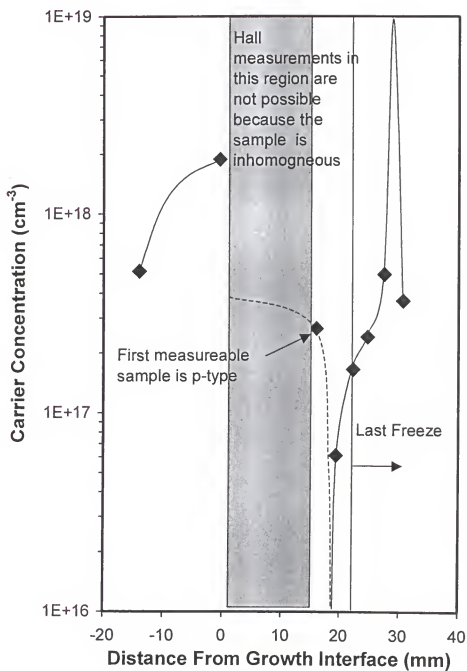
Figure 58 - Variation of the Hall carrier concentration along the length of the grown rod for the space-grown doped sample (UFL2, GaSb).
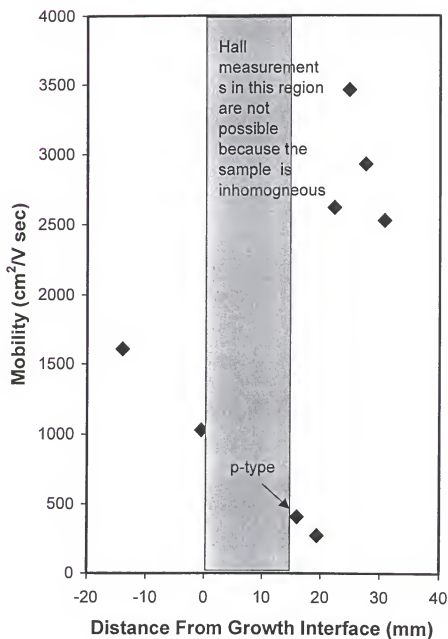
Figure 59 - Variation of the Hall mobility along the length of the grown rod for the space-grown doped sample (UFL2, GaSb).
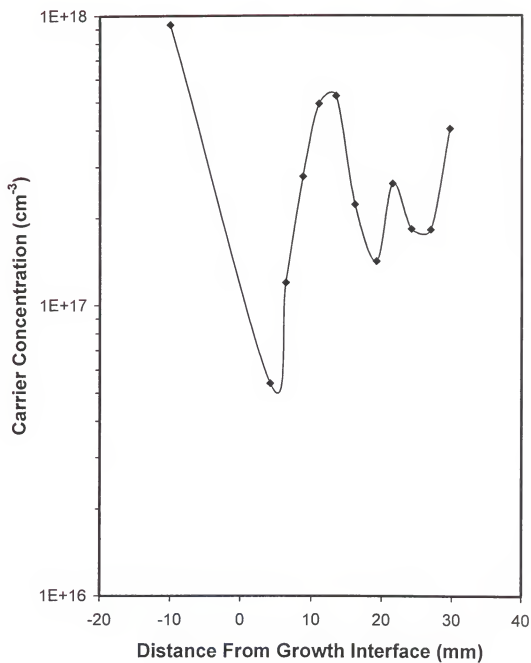
Figure 60 - Variation of the Hall carrier concentration along the length of the grown rod for the earth-grown doped sample (59/4).
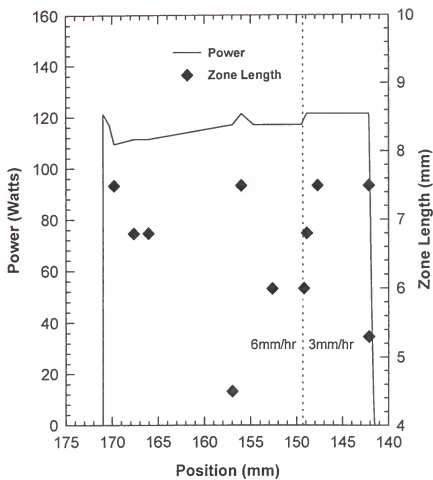
Figure 61 - Variation of zone height and power with position for sample 59/4.

PHOTOLUMINESCENCE RESULTS AND DISCUSSION

p-type Samples

Liquid Helium Measurements

The three undoped samples tested in the variable temperature Hall measurements were also tested with photoluminescence measurements at 4.5 °K with variable input powers ranging from 1-26.5 W/cm^2. The results are shown in Figures 62-64. In Figure 65, the 26.5 W/cm^2 curve for all three graphs was regenerated with a broken scale in the PL intensity axis to better show the lower intensity peaks. The dominant features in all spectra are the transitions centered at 775.4-777.4 and 792.3-794.3 meV depending on the sample and/or input power. Other peaks are found at 746.4-750.1, 753.7-756.5, 763.0-765.8, 799.5, and 807.8-809.9 meV depending on the sample and input power. A summary of the peaks observed in the undoped p-type samples is given in Table 10 and is discussed in detail below.

The dominant transition in all graphs is well recognized as being related to the neutral state of the dominant acceptor (designated A in the literature). In this study, based on experimental observation at low temperatures alone, it is difficult to tell if the transition is of the donor-acceptor pair (DAP) type or of the free electron to bound neutral acceptor (e–A°) type. In all samples, a shift of ~1-1½ meV over a two decade change in power input is observed, which translates to a 0.5-0.75 meV shift per decade of power. For a DAP

157

Table 10 - PL transitions visible in the undoped samples at 4.5 °K.

hν (meV)	Line Designation	Notes
808.9	FE	Free exciton
799.5	D	Conduction band-acceptor transition, E_A=12.5 meV
793.6	BE	Bound exciton
776.7	A	Conduction band-acceptor transition to neutral state of the native double acceptor, E_A=35.3 meV
764.4	BE-LO	LO-phonon replica of line BE
755.5	B	Band-acceptor transition, E_A=56.5 meV
748.2	A-LO	LO-phonon replica of line A

transition, one would expect a 1-2 meV shift in energy with each decade increase in power [95SKR]. In fact, unlike this study, one study found a shift of this magnitude per decade increase in laser power [95DUT] while another study has found an intermediate increase in peak energy of 1 meV per decade increase [88JOH]. While this increase is typically recognized as the hallmark of DAP transitions, it should be noted that the peak energy of a free to bound transition can also increase with excitation power, at a lower rate [91CHI]. With higher excitation power, the quasi-Fermi level for the electrons is driven further up into the conduction band, and because the acceptor state is relatively localized, conserved k transitions are still allowed at higher energies. Therefore, at low temperatures, a shift of the order of the quasi-Fermi level shift is expected.

When the peaks of the samples are normalized and plotted on top of each other as in Figures 66-68, one notices that the width of the acceptor peak is found to increase in all three samples, all on the high energy side. This is also predicted for both (e–A°) and DAP peaks.

The former type is broadened with increasing excitation energy as the electron population is heated by the photoexcitation [95SKR]. The nature of this transition in this study will be further elucidated upon in the discussion on the temperature dependence of the peak.

Above the acceptor-related transitions, the peaks are generally regarded as excitonic in nature. Evidence for the exitonic nature of the peaks can be investigated by examining the variation of the peak height as a function of laser power density, the temperature dependence of the peaks, and the full width half max (FWHM) values. The peak centered around 793 meV is the second most dominant feature in all three samples at the various input power. The peak energy position is not found to vary with excitation power which is characteristic of a bound exciton (BE) transition. Further evidence of the BE nature of this peak is illustrated in Figure 69 where the variation of the signal intensity as a function of excitation power was measured. It was found that the intensity increased superlinearly with incident power density and did not saturate at high laser powers which is also characteristic of a BE peak. This transition has been previously thought to be unique to high-quality MBE layers with low background impurities [87NIC]. However, recently this peak has also been found in bulk-grown GaSb crystals and it was concluded that the transition is intrinsic to undoped GaSb [95DUT]. Note that the widening of the neutral acceptor peak has the effect of increasing the apparent height of the 793 meV peak due to the summation of the acceptor and BE peaks. This is especially visible in the as-received and regrown microgravity samples while this effect is not as prominent in the regrown terrestrial sample where the acceptor peak width does not increase as much.

As a first order analysis, a fit to the two dominant peaks using a Gaussian profile was performed on the samples tested at the lowest input power density of 0.1 W/cm^{-2} to determine their full width at half-max (FWHM). The results for all three undoped samples is given in Figure 70. This power was chosen, because the peaks conform to a Gaussian profile better as the effects of increased photoexcitation are reduced. The results for the 777 meV related peak give an average FWHM of 5.9 meV while that of the 793 meV peak is 3.5 meV which supports the classification of these peaks as related to an acceptor and an exiton respectively.

In the regrown earth and as-received samples, an unresolved peak is found near 799.5 meV only at higher input power densities (see bottom curves in Figures 63 and 64). This peak becomes more visible as the temperature is raised and will be addressed in more detail in the variable temperature PL discussion. The peak centered 753.7-756.5 meV is unresolved in all samples, thus a FWHM and peak height are undetermined. This peak has been previously attributed to the triple native defect $V_{Ga}Ga_{Ss}V_{Ga}^{-}$ [84WEI] and has been labeled B in previous PL studies (see for example [72JAK]).

As shown in Table 11, the peaks centered around 746.4-750.1 and 763.0-765.8 are both located an average of 28.7 meV below the acceptor and BE peaks respectively. They are thus identified as the longitudinal optical (LO) replicas of these peaks, in good agreement with previously published results [72JAK, 92BAS, 95JIA]. The intensity ratio between the main peak and its replica varied between 1:0.04 to 1:0.15 for both peaks; however, as mentioned earlier, the peak heights were often misrepresented due to the addition of peaks.

Table 11 - Energy difference of the LO-phonon replicas for the two dominant peaks (Values are in meV, – indicates no phonon replica was found for that peak).

Energy W·cm^{-2}	As-received		Earth regrown		Microgravity Regrown	
	Acceptor	BE	Acceptor	BE	Acceptor	BE
0.102	29	29.4	29.2	27.4	–	–
0.204	29.9	29.4	28.3	28.4	29.1	–
1.02	27.2	29.4	28.3	27.5	30	–
10.2	28.2	29.4	27.3	28.4	30.1	–
26.5	28.2	30.3	27.3	27.5	29.2	–
Average	28.375	29.58	28.08	27.84	29.6	–
Standard deviation	1.12064	0.402492	0.801249	0.512835	0.522813	–

Variable Temperature Measurements

Neutral acceptor and free exciton peaks.

The temperature variation of the PL spectra for the above undoped samples was also tested at the highest input power density of 26.5 W·cm^{-2}. Figures 71-73 gives the results. A high energy peak becomes visible as temperature is increased which is coincident with the either the calculated bandgap of the semiconductor or with the free exiton transition at that temperature. For nondegenerate conditions, the maximum of the bandgap peak is calculated to be [95SKR]

$$h\nu = E_g + \frac{1}{2}kT. \tag{31}$$

The bandgap is generally expressed by the well known Varshni equation as [67VAR]

$$E_g = E_g(0) - \frac{\alpha T^2}{T + \beta} \tag{32}$$

where $E_g(0)$ is the bandgap in eV at 0 °K, and α and β are constants with the values 3.78×10^{-4} eV·K^{-1} and 94 respectively [91SWA]. Different values for the bandgap, ranging from 811-813 meV, have been reported by several authors [65JOH, 89CHE, 91CHI, 95GHE]. From this, it is assumed that $E_g = 812 \pm 1$ meV is the actual bandgap energy. The measured peak in this study was plotted versus temperature along with the theoretical curves of Equation 31. Concentrating on the top solid curve in Figure 74, the calculated curve for the PL peak maximum closely follows the experimental data using the bandgap value of 812 meV. Note that in general, the curve is about 3 meV above the data points. This most likely results from the transition being the free exiton rather than the actual bandgap.

In Figures 71-73, the peak related to the neutral state of the native double acceptor (A) is found to broaden and shift, first toward higher energy and then to lower energies as the temperature is increased further. This maximum energy of the peak position versus temperature is also shown in Figure 74. The initial increase in energy from 4.5 to 25 °K is 1.33 meV while the decrease in the bandgap in this temperature range is 1.9 meV giving a total increase in energy of the peak of 3.23 meV. Some authors have argued that this energy shift is primarily the result of the DAP to the higher energy free electron to bound acceptor (FB) transition as the donors become thermally ionized [72JAK, 87NIC]. This argument may

or may not be true in the present study depending on how the data is analyzed and its validity is discussed as follows.

For a hydrogenic type of defect, Eagle calculated that the transition photon energy is expected to vary as [60EAG]

$$h\nu_{peak} = E_g - E_A + \frac{1}{2}kT. \tag{33}$$

That is, it should follow and remain a constant distance from the bandgap peak given by the acceptor energy level, E_A (by subtracting equation 33 from equation 31). In this study, after the initial increase in the peak energy with temperature, the peak indeed shifts toward lower energies, but not at the same rate as the bandgap peak which would be expected if the acceptor were hydrogenic in nature. This observation was also made by Nakasima [81NAK], but no detailed interpretation was given.

There are two possible explanations for this observation. First, it is possible that the peak energy level actually varies with position. This is demonstrated in Figure 74 by the bottom solid curve through the acceptor level data which is the result of an model presented by Van Vechten and Thurmond [76VAN]. Note that the actual acceptor level curve (dotted) approaches the actual bandgap curve as temperature is increased indicating the rate of decrease of the acceptor level with temperature. Also note that in the acceptor level curve, a fit to the data could not be made at lower temperatures. As discussed above, this could be explained by assuming the energy transition shift from a (e-A°) type to a DAP type as the temperature is decreased.

The possibility of a variable energy defect level is understood by looking at the thermochemistry of the ionization of defect levels. It is argued by Van Vechten that the entropy of ionization of a defect level associated with a vacancy and isoelectronic type defect is the same as the ionization of an electron across the bandgap. The neutral state of both types of reactions contains no carriers and the core of the vacancy and the isoelectronic defect is neutral. On the other hand, the ionized state of these defects necessitates the creation of both an electron and a hole similar to the case of the ionization of an electron across the bandgap. Thus, both types of reactions have the same entropy of ionization in terms of the effects of e^+ and e^- upon the softening of the lattice modes on the crystal. In contrast, for the hydrogenic type substitutional defect, no new carriers are created in the ionization reaction. The bound carrier is simply freed from the vicinity of the charged ion core. The wave function of this bound carrier is so delocalized that its effect on the bond charge and the lattice modes is essentially identical to that of the corresponding free carrier. That is, there is essentially no change in the phonon frequencies and the lattice entropy remains unchanged. The end result is that hydrogenic defects remain at a fixed distance from the valence or conduction band while the vacancy or isoelectronic type defect approaches the appropriate band as temperature is increased at the same rate as the change in energy of the bandgap with temperature. The defect associated with the level in this study is neither a vacancy nor an isoelectronic or coulombic defect. As outlined in the literature review, the energy level is believed to be related to either a Ga_{Sb} or a $V_{Ga}Ga_{Sb}$ complex. In either case, complexes and deep level defects are expected to fall within the two extremes of the vacancy and the hydrogenic cases outlined above [76VAN].

This concept is explained further by the following. The free energy of the bandgap can be expressed thermodynamically by the well known equation [76VAN]

$$\Delta E_{cv,I}(T) = \Delta H_{cv,I}(T) - T\Delta S_{cv,I}(T) \tag{34}$$

where $\Delta E_{cv,I}$, $\Delta H_{cv,I}$, $\Delta S_{cv,I}$ are the free energy, enthalpy, and entropy of ionization of a charge across either the bandgap (cv) or the defect level (I) as a function of temperature, T. For the case of the defect level, one can see that if $\Delta S_I(T)=0$, then the energy level remains constant over the entire temperature range since $\Delta S_I(T)=\partial \Delta E_I/\partial T=0$ (i.e. $\Delta E_I(T)=\Delta H_I(T)=\Delta E_I(0)$). However, if $\Delta S_I(T)=\Delta S_{cv}(T)$, as in the case of the vacancy or isoelectronic defect, then $\Delta E_I(T)$ varies with the bandgap variation, $\Delta E_{cv}(T)$. The energy of the bandgap was given above by Equation 32. Thus the entropy of ionization is obtained by taking the temperature derivative of this equation

$$\Delta S_{cv,I} = \frac{\alpha_{cv,I} T(T+2\beta)}{(T+\beta)^2}. \tag{35}$$

where α and β are defined in a similar manner as equation 32.

The results presented in Figure 74 illustrate the analysis of this study's results based on the variable free energy model. The acceptor energy level, E_A and the α value in the Varshni equation for the ionization level were allowed to vary in an attempt to fit the data. The best results were found with an acceptor energy level of 31 meV and an α of 9×10^{-5} eV·K^{-1}. Thus, by taking the ratio of α_I to α_{cv}, one obtains $\Delta S_I(T)=0.24\Delta S_{cv}(T)$. This result is between the two extremes of $\Delta S_I(T)=0$ for the hydrogenic donor and $\Delta S_I(T)=\Delta S_{cv}(T)$ for the vacancy or

isoelectronic type defect. A plot of the variation in acceptor energy of the acceptor level with temperature, along with the two extreme cases, is given in Figure 75. Again, the lowest temperature point is high because the energy is increased at low temperatures due to the possibility of a transition from band-to-acceptor to donor-acceptor-pair. Also, the data was increased by 2.5 meV to reflect the difference between the free exitonic transition and the actual bandgap.

The second explanation for the variation of energy of the neutral acceptor peak with temperature is based on Eagle's calculation for the peak energy of a free electron to bound neutral acceptor transition (recall Equation 33) [60EAG]. The $\frac{1}{2}kT$ term results from the calculation of the photoabsorption cross section for scattering an electron initially bound to an isolated acceptor into a final conduction band state. Eagle's model is based on the assumptions that the electron quasi-Fermi level$\ll kT$ (classical limit), the acceptor levels are infinitesimally narrow, and that the capture cross-section for radiative capture of the electron by a neutral acceptor varies inversely with the electron energy. The most likely cause for a deviation in the present study would result from the fact that the cross section may not vary inversely with the electron energy [75ASH] which could result in a larger prefactor than $\frac{1}{2}$ in front of the kT term.

Figure 76 presents a similar graph to that of the variable energy model graph (Figure 74) and shows that the data for the present model is best fit when the prefactor term before kT is increased to 1.45. Note that in this analysis, the actual acceptor transition remains a fixed distance, E_A, from the bandgap, as opposed to Van Vechten's variable energy interpretation. This fit was obtained by assuming a free to bound transition at all temperatures. That is, the

possible shift to DAP transition at low temperatures was not taken into account as in the variable acceptor energy model. This interpretation is more consistent with the results presented in the low temperature measurements at variable input powers where the acceptor transition was found to shift only slightly as the input power was increased. (Recall that an increase of 1-2 meV per decade increase in excitation energy is expected for a DAP transition). Concerning the other assumptions of Eagles model, it is possible that the quasi-Fermi level is larger than kT for the lowest temperatures, but this effect should also be visible in the bandgap variation and would cancel. In addition, it is possible that the acceptor level has some finite line width, perhaps 1-2 meV, but this alone cannot explain the large shift in the peak over the temperature range of this study.

The use of a prefactor other than ½ was also found for other material systems. Colbow [66COL] found that the shift was closer to $1kT$ in CdS, which was also predicted theoretically by using an energy-independent capture cross section, as opposed to varying inversely with electron energy as in Eagle's model. Even higher prefactors of 1.3 [75ASH] and 1.4 [73BAC] were found experimentally in GaP suggesting an energy dependence close to $E^{\frac{1}{4}}$. The latter values are consistent with the value of 1.45 in this study.

Other peaks.

The BE peak centered at 793 meV quenches quickly with temperature and disappears between 25 and 50 °K (Figures 71-73), thus reaffirming even further its identification as a bound exiton. The most noticeable peak in terms of significance is the peak centered around 799.5 meV at 4.5 °K in the higher excitation power spectra in the regrown ground sample and in the as-received sample (Figures 63 and 64). With a bandgap of 812 meV, the

difference between this peak and the calculated bandgap at 4.5 °K is 12.5 meV and this energy value was used in the model for the variable temperature Hall measurements above. At 25 °K, the peak is dominant in the regrown ground sample and becomes more visible, although to a lesser extent, in the as-received and space regrown samples. It remains visible until about 75 °K where merges with the broad free-exciton or band-to-band recombination peak. The structural and/or elemental nature of this peak is unclear at this point; however, this level coincides exactly with the calculated $1S_{3/2}$ bound state for GaSb [96YU]. Transtions near this level have also been found by other authors; Chidley et al. [91CHI] identified a peak centered at 800 meV as a shallow free to bound (e-A°) type of transition. Other authors have found similar peaks at various energy levels in both bulk [72JAK, 95DUT] and MBE-grown [87NIC, 96BIG] crystals, but no discussion of its nature has been found.

<u>Further observations.</u>

Returning to the concept of variation of peak position with temperature, other PL studies with GaSb have also found peaks other than the dominant native acceptor to vary with temperature in a manner that was not consistent with Eagle's model. Chidley studied the traits of the above mentioned transition centered at 800 meV in great detail and found their data was best fit with a prefactor of one before the kT term [91CHI]. In Te-compensated p-type GaSb samples, Nakashima [81NAK] found that a peak estimated at ~76 meV below the bandgap at 0 °K followed the same temperature variation as the first ionization level of the native double acceptor. From this it was concluded that both peaks could be from the same defect center. However, this peak has been subsequently identified as being related to the

acceptor state simultaneously created during the incorporation of the donor dopant tellurium [96DUT]. The end result is that all transitions to neutral acceptors appear to have a variable peak transition energy with temperature. From the results of this study, this phenomena is believed to be caused by a different variation than what Eagle used for the capture cross-section for radiative capture of the electron by a neutral acceptor (i.e. an inverse variation with the electron energy).

<div align="center">n-type Samples</div>

The same three sample used in the Hall measurements were studied at variable excitation intensities. Table 12 below shows the processing background and doping characteristics of the samples. The results of the PL study are given in Figures 77-79. In general, the peaks are broad and unresolved making positive identification of some of the transitions uncertain. As noticed in the lightly-doped and moderately doped samples, the spectral distributions undergo considerable change with increasing laser excitation power density. At low excitation energy, the spectra is dominated by the transitions associated with relatively deeper acceptor levels and there is virtually no emission near the band edge. The holes generated by the laser excitation are captured by the deep acceptors in preference over the shallower acceptors. At high intensity, the spectra is increasingly dominated by high-energy transitions. As the excitation energy is increased, the larger concentration of holes created is able to neutralize not only the aforementioned deeper levels, but also the shallower acceptor levels as the quasi-Fermi level is shifted. These observations are in agreement with previous studies of GaSb crystals [72KYU, 95IYE].

Table 12 - Sample information for doped PL study. Carrier concentrations are at 60 °K.

Sample	Processing Background	Doping Characteristic
GaSb 59/4 seed 2	Terrestrially processed, ~5 mm from initial growth interface	n-type, lightly-doped (7.8×10^{16} cm^{-3})
UFL2 GaSb Tail 6	Microgravity processed, ~22 mm from initial growth interface	n-type, moderately doped (2.9×10^{17} cm^{-3})
GaSb 59/4 seed 0	As-received seed end of CZ-grown crystal	n-type, heavily-doped (9.5×10^{17} cm^{-3})

At 10 and 26.5 W/cm^2, the most prominent peaks visible are in the 707-709 and 778-783 meV range for the GaSb 59/4 seed 2 sample, while in the UFL2 GaSb Tail 6 sample, these peak levels increase to 715.4 and 793.3 meV. The lower energy peak, located ~104 meV below the bandgap in the former sample, is attributed to the ionized state of the native acceptor and is commonly designated A⁻ or C in the literature [72JAK, 87NIC, 95DUT, 96BIG]. This peak becomes visible with increased doping since the Fermi level crosses the neutral state of the native double acceptor. The higher energy peak in each of the samples is related to the neutral acceptor transition (A) previously found in the undoped samples.

There are slight, but notable differences between these two lightly- and moderately-doped wafers. In both samples, the A transition is slightly blue-shifted compared to the photon energy seen in the undoped samples, by ~1-6 meV for the lightly-doped specimen, depending on the excitation power density, and ~16 meV for the moderately-doped sample. Likewise, the peak level of the A⁻ acceptor is seen to blue shift when comparing the moderately-doped sample to the lightly-doped sample. This can be explained by considering the interplay of different effects connected with increasing the level of doping. The low energy tail of the PL spectrum is influenced by bandgap narrowing due to carrier-carrier and carrier-impurity

interactions and also to the formation of band tails due to doping inhomogeneities. The higher energy tail is mainly determined by conduction-band filling. The latter effect is dominant due to the low density of states of the conduction band in GaSb. Thus the PL band is blue-shifted by energies of the order of the Fermi-level shift. Similar results were found in other studies [96BIG].

Related to this, the height of the A peak is relatively smaller in the moderately-doped sample compared to the lightly-doped sample. At the doping levels of the samples in this study, the electrons form a degenerate gas and completely screen the shallow donors and partially the shallow acceptors. Thus, the samples with larger electron concentrations have a higher density of deep acceptors and therefore exhibit a lower intensity in the near bandgap peaks.

There is an increase in peak energy for these transitions as the excitation power increases which is even larger than that in the undoped samples. (Recall that there was a shift in energy of only ~0.5-0.75 meV in the undoped samples.) This can be caused by two factors. First, as mentioned for the undoped samples, with higher excitation power, the quasi-Fermi level for the electrons is driven further up into the conduction band and a shift of the order of the Fermi level shift is expected. Second, with such a high concentration of compensating acceptor levels in the n-type samples, the transition is expected to be of the donor-acceptor-pair type. An increase in transition energy with increased excitation energy is expected with this type of transition due to a change in occupancy of the impurity levels. It is possible that, with an increase in the number of donors in the Te-compensated sample, this effect is exacerbated when compared to the undoped state.

In addition to these two peaks, there are several unresolved transitions between the two dominant transitions in the lightly- and moderately-doped samples. Previous studies have found distinct transitions related to the Te donor at 723 meV [96BIG], 731-737 meV [72KYU, 95IYE], and 740-748 meV [95IYE, 95DUT]. The first peak at 723 meV appears in both of these samples at the lowest excitation intensity of 2 W/cm^{-2} and disappears at the two higher excitation energies. The last peak appears partially resolved in the lightly-doped sample and has been suggested to be a Te$_{Sb}^{+}$ center complexing with the V$_{Ga}$Ga$_{Sb}^{-}$ to form (V$_{Ga}$Ga$_{Sb}$Te$_{Sb}$)$^{-}$ [96DUT]. It can also be concluded from these two spectra that there is a negligible contribution from gravity levels into the incorporation of Te into the host in relation to the luminescence.

Finally, as the doping level is increased even further in the as-received sample (Figure 79), the A-band associated with the neutral acceptor transition is replaced by transitions relating to the acceptor levels of the Te donor. A rough estimate of the transition energy for the origin of this transition is as follows. The observance of a shoulder at ~836 meV in the as-received sample at the two higher excitation powers is assumed to originate from the conduction band to the A acceptor level (the dominant transition in the undoped samples). From this, a shift of ~59 meV (836 meV minus 777 meV) is calculated. Assuming the peak at 793 meV shifted a similar amount, the origin of this peak would be at 734 meV in a lightly-doped sample. As mentioned above, this is coincident with peaks related to the found in earlier studies [72KYU, 95IYE]. It appears as if the peak located in this range is weak in the lightly- and moderately-doped samples, but has become stronger as more complexes between the Te and the native acceptor are formed with increasing doping concentrations.
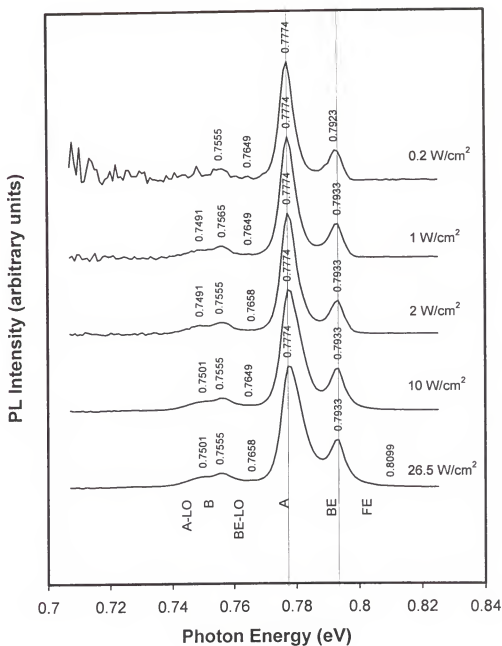
Figure 62 - Low temperature (4.5°K) photoluminescence results for the regrown space sample (UFL GaSb (Spare) Wafer A). Two lines are drawn for the two dominant peaks to help guide the eye in observing the evolution of the peak width with excitation intensity. All peaks have been normalized to the dominant peak.
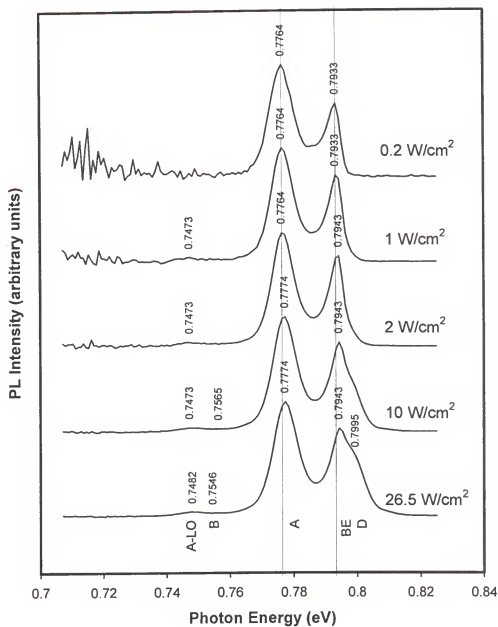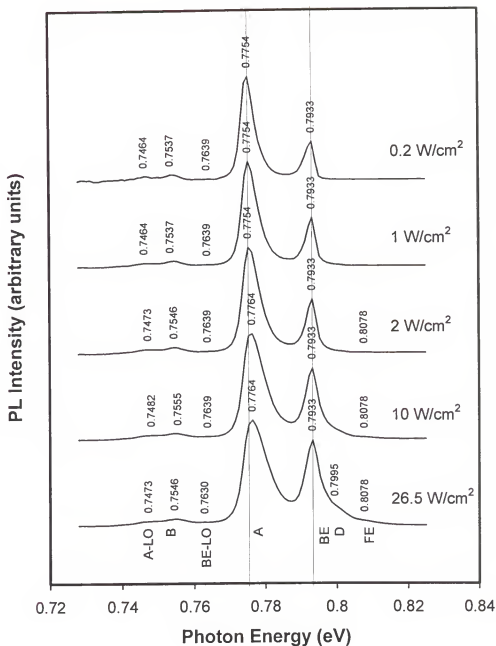
Figure 63 - Low temperature (4.5°K) photoluminescence results for the regrown earth sample (GaSb 53/1 #5). Two lines are drawn for the two dominant peaks to help guide the eye in observing the evolution of the peak width with excitation intensity. All peaks have been normalized to the dominant peak.

Figure 64 - Low temperature (4.5 °K) photoluminescence results for the as-received sample (UFL GaSb (Spare) Tail). Two lines are drawn for the two dominant peaks to help guide the eye in observing the evolution of the peak width with excitation intensity. All peaks have been normalized to the dominant peak.
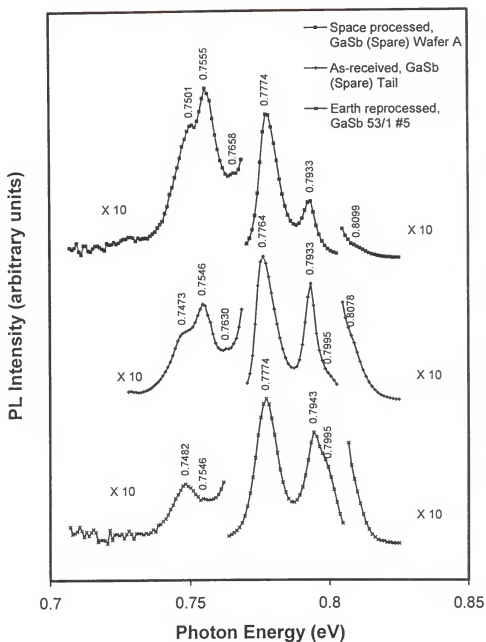
Figure 65 - PL spectra of the three p-type samples at 26.5 W/cm². The PL intensity scale has been broken to better show the lower intensity peaks. All peaks were first normalized to the dominant peak.
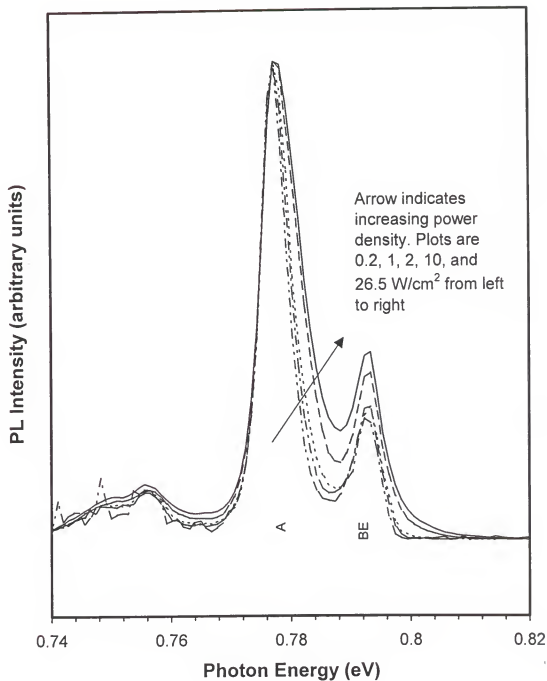
Figure 66 - Same graph as in Figure 62 (regrown space sample) except the curves are not offset to better illustrate the widening of the neutral acceptor transition (A) with increasing excitation energy.
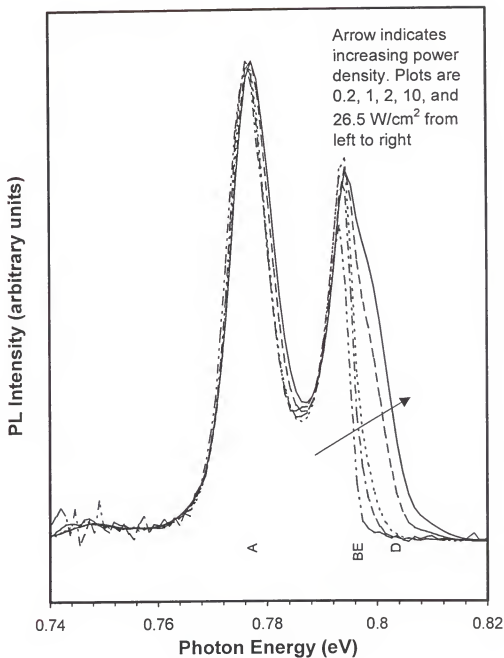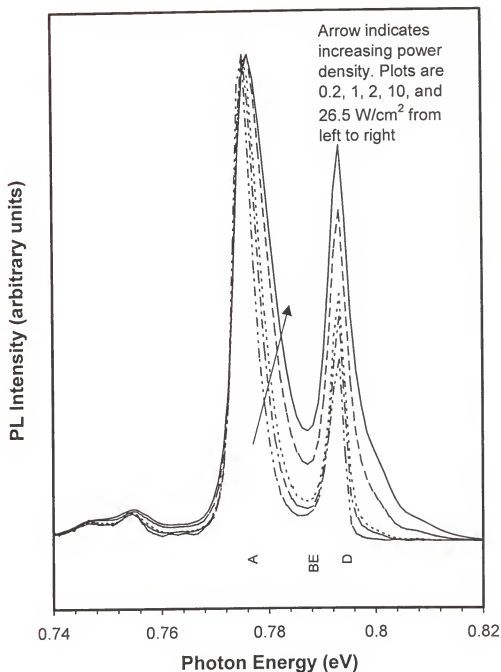
Figure 67 - Same graph as in Figure 67 (regrown earth sample) except the curves are not offset to better illustrate the widening of the peaks with increasing excitation energy. Note that in this sample, there is very little widening of the neutral acceptor peak (A) and most of the change occurs in the intensity of the peak centered at 799.5 meV (D).

Figure 68 - Same graph as in Figure 64 (as-received CZ-grown sample) except the curves are not offset to better illustrate the widening of the peaks with increasing excitation energy. In this sample, there is widening of the neutral acceptor peak (A) along with a slight increase in intensity of the peak centered at 799.5 meV (D).
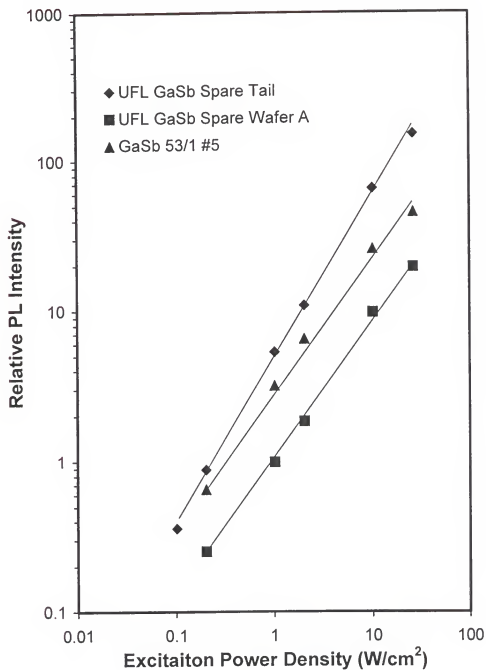
Figure 69 - Variation of relative PL intensity of the BE peak at ~793 meV as a function of excitation intensity.
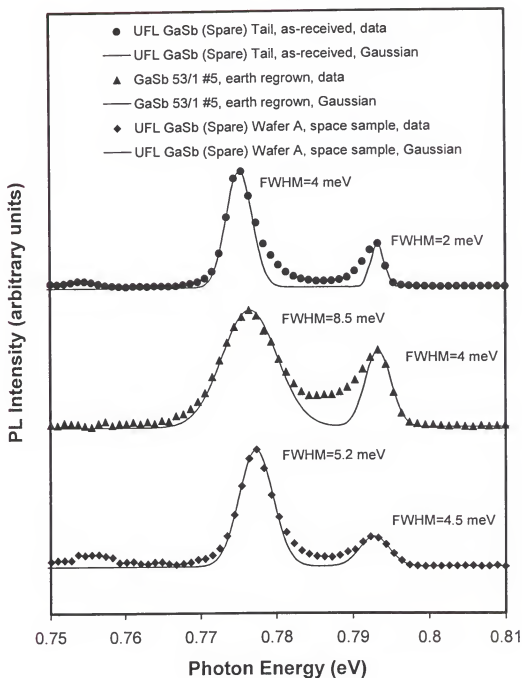
Figure 70 - Gaussian profile fit to the two dominant PL peaks in the undoped samples to determine their FWHM in a first order analysis.
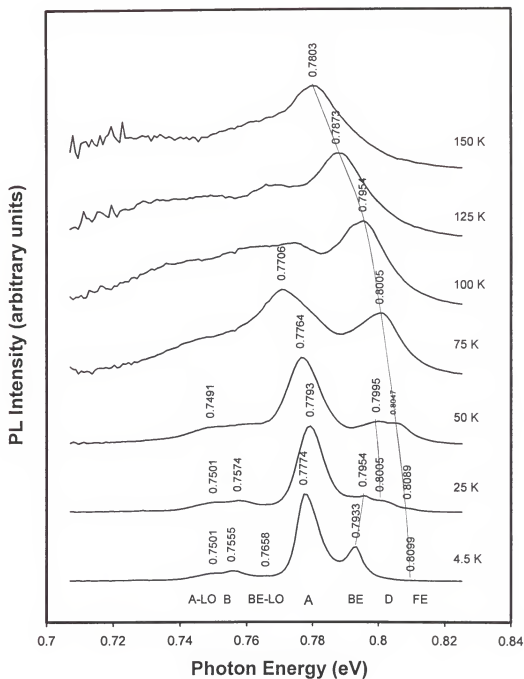
Figure 71 - Temperature evolution of the peaks for the undoped space grown sample (UFL GaSb (Spare) Wafer A).
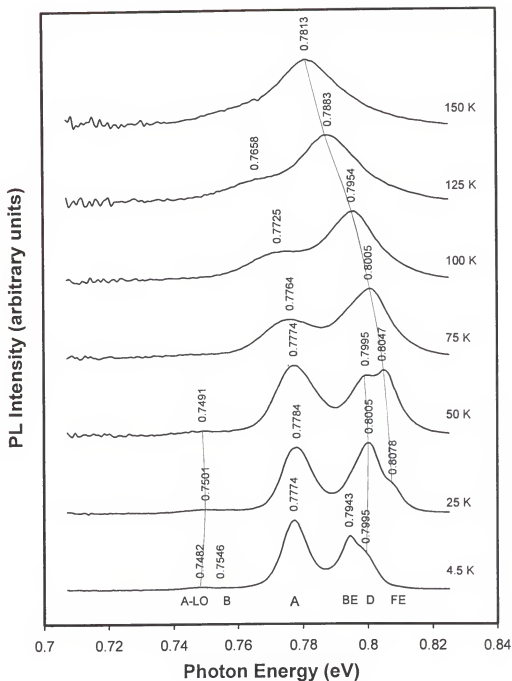
Figure 72 - Temperature evolution of the peaks for the undoped earth grown sample (GaSb 53/1 #5).
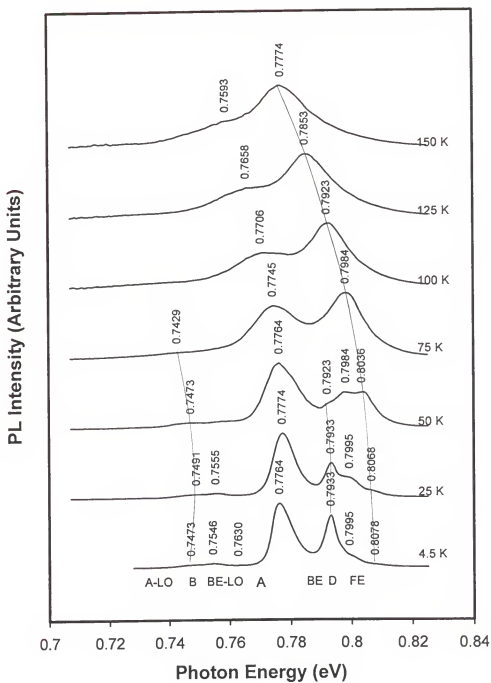
Figure 73 - Temperature evolution of the peaks for the as-received sample (UFL GaSb (Spare) Tail).
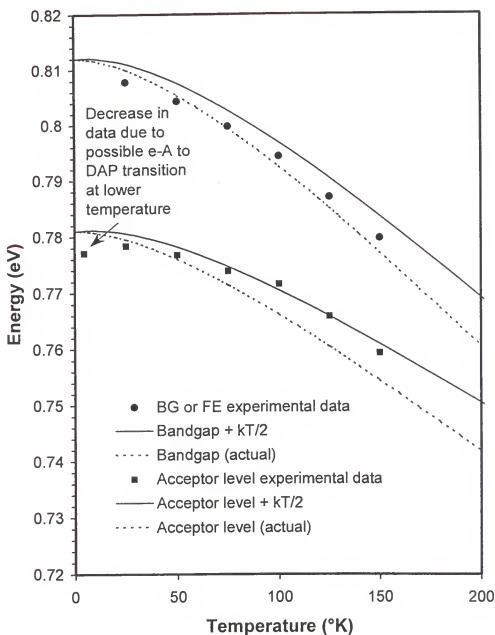
Figure 74 - Plot of the variation of photon energy with temperature for both the FE and A peaks (solid points). The curve drawn through the FE data points are based on known values for the Varshni equation. The curve drawn through the A data points are based on an analysis using a variable energy of the peak with a change in temperature. The dashed line in both curves is the actual transition energy while the solid curve is the offset peak value observed in photoluminescence.
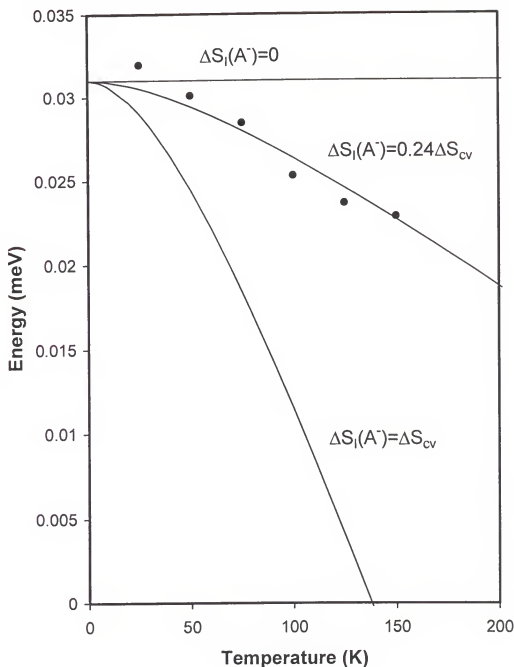
Figure 75 - Variation in the difference between the acceptor level peak (A) and the band edge with temperature. The best fit is $\Delta S_i(T)=0.24\Delta S_{cv}(T)$. This value is intermediate between the two extremes of a coulombic donor where $\Delta S_i(T)=0$ and a vacancy or isoelectronic defect where $\Delta S_i(T)=\Delta S_{cv}(T)$.
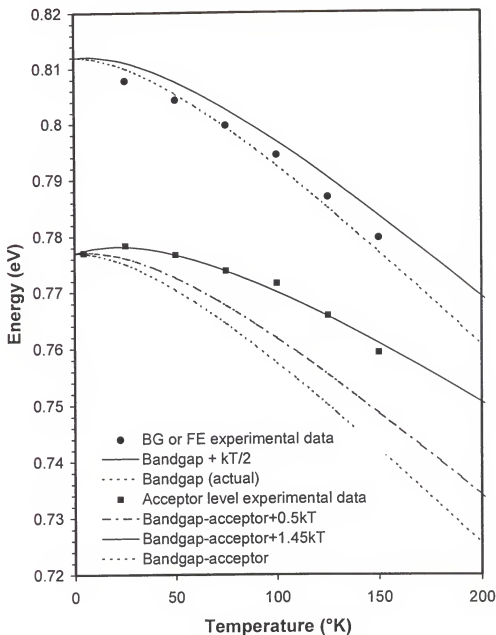
Figure 76 - Plot of the variation of photon energy with temperature for both the FE and A peaks (solid points). The curve drawn through the FE data points are based on known values for the Varshni equation. The curve drawn through the A data points are based on an analysis using a variable energy capture cross section with a change in temperature. The dashed line in both curves is the actual transition energy while the solid curve is the offset peak value observed in photoluminescence.
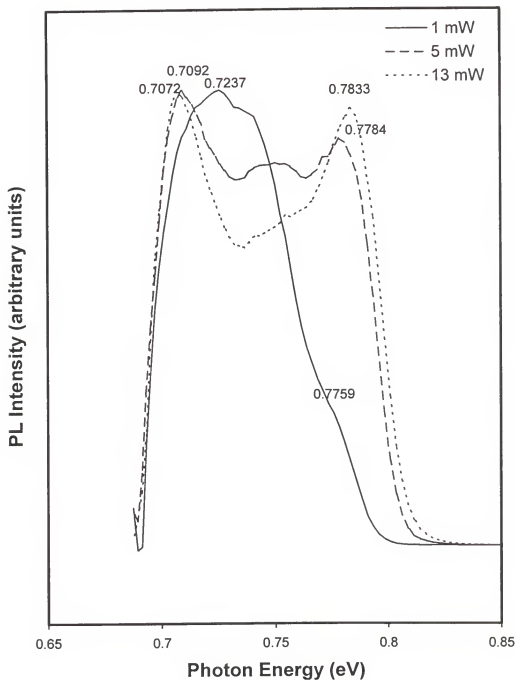
Figure 77 - Photoluminescence results for the lightly-doped regrown earth sample (GaSb 59/4 seed 2).
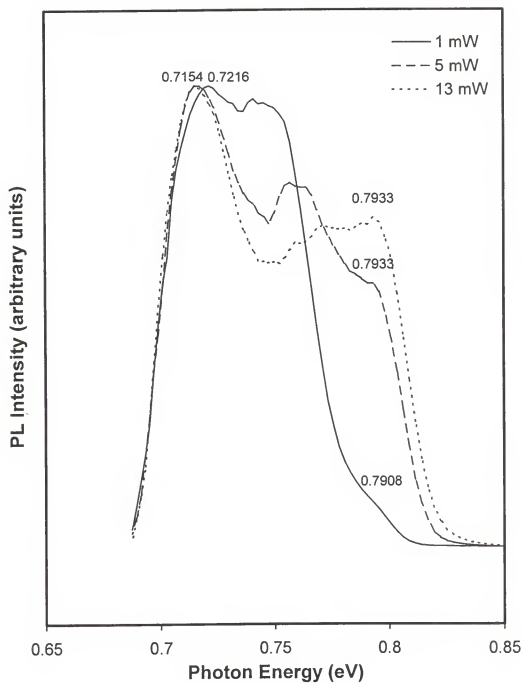
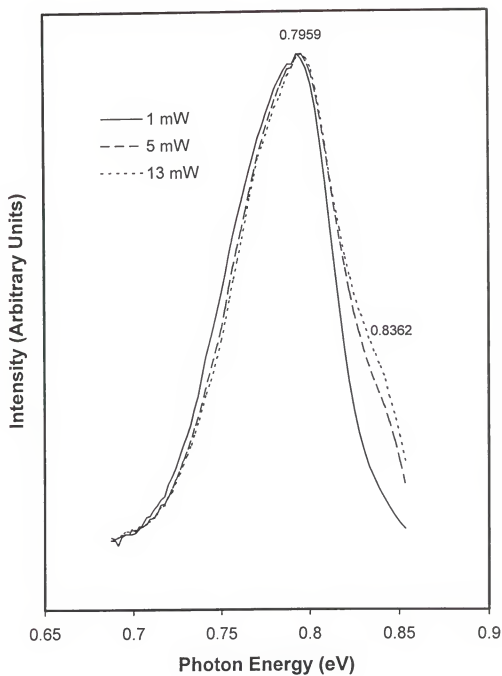Figure 78 - Photoluminescence results for the moderately-doped regrown space sample (UFL2 GaSb Tail 6).

Figure 79 - Photoluminescence results for the heavily-doped as-received sample (GaSb 59/4 seed 0).

SUMMARY AND CONCLUSIONS

Gallium antimonide was grown by the Liquid Encapsulated Melt Zone technique in both a terrestrial and microgravity environment. The microgravity experiments were performed aboard the Space Shuttle Endeavor (STS-77) as part of the Commercial Float Zone Furnace payload. The terrestrial experiments were performed at the University of Florida in a furnace of the sames design as that used in space. Following processing, the samples were characterized to determine the effects of gravity on the crystal growth of this technologically important semiconductor material.

A total of three samples were grown in space – two undoped samples and one tellurium-doped sample. Four samples were grown on earth – two undoped samples and two tellurium-doped samples. For all crystals, single crystal rods (originally grown by the Czochralski technique) were encapsulated with a eutectic mixture of sodium-chloride and potassium-chloride and surrounded by a double-walled quartz ampoule. Heating of the sample was effected by focusing light from a halogen lamp in a concentric ring around the sample in a mirror furnace. The molten zone was then translated by moving the ampoule relative to the focus point.

Single crystals were found in all three microgravity-grown samples. The earth-grown samples all started growth as single crystals, but two of the samples exhibited bicrystal or polycrystal features in parts of the sample toward the tail. Crystal shape stability was studied

191

in the microgravity samples and it was found that constant diameters are predicted for an angle of 44° between the tangent to the molten zone meniscus and the growth direction. This is much larger than the angle of 28° found for unencapsulated GaSb samples. The encapsulant reduced the line forces along the external boundaries of the crystal and the melt at the triple phase boundary. The sample attained the critical angle by reducing the diameter of the growing crystal in the initial phases of growth. In the earth-grown samples, no reduction in diameter was observed. The zones in these samples attained the critical angle necessary for stable growth at the beginning of growth since gravity forced the liquid to obtain a pear-like shape. The earth-grown samples were also found to sustain a larger stable float zone length than predicted by theory for unencapsulated samples.

The dislocation density and doping striations were studied by chemically etching the crystals. All seed samples exhibited an EPD of $\sim 10^5$ cm^{-2}. After this, all samples exhibited a reduction of dislocations as the sample was grown. A maximum reduction to 4.3×10^3 cm^{-2} was found in the tellurium-doped microgravity sample. The microgravity samples exhibited lower dislocation densities than those processed under terrestrial conditions. This can be attributed to reduced convective flows under microgravity leading to a more quiescent interface and/or to different temperature gradients due to reduced convection in the melt, encapsulant, and furnace atmosphere. Crystal doping also appeared to have a positive effect on the EPD by increasing the critical resolved shear stress in the samples. Interface curvature was observed to have a detrimental effect on the EPD of the crystals. It is assumed that the dislocation density of the samples in this study could have been reduced to values less than 100 cm^{-2} with a low dislocation density as-received crystal acting as the seed.

Growth striations were found to be highly reduced in all Te-doped samples. (Note that striations were not revealed in the undoped samples.) In the microgravity sample, rotational striations were observed in some sections of the crystal that coincided with the distance the sample moved in one period of rotation. In general the rotational striations quickly faded and disappeared toward the center of the crystal. Striations were slightly more prominent in the ground samples and were classified as strictly rotational type.

The macrosegregation of the dopant in the tellurium-doped GaSb crystals was studied by the SIMS technique. Line scans were performed along a large section of the growth axis in the microgravity crystal. The drop in concentration at the initial solid/liquid interface was explained by the distribution coefficient of tellurium in GaSb which was found to be ~0.13 in both earth and space. After this point, it was found that convective-controlled growth determined the redistribution of the dopant in the growing solid, even in space, due to g-jitters and/or Marangoni convection. The redistribution of the Te followed the well known Pfann's equation. It appears as if the molten salt was not successful in completely eliminating the convection in the molten zone of the crystal; however, as mentioned above, the convective levels were low as evidenced by the lack of striations in the grown crystal. As expected, the terrestrially-grown crystal exhibited convective-controlled redistribution of the tellurium according to Pfann's equation.

The radial segregation in the crystals was also studied by the SIMS technique. Local variations in the Te-distribution were found in the seed and tail sections of the Te-doped microgravity crystal. This was attributed to the positioning of the sample relative to the central axis of the ampoule. The presence of an argon bubble in the ampoule (which was

intentionally placed to prevent the ampoule from breaking) migrated toward the molten zone and physically pushed the sample until it hit the ampoule wall. It is believed that this caused uneven heating of the sample leading to local variations in the convective flow in the crystal. This phenomenon was not a factor for the earth-grown samples since the bubble floated in an even ring at the top of the much larger salt molten zone where the GaSb feedstock was still solid. The radial distribution in the earth-grown sample was more homogeneous in the center of the crystal than the space-grown samples. A drop in concentration near the edges of the crystal was seen and can be explained by an inflow of liquid at the solid/liquid interface at this point caused by buoyancy-driven convection.

Hall measurements were performed on all wafer samples at room temperature and variable temperature Hall measurements were performed on selected wafers. There appears to be no connection between the results and the gravity level for both sets of data. However, since GaSb is a relatively unknown semiconductor, the results were found to be important to the material system as a whole. It was discovered that the variable temperature Hall measurements performed on the undoped samples could not be adequately explained by single acceptor level model as was used in many previous studies. The results were best explained by a two acceptor approach; one level was the commonly observed native defect present in all undoped GaSb samples (at 33 meV) and the other defect level was that observed in the photoluminescence tests in this study (at 12.5 meV).

The variable temperature Hall measurements of the n-type samples were analyzed with a two-band model to take into account the effects of the subsidiary L-band minimum. This level was calculated to be 95 meV above the Γ-band with a temperature variation of 1×10^{-5}

meV/K⁻¹. For the room tempeature Hall measurements in the doped terrestrial samples, the carrier concentration and mobility were affected by the variation in the zone height. As the aspect ratio changed, the velocity of the solid/liquid interface was varied and this in turn changed the distribution coefficient in the sample.

Photoluminescence tests were performed on the same samples that were used in the variable temperature Hall study. Similarly, no variation was found between the microgravity samples and those grown on ground, but the results are still important since they add to the knowledge base of the GaSb material system. For the p-type samples, the liquid He temperature results are consistent with high quality bulk crystals. A bound exiton peak was found at ~793 meV. Also, a peak centered at 799.5 meV (12.5 meV below the bandgap edge) was found and was attributed to an unknown acceptor. The dominant peak in all undoped samples at 777 meV related to the neutral state of the native double acceptor.

The undoped samples were also tested at variable temperatures up to 150°K. The 12.5 meV peak was found to increase in relative intensity over this range while the BE peak decreased in intensity. The temperature variation of the native acceptor peak at 777 meV was found to approach the bandgap edge. This was explained by either a true variation in the acceptor band level or a variation in the photoabsorption capture cross section *other than* inversely with electron energy as in Eagle's model (the latter being more likely).

The n-type samples were only tested at liquid He temperatures. In the lower-doped samples, the spectral distributions were found to vary greatly with increasing input power as the larger concentration of holes created was able to neutralize the shallow levels as well as the deeper levels. The transition to the ionized state of the native double acceptor was also

revealed at 710 meV. A blue-shifting of the peaks was observed as the doping level increased due to conduction-band filling. Finally, for the highest doped sample, there is only a broad peak visible related to the neutral state of the acceptor level.

It is concluded that the growth of high-quality GaSb crystals is possible in space with low dislocation densities and with no striations due to convective flows. With a better ampoule design and a scaled up furnace, larger float-zoned GaSb crystals of commercial quality are possible. However, it does not appear that the growth of these crystals in a microgravity environment would hold any distinct advantage over terrestrial-grown crystals in terms of the defect behaviors and their associated properties.

APPENDIX
GaAs RESULTS AND DISCUSSION

Four ampoules containing GaAs crystals were processed in space using the float-zone technique. All of the ampoules sustained launch vibrations and landing loads. Figure 80 shows the resulting GaAs crystals grown in space. In general the texture of the grown crystals was rough with a dull surface observed in all of the samples. Processing speeds ranged from 1 to 56.2 mm/hr with lamp power input during translation ranging from 439 to 486 Watts. Sample diameters for all space grown crystals averaged 16 mm. Samples UFL4-GaAs, UFL5-GaAs, and UFL6-GaAs were processed with video downlink to help visually establish the float zone. Sample UFL-GaAs (Spare) was flown blind (without video) by using power levels based on a previously processed ampoule in the flight.

Diameter Control and Float Zone Length

All space-processed samples in the initial crystal growth exhibit a reduction in diameter contained within the first 8 mm of growth, followed by a gradual increase in cross section that attempts to but does not reach the feedstock diameter. As was the case with GaSb, this behavior can be explained by the criterion for the stability of the external shape of crystals in crystal growth from the melt as defined by Surek [76SUR]. Float zone length measurements were performed on the microgravity samples. Heights longer than those able

197

to obtained on ground (maximum 7-8mm [95HER]) were realized without causing an undesirable disruption of the molten zones. Zone heights ranged from 7 to 13 mm. Using the same reasoning as before with the GaSb samples, the molten zone lengths can be strongly correlated with lamp power input, translation speed, sample position and crystal diameter as follows:

- Zone lengths are obviously directly proportional to lamp power input.
- Zone lengths are inversely proportional to translation speed.
- Zone lengths decrease as the molten zones approach the ends of the samples.
- Zone lengths are inversely proportional to the diameter of the newly grown crystal.

Float zone limits of stability were not tested in microgravity because of the limitations imposed by the small length of the crystals compared to the predicted microgravity Rayleigh stability limit.

<u>Microstructural Characterization</u>

Samples UFL4-GaAs, UFL5-GaAs, and UFL6-GaAs were processed with a full melt zone. Figure 81 shows an axial slice of UFL5-GaAs. As observed, single crystalline growth was established in the first ~1 mm, followed by polycrystalline growth without voids, and finally by polycrystalline growth with voids for the majority of the crystal. This growth was unexpected and indicates the B_2O_3 encapsulant was not sufficient to prevent loss of arsenic during growth. This had the deleterious effects of first, disturbing the growth and creating polycrystalline material, and second, allowing the sample to grow non-stoichiometric leaving gallium at the grain boundaries of the material. Note that the gallium with its low melting

point left the crystal and created the voids visible in the photo. As mentioned above, sample UFL-GaAs (spare) was processed without video downlink. As a result, a zone was not established at the power levels used because of excess As buildup on the ampoule wall. However, one can assume that had a zone been established, the result would have been the same as above.
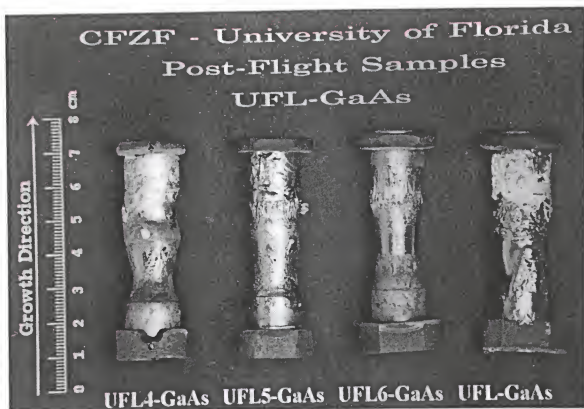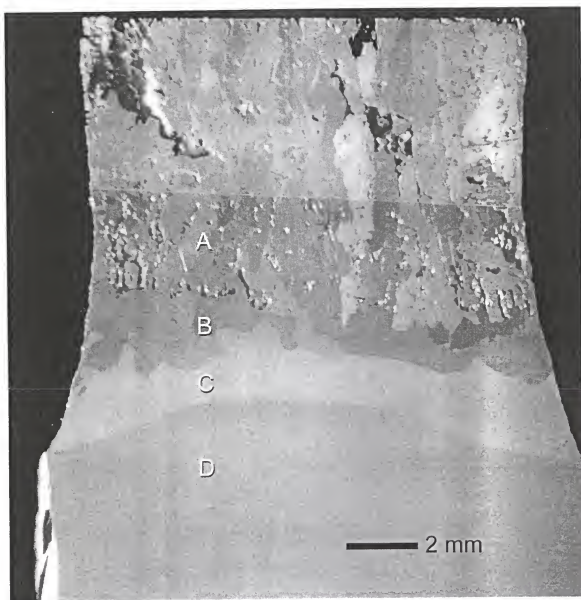
Figure 80 - Microgravity-processed GaAs crystals.

Figure 81 - Axial slice of UFL5-GaAs showing single crystal and polycrystalline growth. The structure of this sample includes: A) polycrystalline section with voids, B) polycrystalline section without voids, C) regrown single crystalline section, and D) as-received CZ-grown seed.

LIST OF REFERENCES

[1879HAL]   E. H. Hall, American Journal of Mathematics, **2** (1879) 287.

[1892RAY]   L. Rayleigh, Philosophical Magazine and Journal of Science, Fifth Series, **34** (1892) 145.

[52PHA]   W. G. Pfann, Transactions of the AIME, **194** (1952) 747.

[52HOR]   F. H. Horn, Philosophical Magazine **43** (1952) 1210.

[53BUR]   J. A. Burton, R. C. Prim and W. P. Slichter, Journal of Chemical Physics, **21** (1953) 1987.

[53TIL]   W. A. Tiller, K. A. Jackson, J. W. Rutter and B. Chalmers, Acta Metallurgica, **1** (1953) 428.

[54LEI]   H. N. Leifer and W. C. Dunlap, Jr., Physical Review, **95** (1954) 51.

[56BIL]   E. Billig, Proceedings of the Royal Society (London) **A235** (1956) 37.

[56HEY]   W. Heywang, Zeitschrift fur Naturfrosch, **11a** (1956) 238.

[57CAL]   A. Calverley, M. Davis and R. F. Lever, Journal of Scientific Instruments, **34** (1957) 142.

[58HRO]   H. Hrostowski and C. S. Fuller, Journal of Physics and Chemistry of Solids, **4** (1958) 155.

[58VAN]   L. J. van der Pauw, Philips Research Reports, **13** (1958) 1.

[60EAG]   D. M. Eagles, Journal of the Physics and Chemistry of Solids, **16** (1960) 76.

[60SAG]   A. Sagar, Physical Review, **117** (1960) 93.

[61STR]   A. J. Strauss, Physical Review, **121** (1961) 1087.

[63PIL]   H. Piller, Journal of the Physics and Chemistry of Solids, **9** (1963) 425.

[64EFF]   D. Effer and P. J. Etter, Journal of the Physics and Chemistry of Solids, **25** (1964) 451.

[65BAX]   R. D. Baxter, R. T. Bate, and F. J. Reid, Journal of Physics and Chemistry of Solids, **26**, (1964) 41.

[65GAS]   D. B. Gasson, Journal of Scientific Instruments, **42** (1965) 114

[65HAB]   M. A. Habegger and H. Y. Fan, Physical Review, **138** (1965) 598.

[65JOH]   E. J. Johnson and H. Y. Fan, Physical Review, **139** (1965) A1991.

[65VAN]   M. H. Van Maaren, Journal of Physics and Chemistry of Solids, **27** (1965) 472.

[65YEP]   T. O. Yep and W. M. Becker, Journal of Applied Physics, **37** (1965) 456.

[66COL]   K. Colbow, Physical Review, **141** (1966) 742.

[66HAR]   H. B. Harland and J. C. Woolley, Canadian Journal of Physics, **44** (1966) 2715.

[66REI]   F. J. Reid, R. D. Baxter, and S. E. Miller, Journal of the Electrochemical Society, **133** (1966) 713.

[67BAX]   R. D. Baxter, F. J. Reid and A. C. Beer, Physical Review, **162** (1967) 718.

[67VAN]   Y. J. Van Der Meulen, Journal of Physics and Chemistry of Solids, **28** (1967) 25.

[67VAR]   Y. P. Varshni, Physica, **34** (1967) 149.

[70AVE]   M. Averous, G. Bougnot, J. Calas and J. Chevrier, Physica Status Solidi, **37** (1970) 807.

[70LAZ]   I. K. Lazareva and V. M. Stuchebnikov, Soviet Physics: Semiconductors, **4** (1970) 550.

[70ROB]   J. Robert and D. Barjion, Physica Status Solidi A, **3** (1970) 421.

[71SZL]   K. Szlenk and W. Walukiewicz, Physica Status Solidi B, **48** (1971) K15.

[72BAS]   J. Basinski, C. C. Y. Kwan, J. C. Woolley, Canadian Journal of Physics, **50** (1972) 1068.

[72BEN]   C. Benoit a la Guillaume and P. Lavallard, Physical Review B, **5** (1972) 4900.

[72CAR]   J. R. Carruthers and M. Grasso, Journal of Applied Physics, **43** (1972) 436.

[72JAK]   W. Jakowetz, W. Rühle, K. Breuninger and M. Pilkuhn, Physica Status Solidi (a), **12** (1972) 169.

[72KIM]   K. M. Kim, A. F. Witt and H. C. Gatos, Journal of the Electrochemical Society, **119** (1972) 1218.

[72KYU]   A. S. Kyuregyan, I. K. Lazareva, V. M. Stuchebnikov, and A. E. Yunovich, Soviet Physics: Semiconductors, **6** (1972) 208.

[73BAC]   R. Z. Bachrach and O. G. Lorimor, Physical Review B, **7** (1973) 700.

[73DOL]   M. D'Olne Campos, A. Gouskov, L. Gouskov, and J. C. Pons, Journal of Applied Physics, **44** (1973) 2642.

[73RÜH]   W. Rühle, W. Jakowetz, and M. Pilkuhn, Bulletin of the Academy of Science USSR Physics Series, **37** (1973) 99.

[74SUN]   R. Y. Sun and W. M. Becker, Physical Review B, **10** (1974) 3436.

[75ASH]   D. J. Ashen, P. J. Dean, D. T. J. Hurle, J. B. Mullin, A. M. White, and P. D. Greene, Journal of the Physics and Chemistry of Solids, **36** (1975) 1041.

[75WIT]   A. F. Witt, H. C. Gatos, M. Lichtensteiger, M. C. Lavine and C. J. Herman, Journal of the Electrochemical Society, **122** (1975) 276.

[76HOO]   K. Hoo and W. M. Becker, Physical Review B **14** (1976) 5372.

[76RÜH]   W. Rühle, W. Jakowetz, C. Wölk, R. Linnebach, and M. Pilkuhn, Physica Status Solidi (b), **73** (1976) 255.

[76SUR]   T. Surek, Journal of Applied Physics, **47** (1976) 4384.

[76VAN]   J. A. Van Vechten and C. D. Thurmond, Physical Review B, **14** (1976) 3539.

[77COR]   S. R. Coriell and M. R. Cordes, Journal of Crystal Growth, **42** (1977) 466.

[77KRÖ]   F. A. Kröger, Annual Review of Materials Science, (1977) 449.

[77KUM]   M. Kumagawa, Y. Asaba and S. Yamada, Journal of Crystal Growth, **41** (1977) 245.

[78KUM]   M. Kumagawa, Journal of Crystal Growth, **44** (1978) 291.

[78NOA]   R. A . Noack, W. Rühle, and T. N. Morgan, Physical Review B, **18** (1978) 6944.

[78SEK]   Y. Seki, H. Watanabe and J. Matsui, Journal of Applied Physics **49** (1978) 822.

[78WEN]   H. Wenzl, A. Fattah, D. Gustin, M. Mihelcic, and W. Uelhoff, Journal of Crystal Growth, **43** (1978) 607.

[78WIT]   A. F. Witt, H. C. Gatos, M. Lichtensteiger and C. J. Herman, Journal of the Electrochemical Society, **125** (1978) 1832.

[79BEN]   K. W. Benz and G Müller, Journal of Crystal Growth, **46** (1979) 35.

[79LEB]   A. I. Lebedev and I. A. Strel'nikova, Soviet Physics of Semiconductors, **13** (1979) 229.

[79MAT]   P. C. Mathur and S. Jain, Physical Review B, **19** (1979) 3159.

[80CHI]   T. H. Chiu, J. L. Zyskind, and W. T. Tsang, Journal of Electronic Materials, **16** (1987) 57.

[80EDE]   G. Edelin and D. Mathiot, Philosophical Magazine B, **42** (1980) 95.

[80MIL]   D. C. Miller and G. A. Rozgonyi, Defect Characterization by Etching, Optical Microscopy and X-ray Topography, in Handbook on Semiconductors, Volume 3, Materials Properties and Preparation, S. P. Keller, Volume ed., T. S. Moss, Series ed., North Holland Publishing Company, Amsterdam (1980) 217.

[80MIY]   S. Miyazawa, S. Kondo, and M. Naganuma, Journal of Crystal Growth, **49** (1980) 670.

[80SAS]   A. Sasaki, M. Nishiuma, and Y Takeda, Japanese. Journal of Applied Physics, **19** (1980) 1695.

[80TAK]   K. Takahashi, Japanese Journal of Applied Physics, **19** (1980) 773.

[81HIL]   O. Hildebrand, W. Kuebart, K. W. Benz, and M. H. Plikuhn, IEEE Journal of Quantum Electronics, **QE-17** (1981) 284.

[81KEL]   W. Keller and A. Muhlbauer, Floating-Zone Silicon, Dekker, New York, (1981).

[81LAW]   H. D. Law, R. Chin, K. Nakano, and R. A. Milano, IEEE Journal of Quantum Electronics, **QE-17** (1981) 284.

[81NAK]   K. Nakashima, Japanese Journal of Applied Physics, **20** (1981) 1085.

[82BRO]   G. T. Brown, B. Cockayne, W. R. MacEwan, and V. W. Steward, Journal of Materials Science Letters, **1** (1982) 253.

[82GAT]   H. C. Gatos, in Materials Processing in the Reduced Gravity Environment of Space, G. Rindone, Ed., North-Holland, Amsterdam (1982) 355.

[83FOR]   R. Fornari, C. Paorici, L. Zanotti, and G. Zuccalli, Journal of Crystal Growth **63** (1983) 415.

[83JOR]   A. S. Jordan, R. Caruso, and A. R. Von Neida, Bell Systems Technology Journal, **62** (1983) 477.

[83KRA]   H. G. Kramer, Solid State Technology, January (1983) 137.

[83MÜL]   G. Müller and G. Neumann, Journal of Crystal Growth, **63** (1983) 58.

[84EYE]   A. Eyer, H Leiste and R. Nitsche, Proceedings of the 5th European Symposium on Materials Sciences Under Microgravity, Schloss Elmau (5-7 November 1984) 173.

[84KOU]   C. D. Kourkoutas, P. D. Bekris, G. J. Papaioannou and P. C. Euthmiou, Solid State Communications, **49** (1984) 1071.

[84LIN]   M. E. Lines, Journal of Applied Physics, **55** (1984) 4052, 4058.

[84WEI]   D. Weiler and H. Mehrer, Philosophical Magazine A, **49** (1984) 309.

[85AND]   I. A. Andreev, A. N. Baranov, M. Z. Zhingarav, V. I. Korol'kov, M. P. Mikhailova, and Yu. P. Yakovlev, Soviet Physics of Semiconductors, **19** (1985) 987.

[85BAR]   A. N. Baranov, T. I. Voronina, N. S. Zimogorova, L. M. Kansaya, and Yu. P. Yakovlev, Soviet Physics: Semiconductors, **19** (1985) 1030.

[85EYE]   A. Eyer and H. Leiste, Journal of Crystal Growth, **71** (1985) 249.

[86AME]   American Society for Testing and Materials, Annual Book of ASTM Standards, F 76-86.

[86CARa] T. Carlberg, Acta Astronautica, **13** (1986) 639.

[86CARb] T. Carlberg, Journal of Crystal Growth, **79** (1986) 71.

[86CHE]   M. J. Cherng, G. B. Stringfellow, D. W. Kisker, A. K. Srivastava, and J. L. Zyskind, Applied Physics Letters, **48** (1986) 419.

[86CRÖ]   A. Cröll, W. Müller and R. Nitsche, Journal of Crystal Growth, **79** (1986) 65.

[86LEE]   M. Lee D. J. Nicholas, K. E. Singer and B. Hamilton, Journal of Applied Physics, **59** (1986) 2895.

[86SUN]   W. A. Sunder, R. L. Barnes, T. Y. Kometani, J. M. Parsey, Jr. and R. A. Laudise, Journal of Crystal Growth, **78** (1986) 9.

[87CHI]   T. H. Chiu, J. L. Zyskind, and W. T. Tsang, Journal of Electronic Materials, **16** (1987) 57.

[87HUR]   D. T. J. Hurle, G. Müller, R. Nitsche, Crystal Growth From the Melt, in Fluid Sciences and Materials Science in Space, H. U. Walter, editor, (1987) 313.

[87NIC]   D. J. Nicholas, M. Lee, B. Hamilton and K. E. Singer, Journal of Crystal Growth, **81** (1987) 298.

[87PIE]   R. F. Pierret, Advanced Semiconductor Fundamentals, Addison-Wesley Pub. Co., Reading, MA, (1987).

[87SAN]   K. Sangwal, Etching of Crystals: Theory, Experiment, and Application, North-Holland, Amsterdam (1987).

[87SEK]   A. G. Elliot, C. Wei, and D. A. Vanderwater, Journal of Crystal Growth **85** (1987) 59.

[88JOH]   G. R. Johnson, B. C. Cavenett, T. M. Kerr, P. B. Kirby and C. E. C. Wood Semiconductor Science and Technology, **3** (1988) 1167.

[88MÜL]   G. Müller, Crystal Growth From the Melt, Springer-Verlag, Berlin, (1988).

[88NGA]   T. L. Ngai, R. C. Sharma and Y. A. Chang, Bulletin of Alloy Phase Diagrams, **9** (1988) 586.

[89CHE]   S. C. Chen and Y. K. Su, Journal of Applied Physics, **66** (1989) 350.

[89CRÖ]   A. Cröll, W. Muller-Sebert and R. Nitsche, Materials Research Bulletin, **24** (1989) 995.

[89GAR]   J. P. Garandet, T. Duffar and J. J. Favier, Journal of Crystal Growth, **96** (1989) 888.

[89WON]   D. Wong, H. K. Kim, Z. Q. Fang, T. E. Schlesinger, and A. G. Milnes, Journal of Applied Physics, **66** (1989) 2002.

[90ANA]   C. Anayama T. Tanahashi, K. Kuwatsuka, S. Nishiyama, S. Isozumi and K. Nakajima, Applied Physics Letters, **56** (1990) 239.

[90ICH]   M. Ichimra, K. Higuchi, Y. Hattori, and T. Wada, Journal of Applied Physics, **68** (1990) 6153.

[90MÜL]   G. Müller, Journal of Crystal Growth, **99** (1990) 1242.

[90ROS]   T. M. Rossi, D. A. Collins, D. H. Chow and T. C. McGill, Applied Physics Letters, **57**, (1990) 2256.

[90TIL]   E. Tillberg and E. Carlberg, Journal of Crystal Growth, **99** (1990) 1265.

[91CHE]   J. F. Chen and A. Y. Cho, Journal of Applied Physics, **70** (1991) 277.

[91CHI]   E. T. R. Chidley, S. K. Haywood, A. B. Henriques, N. J. Mason, R. J. Nicholas and P. J. Walker, Semiconductor Science and Technology, **6** (1991) 45.

[91SWA]   V. Swaminathan and A. T. Macrander, Materials Aspects of GaAs and InP Based Structures, Prentice Hall, Englewood Cliffs, New Jersey (1991).

[91WIL]   W. R. Wilcox, AIAA 29th Aerospace Sciences Meeting, Reno, NV (January 9-10, 1991) AIAA 91-0507.

[92BAS]   S. Basu, Applied Surface Science, **59** (1992) 159.

[92BRO]   E. R. Brown, S. J. Eglash, and K. A. Macintosh, Physical Review B, **46** (1992) 7244.

[92LAN]   C. Lan and S. Kou, Journal of Crystal Growth, **118** (1992) 151.

[92POLa]   A. Y. Polyakov, M. Stam, A. G. Milnes and T. E. Schlesingher, Materials Science and Engineering B, **12** (1992) 337.

[92POLb]   A. Y. Polykov, S. J. Pearton, R. G. Wilson, P. Rai-Choudhury, R. J. Hillard, X. J. Bao, M. Stam, A. G. Milnes, T. E. Schlesinger and J. Lopata, Applied Physics Letters, **60** (1992) 1318.

[92ŠES]   V. Šesták'ová and B. Štěpánek, Thermochimica Acta, **209** (1992) 277.

[92WUa]   M. C. Wu and C. C. Chen, Journal of Applied Physics, **72** (1992) 4275.

[92WUb]   M. C. Wu, C. W. Chen, and C. C. Chen, Journal of Applied Physics, **72** (1992) 1101.

[93MEI]   F. Meinardi, A. Parisini, and L. Tarricone, Semiconductor Science and Technology, **8** (1993) 1985.

[93MIL]   A. G. Milnes and A. Y. Polyakov, Solid State Electronics, **36** (1993) 803.

[94ABB]   R. Abbaschian, A. Gokhale, E. Jensen, and R. Panchapakesan, AIAA 32nd Aerospace Sciences Meeting and Exhibit, Reno, NV, (January 10-13, 1994) AIAA 94-0563.

[94DUTa]   P. S. Dutta, K. S. Sangunni, H. L. Bhat and V. Kumar, Journal of Crystal Growth, **141** (1994) 44.

[94DUTb]   P. S. Dutta, K. S. Sangunni, H. L. Bhat and V. Kumar, Journal of Crystal Growth, **141** (1994) 476.

[94JEN]   E. E. Jensen, M. S. Thesis, University of Florida, Gainesville (1994).

[94LE]   H. Q. Le, G. W. Turner, S. J. Eglash, H. K. Choi, and D. A. Coppeta, Applied Physis Letters, **64** (1994) 152.

[94LOW]   B. J. Lowry and P. H. Steen, International Journal of Multiphase Flow, **20** (1994) 439.

[94VAR]   A. Varaldi, C. Ghezzi, R. Magnanini, A. Parisini, L. Tarricone, A. Bosacchi, S. Franchi, V. Avanzini, and P. Alegri, Materials Science and Engineering B, **28** (1994) 174.

[95BOS]   A. Bosacchi, S. Franchi, P. Allegri, V. Avanzini, A. Baraldi, C. Ghezzi, R. Magnanini, A. Parisini, and L Tarricone, Journal of Crystal Growth, **150** (1995) 844.

[95CHI]   V. W. L. Chin, Solid-State Electronics, **38** (1995) 59.

[95DUT]   P. S. Dutta, K. S. R. Koteswara Rao, H. L. Bhat and V. Kumar, Applied Physics A, **61** (1995) 149.

[95GHE]   C. Ghezzi, R. Magnanini, A. Parisini, B. Rotelli, L Tarricone, A. Bosacchi and S. Franchi, Physical Review B, **52** (1995) 1463.

[95HER]   F. M. Herrmann and G. Müller, Journal of Crystal Growth **156** (1995) 350.

[95IYE]   S. Iyer, L. Small, S. M. Hegde, K. K. Bajaj, and A. Abul-Fadi, Journal of Applied Physics, **77** (1995) 5902.

[95JIA]   W. J. Jiang, Y. M. Sun and M. C. Wu, Journal of Applied Physics, **77** (1995) 1725.

[95MÜL]   G. Müller, in Scientific Results of the German Spacelab Mission D-2, P. R. Sham, M. H. Keller, B. Shiewe (Eds.), WPF (1995) 463.

[95SKR]   B. J. Skromme, in Handbook of Compound Semiconductors: Growth, Processing, Characterization, and Devices, P. H. Holloway and G. E. McGuire (Eds.), Noyes Publications, Park Ridge, NJ, 1995, 679-771.

[96ABB]   R. Abbaschian, C. López, A. Gokhale, E. Jensen, and R. Raman, in Solidification Science and Processing, I. Ohnaka and D. M. Stefanescu (Eds.), TMS, Warrendale, PA (1996) 319.

[96BIG]   A. Bignazzi, E. Grilli, M. Guzzi, M. Radice, A. Bosacchi, S. Franchi and R. Magnanini, Journal of Crystal Growth, **169** (1996) 450.

[96CRÖ]   A. Cröll, M. Schweizer, A. Tegetmeier, K. W. Benz, Journal of Crystal Growth, **166** (1996) 239.

[96DAN]   A. N. Danilewsky, S. Lauer, J. Meinhardt, K. W. Benz, B. Kaufmann, R. Hofmann and Dörnen, Journal of Electronic Materials, **25** (1996) 1082.

[96DUT]   P. S. Dutta, V. Prasad, H. L. Bhat, and Vikram Kumar, Journal of Applied
            Physics, **80** (1996) 2847.

[96ŠES]   V. Šestáková, B. Štepánek, J. Šesták, Crystal Research and Technology, **31**
            (1996) 929.

[96TEG]   A. Tegetmeier, A. Cröll, A. Danilewsky, and K. W. Benz, Journal of Crystal
            Growth **166** (1996) 651.

[96YU]   P. Y. Yu and D. M. Cardona, Fundamentals of Semiconductors: Physics and
            Materials Properties, Springer-Verlag, Berlin (1996).

[97CRÖ]   A. Cröll and K. W. Benz, AIAA 48th International Astronautical Congress,
            Turin, Italy, (October 6-10, 1997) AIAA 97-12106.

[97DUT]   P. S. Dutta, H. L. Bhat, and V. Kumar, Journal of Applied Physics, **81** (1997)
            5821.

[97LÓP]   C. R. López, M. S. Thesis, University of Florida, Gainesville, Florida, (1997).

[97MAT]   B. P. Matisak, A. X. Zhao, R. Narayanan, A. L. Fripp, Journal of Crystal
            Growth, **174** (1997) 90.

[97NIS]   T. Nishinaga, P. Ge, C. Huo, J. He, T. Nakamura, Journal of Crystal Growth,
            174 (1997) 96.

BIOGRAPHICAL SKETCH

Jeffrey Robert Mileham was born in Kenmore, New York, on August 14, 1969. He grew up in the neighboring city of Tonawanda, New York, as did his parents and grandparents. In 1987 he graduated from Tonawanda High School and accepted an appointment to the United States Naval Academy. However, deciding that the military life was not to his suiting, he decided to pursue a degree in mechanical engineering at the State University of New York (SUNY) at Buffalo in 1989. He received his bachelor's degree in 1991 and continued on for the Master of Science degree. In the Fall of 1993 he was accepted into the Ph.D. program at the University of Florida in the Department of Materials Science and Engineering. During his first semester there, he completed writing his thesis for SUNY at Buffalo and received his Master of Science degree in January 1994. He then obtained his Ph.D. in August of 1999.

I certify that I have read this study and that in my opinion it conforms to acceptable standards of scholarly presentation and is fully adequate, in scope and quality, as a dissertation for the degree of Doctor of Philosophy.
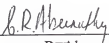
Stephen J. Pearton, Chair
Professor of Materials Science and
Engineering

I certify that I have read this study and that in my opinion it conforms to acceptable standards of scholarly presentation and is fully adequate, in scope and quality, as a dissertation for the degree of Doctor of Philosophy.
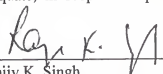
Reza Abbaschian, Cochair
Professor of Materials Science and
Engineering

I certify that I have read this study and that in my opinion it conforms to acceptable standards of scholarly presentation and is fully adequate, in scope and quality, as a dissertation for the degree of Doctor of Philosophy.

Cammy R. Abernathy
Professor of Materials Science and
Engineering

I certify that I have read this study and that in my opinion it conforms to acceptable standards of scholarly presentation and is fully adequate, in scope and quality, as a dissertation for the degree of Doctor of Philosophy.

Rajiv K. Singh
Professor of Materials Science and
Engineering

I certify that I have read this study and that in my opinion it conforms to acceptable standards of scholarly presentation and is fully adequate, in scope and quality, as a dissertation for the degree of Doctor of Philosophy.

Fred Sharifi
Associate Professor of Physics

This dissertation was submitted to the Graduate Faculty of the College of Education and to the Graduate School and was accepted as partial fulfillment of the requirements for the degree of Doctor of Philosophy.

August, 1999

Jack Ohanian
Dean, College of Engineering

Winfred M. Phillips
Dean, Graduate School